論文 / 著書情報
Article / Book Information

題目(和文)	
Title(English)	Bond Randomness Effect in Frustrated Quantum Antiferromagnets
著者(和文)	渡邊正理
Author(English)	Masari Watanabe
出典(和文)	学位:博士(理学), 学位授与機関:東京工業大学, 報告番号:甲第11693号, 授与年月日:2022年3月26日, 学位の種別:課程博士, 審査員:田中 秀数,平山 博之,笹本 智弘,髭本 亘,西田 祐介
Citation(English)	Degree:Doctor (Science), Conferring organization: Tokyo Institute of Technology, Report number:甲第11693号, Conferred date:2022/3/26, Degree Type:Course doctor, Examiner:,,,,
学位種別(和文)	博士論文
Type(English)	Doctoral Thesis

Bond Randomness Effect in Frustrated Quantum Antiferromagnets

Masari Watanabe

Department of Physics,
Tokyo Institute of Technology

February 28, 2022

Abstract

In frustrated magnets, the experimental realization of a quantum disordered ground state (QDGS), especially quantum spin liquid (QSL) ground state, is a central topic in condensed matter physics. Several promising candidates were reported, and a number of QSL-like behavior, such as excitation continuum, T-linear specific heat, and so on, were observed. However, whether the QSL-like behavior is owing to the synergy between spin frustration and quantum fluctuation or bond randomness effects has not been clarified yet. Several theoretical studies have demonstrated that the synergy effect between the magnetic frustration and the bond randomness suppresses magnetic ordering and induces a QSL-like state. This QSL-like state was proposed to be a random-singlet (RS) state, where not only nearest-neighbor spins but also distant spins form singlet pairs with random coupling energy. Since thermodynamic properties of RS and QSL are predicted to be similar to each other, it is important to elucidate the microscopic nature of randomness-induced QDGSs. However, its experimental verifications are still insufficient due to a lack of model materials.

In this work, I synthesized polycrystalline samples of $SrLaCuSbO_6$ (SLCSO) and $SrLaCuNbO_6$ (SLCNO) by a solid-state reaction. Magnetic Cu^{2+} ions with $S = 1/2$ Heisenberg spins form a square lattice with nearest-neighbor (J_1) and next-nearest-neighbor (J_2) exchange interaction. Thus, SLCSO and SLCNO were magnetically described as quasi-two-dimensional $S = 1/2$ J_1–J_2 square lattice Heisenberg antiferromagnet (SLHAF). The temperature dependence of the magnetic susceptibilities of both compounds shows a broad maximum characteristic of an $S = 1/2$ SLHAF. However, both compounds undergo magnetic phase transitions at $T_N = 13.6$ and 15.7 K for SLCSO and SLCNO, respectively, due to weak inter-layer interactions. Neutron powder diffraction measurements reveal contrasting spin structures in both compounds. The spin structures of SLCSO and SLCNO below T_N are Néel antiferromagnetic and collinear antiferromagnetic, respectively. This result demonstrates that the nearest-neighbor interaction is dominant in SLCSO, whereas the next-nearest-neighbor interaction is dominant in SLCNO. The magnitude of the ordered moment was evaluated at 3.5 K to be $m = 0.39(3)\,\mu_B$ for SLCSO and $0.37(1)\,\mu_B$ for SLCNO, which are significantly reduced from $1\mu_B$ expected in the classical spin case. The shrink of the ordered magnetic moment was caused by not only magnetic frustration effects but also bond randomness effects arising from the site disorder of Sr^{2+} and La^{3+} ions.

Next, I synthesized the mixed system $SrLaCuSb_{1-x}Nb_xO_6$ with $0.1 \leq x \leq$

0.5 and performed systematic magnetic susceptibility and specific heat measurements. Because the superexchange paths via Sb^{5+} and Nb^{5+} make J_1 and J_2 dominant, respectively, the random substitution of Nb^{5+} for Sb^{5+} produces strong randomness in the magnitude of J_1 and J_2. Hence, these systems can be magnetically described as $S = 1/2$ random $J_1 - J_2$ SLHAF. Compared with parent systems SLCSO and SLCNO, the bond randomness effect is more pronounced in $SrLaCuSb_{1-x}Nb_xO_6$ even for a small amount of Nb substitution. No sign of magnetic ordering was observed in specific heat measurements down to 0.35 K for $0.1 \leq x \leq 0.5$. Furthermore, μSR measurements on a sample with $x = 0.2$ revealed that neither magnetic ordering nor spin freezing occurs. The temperature dependence of the magnetic susceptibility and the specific heat at low temperatures follows the power law, suggesting the realization of a gapless QDGS. LF-μSR measurements at 0.035 K showed that muon spin relaxation is still retained even for an applied longitudinal field of 0.3 T, suggesting that spin fluctuation is maintained even at 0.035 K. This is consistent with the emergence of the QDGS.

The QSL-like QDGS is naively considered to be the RS state. However, there are some disagreements between experimental and theoretical results for the temperature dependences of magnetic and thermodynamic quantities. It was theoretically predicted that the low-temperature magnetic specific heat divided by temperature $C_{\mathrm{mag}}(T)/T$ and magnetic susceptibility $\chi(T)$ follow power laws $\chi \propto T^{-\gamma}$ and $C_{\mathrm{mag}}(T)/T \propto T^{-\gamma}$ with same exponent γ for the RS state. Although temperature dependence of magnetic susceptibility and specific heat of $SrLaCuSb_{1-x}Nb_xO_6$ for $0.1 \leq x \leq 0.5$ follow power laws in the low-temperature region, the exponents γ estimated from $C_{\mathrm{mag}}(T)/T$ and $\chi(T)$ do not agree with each other.

Contents

1 Introduction **6**

1.1 Magnetic frustration and low dimensionality 6

1.2 Quantum spin liquid 8

1.3 Previous studies on QSL candidate materials 10

1.3.1 $S = 1/2$ organic salt triangular lattice antiferromagnet . . 10

1.3.2 $S = 1/2$ kagome-lattice antiferromagnet herbertsmithite $ZnCu_3(OH)_6Cl_2$ 13

1.4 Randomness induced quantum disordered ground states 16

1.4.1 Theoretical study by exact diagonalization 16

1.4.2 Theoretical study by RG and QMC 17

1.5 Purpose of this study 20

2 Experimental Detail **22**

2.1 Sample preparation 22

2.2 Powder X-ray diffraction measurement 22

2.2.1 Rietveld analysis 23

2.3 Neutron powder diffraction measurement 24

2.3.1 Neutron time-of-flight spectroscopy 25

2.4 Magnetization measurement 26

2.5 Specific heat measurement 28

2.5.1 Theory of the relaxation method: Simple model 28

2.5.2 Theory of the relaxation method: Two-Tau model 31

2.6 Electron spin resonance measurement 33

2.7 Muon spin relaxation measurement 35

3 Effect of Weak Bond Randomness in Spin-1/2 J_1–J_2 Quasi-Square-Lattice Heisenberg Antiferromagnets: $SrLaCuSbO_6$ and $SrLaCuNbO_6$ **39**

3.1 Introduction 40

3.1.1 $S = 1/2$ Square-Lattice $J_1 - J_2$ Heisenberg model 40
3.1.2 B-site Ordered Double Perovskites $Sr_2Cu{M}O_6$ (M =Te^{6+}, W^{6+}) 42
3.2 Experimental results 46
3.2.1 Crystal structure 46
3.2.2 Electron spin resonance 53
3.2.3 Magnetic susceptibility and magnetization 55
3.2.4 Specific heat 58
3.2.5 μSR measurements 60
3.2.6 Magnetic structure 72
3.3 Discussion 78
3.3.1 Super-exchange interaction in $SrLaCuSbO_6$ and $SrLaCuNbO_6$ 78
3.3.2 Magnetic models of $SrLaCuSbO_6$ and $SrLaCuNbO_6$ . . . 79
3.4 Summary 81

4 Effect of Strong Bond Randomness in Spin-1/2 J_1−J_2 Square-Lattice Antiferromagnets: $SrLaCuSb_{1-x}Nb_xO_6$ 83
4.1 Introduction 84
4.1.1 Theoretical study of bond randomness effects in square lattice quantum antiferromagnets 84
4.1.2 Theoretical study on the effect of the exchange randomness on the frustrated quantum magnets 85
4.1.3 Spin-1/2 randomJ_1−J_2 square lattice antiferromagnet $Sr_2CuTe_{1-x}W_xO_6$ 87
4.2 Experimental results and discussion 95
4.2.1 X-ray diffraction and Rietveld analysis 95
4.2.2 Magnetic susceptibility 98
4.2.3 Magnetization process 102
4.2.4 Specific heat 103
4.2.5 Muon spin rotation and relaxation 112
4.3 Summary 121

5 Summary and outlook 123

Acknowledgments 127

References 129

Chapter 1

Introduction

The nature of magnetic insulators can be described as a collective of localized electron spins with quantum mechanical exchange interactions. Remarkable quantum effects appear particularly for the systems with small spin quantum numbers. Even in the simple model of two $S = 1/2$ Heisenberg spins with an antiferromagnetic interaction J, the ground state is not a Néel state with antiparallel spins, but a spin singlet state, which is a superposition of $|\uparrow\downarrow\rangle$ and $|\downarrow\uparrow\rangle$ as $\frac{|\uparrow\downarrow\rangle - |\downarrow\uparrow\rangle}{\sqrt{2}}$, where $|\uparrow\rangle$ and $|\downarrow\rangle$ are the spin-up and spin-down states, respectively. The collection of such quantum spins, i.e., quantum spin systems, provides fertile ground for exploring exotic quantum phenomena appearing in the macroscopic scale. The study of quantum spin systems is expanding the frontiers of condensed matter physics as a result of the good collaboration between theoretical studies using analytical and numerical methods and experimental studies using model materials.

1.1 Magnetic frustration and low dimensionality

Magnetic frustration is a key concept for novel magnetic phases to be manifested in quantum spin systems [1, 2]. Now we consider a situation in which three Ising spins are placed at the vertices of a triangle and interact antiferromagnetically with each other as shown in Fig 1.1. If there are only two spins, the antiparallel arrangement can minimize the energy. However, in a three interacting spin situation, if two spins are aligned antiparallel, the orientation of the other spin cannot be optimized simultaneously. In this case, any possible spin arrangement can not satisfy all antiferromagnetic interactions.

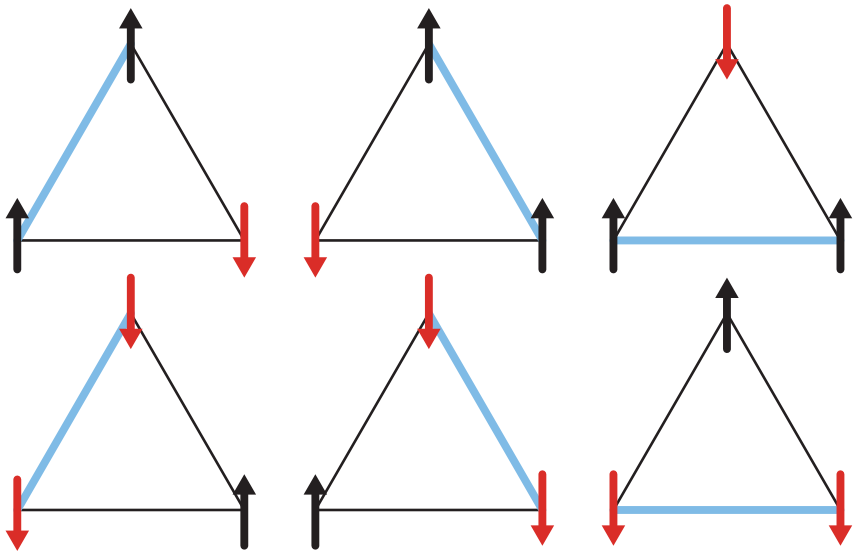

Figure 1.1: Schematic illustration of frustrated three Ising spins with antiferromagnetic interaction on a triangle. The arrows and blue bonds are directions of spins and unsatisfied bonds.

This situation is termed as magnetic frustration. In particular, the frustration caused by the geometry of the spin configuration is called "geometrical frustration". Moreover, magnetic frustration can also be produced by the competition of several types of interactions, as shown in Fig. 1.2. This is called "bond frustration". The J_1-J_2 square lattice Heisenberg antiferromagnet (SLHAF) with nearest-neighbor (NN) interaction J_1 and next-nearest-neighbor (NNN) interaction J_2 is a prototypical bond frustrated model. Spins are arranged on the corners of squares with antiferromagnetic interactions along the sides and diagonals, as shown in Fig 1.2. In the case of Ising spins, the Néel state with antiparallel spin configuration is the ground state if $J_2 = 0$, whereas for $J_2 = \frac{1}{2}J_1$, the ground state degenerates due to the competition between J_1 and J_2. Magnetic frustration potentially occurs even in a bipartite lattice.

The absence of long-range order at finite temperature in one- or two-dimensional spin systems with continuous symmetry is known as the Mermin–Wagner theorem [3, 4]. In the Heisenberg model in 2D or less, spin fluctuations with small wave numbers destroy the long-range magnetic. The energy gain of the magnetic ordering is prevented by the increase in entropy due to thermal fluctuations at long wavelengths. Particularly in one-dimensional quantum spin systems, strong non-perturbative theoretical approaches have been employed to investigate not only the ground state but also the excited state properties [5]. Several model materials have been synthesized [6, 7], and a

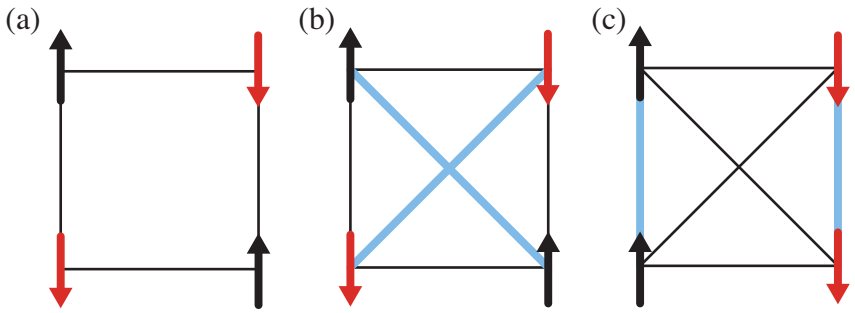

Figure 1.2: Schematic illustration of four Ising spins with antiferromagnetic coupling on a square. (a) In the case of the nearest-neighbor interaction only, all bonds are satisfied, although (b), (c) in the presence of the second-neighbor interaction, there are unsatisfied bonds (blue line).

consensus has been achieved that the ground state of $S = 1/2$ Heisenberg antiferromagnetic spin chain is a quantum spin liquid (QSL) state without any spontaneous symmetry breaking [8, 9].

1.2 Quantum spin liquid

Quantum spin liquid (QSL) is an exotic phase of matter in which spontaneous symmetry breaking does not occur even at absolute zero, but spins are entangled over long distances [2, 10, 11]. In conventional magnets, entropy is released to form a magnetically ordered state accompanied by spontaneous symmetry breaking. In some frustrated quantum magnets, entropy can be released to form a macroscopically non-degenerate state without a magnetic ordering owing to the strong quantum fluctuation. This fascinating quantum state is called a quantum spin liquid state.

QSL has been actively investigated since the resonating valence bond (RVB) state was proposed by Anderson in 1973 as a possible ground state for $S = 1/2$ triangular lattice Heisenberg antiferromagnet (TLHAF) with nearest-neighbor (NN) interaction [12]. The RVB is known as a superposition of singlet coverings, as shown in Fig. 1.3, and has received extensive attention due to its relevance to high-temperature superconductors. Although later studies have reached a consensus that the RVB state is not the ground state of $S = 1/2$ TLHAF with NN interactions, research on QSL is now at the forefront of condensed matter physics. Currently, various classes of quantum spin liquids other than RVB have been theoretically proposed, such as a chiral spin liquid [13],

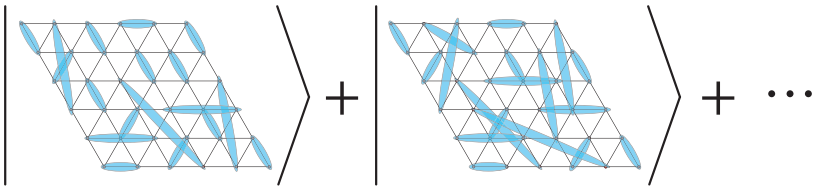

Figure 1.3: schematic illustration of the resonating valence bond state. The ellipse represents a singlet. Not only the nearest-neighbor spin pairs but also various spin pairs form a singlet. Naively, the RVB state is interpreted as a superposition of such singlet coverings.

$U(1)$ spin liquid [14], Z_2 spin liquid [15], and Kitaev spin liquid [16]. However, the experimental realization of these QSLs is still a challenging journey.

Experimentally, several promising candidate materials were reported, such as a $S = 1/2$ triangular and kagome lattice Heisenberg antiferromagnets. Well-studied examples of these candidates are the kagome-lattice antiferromagnet herbersmithite $ZnCu_3(OH)_6Cl_2$ [17–23], the triangular lattice antiferromagnet $YbMgGaO_4$ [24–26], and organic salt triangular lattice antiferromagnets [27–36]. In these materials, magnetic ordering does not occur down to low enough temperatures in comparison to their exchange interaction J, and a number of QSL-like behaviors, such as continuous magnetic excitations and T-linear or power-law temperature dependence of the specific heat, and so on, were observed in these compounds. However, the origin of the QSL-like behavior has not been clarified yet. There is also no consensus on the existence of an excitation gap, and conflicting experimental results have been obtained.

1.3 Previous studies on QSL candidate materials

1.3.1 $S = 1/2$ organic salt triangular lattice antiferromagnet

A variety of features suggestive of QSL ground states have been found in some organic triangular lattice antiferromagnets, such as κ-(BEDT-TTF)$_2$Cu$_2$(CN)$_2$ and EtMe$_3$Sb[Pd(dmit)$_2$]$_2$ [27–36]. In a typical organic triangular lattice antiferromagnet, the molecular dimers are responsible for $S = 1/2$, forming a triangular lattice, as shown in Fig. 1.4, reprinted from Ref. [30]. These two materials do not exhibit long-range magnetic ordering down to about 20 mK, although they both have a large antiferromagnetic exchange interaction J/k_B of about 250 K [28, 31]. Nevertheless, the details of the ground state are still under debate because of the conflicting experimental results showing a gapless ground state and a gapped ground state. Figure 1.5 shows the temperature dependence of specific heat C_p divided by temperature T for κ-(BEDT-TTF)$_2$Cu$_2$(CN)$_2$

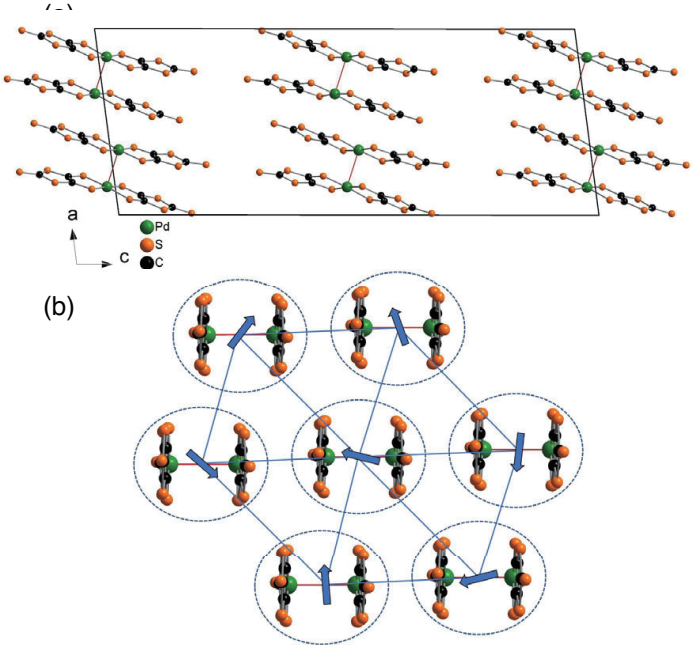

Figure 1.4: Crystal structure of EtMe$_3$Sb[Pd(dmit)$_2$]$_2$, reprinted from Ref. [30]. (a) shows Pd(dmit)$_2$ layers. (b) shows triangular lattice structure of the $S = 1/2$ in the Pd(dmit)$_2$ layer as an example of a typical dimer structure in the organic salt triangular lattice antiferromagnet. Spin density is localized on each molecule dimer of Pd(dmit)$_2$.

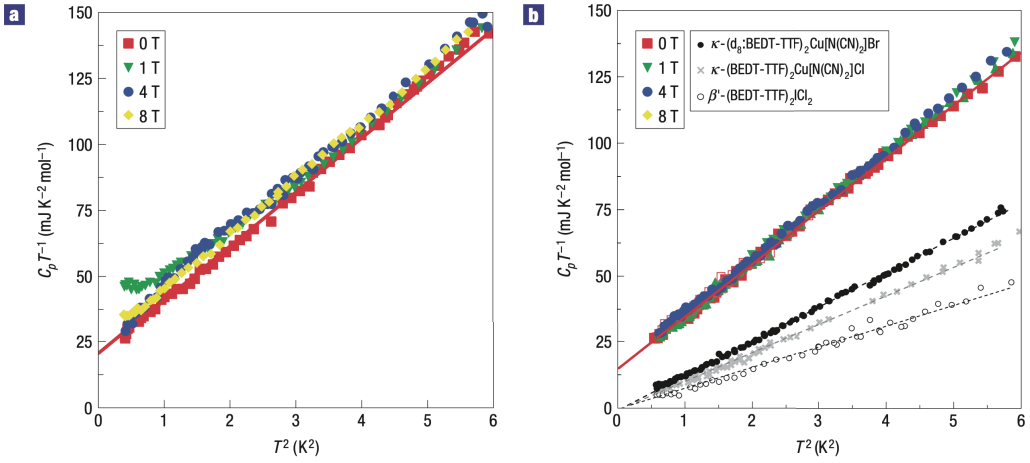

Figure 1.5: Low-temperature specific heat divided by temperature C_p/T for κ-(BEDT-TTF)$_2$Cu$_2$(CN)$_2$ measured in magnetic fields up to 8 T, reprinted from Ref. [33]. (b) contains other organic antiferromagnetic insulator, which occur long-range magnetic ordering, for comparison.

reported by Yamashita *et al.* [33]. T-linear contribution even in the insulating state of κ-(BEDT-TTF)$_2$Cu$_2$(CN)$_2$ was clearly observed, indicative of a gapless QSL without a long-range magnetic ordering. The T-linear contribution could originate from a fermionic spinon excitation that carries spin-1/2. On the other hand, thermal-conductivity measurements on κ-(BEDT-TTF)$_2$Cu$_2$(CN)$_2$ performed by Yamashita *et al.* [34], on the other hand, proposed a gapped QSL ground state. Figure 1.6 shows the temperature dependence of thermal conductivity κ divided by temperature T, reprinted from Ref. [34]. It was found that κ/T vanishes as extrapolating to $T = 0\,\mathrm{K}$, indicative of a gapped ground state. Similarly in the case of EtMe$_3$Sb[Pd(dmit)$_2$]$_2$, a gapless QSL ground state was proposed in Refs. [27, 30], while a gapped QSL ground state was suggested in Ref. [35]. A recent study [36] has shown that the temperature dependence of the thermal conductivity strongly depends on the cooling process. In the case of slow cooling, thermal conductivity represents T-linear contribution indicative of a gapless QSL ground state. On the other hand, in the case of rapid cooling, $\kappa(0\,\mathrm{K})$ vanishes and the phonon thermal conductivity is also suppressed.

Spin-1/2 triangular lattice Heisenberg antiferromagnet has a magnetically ordered ground state with 120° spin structure if the interaction is nearest neighbor only [37]. Thus, the mechanism of emergent QSL ground states in triangular lattice antiferromagnets involves additional ingredients beyond the nearest-neighbor interaction. Several studies have pointed out that the in-

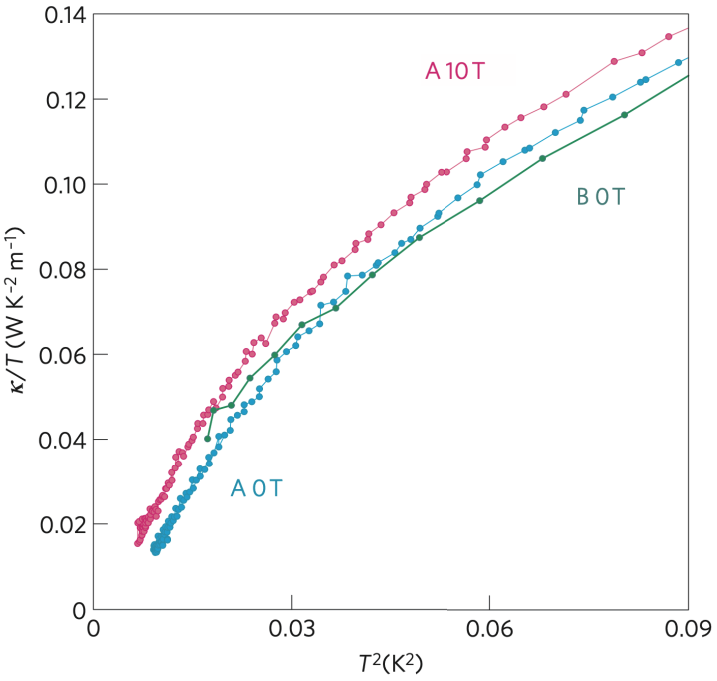

Figure 1.6: Thermal conductivity divided by temperature κ/T vs T^2, reprinted from Ref. [34]. The measurements were performed in magnetic fields up to 10 T below 300mK.

homogeneous charge distribution should be important in describing the magnetism of organic triangular lattice magnets. AC dielectric constant measurement [29] on κ-(BEDT-TTF)$_2$Cu$_2$(CN)$_2$ found a glassy response indicative of the random freezing of the electric polarization, which is strongly coupled with the magnetic system [38]. In the case of EtMe$_3$Sb[Pd(dmit)$_2$]$_2$, vibrational spectroscopy measurements [32] found multiple modes of charge and lattice fluctuations, which indicates that some inhomogeneous electronic states might be formed. As mentioned in Ref. [36], the cooling process of the sample is presumably related to the heterogeneity of the electronic state. Hence, this "inhomogeneity" might be the key to a comprehensive explanation of the conflicting experimental results obtained so far.

1.3.2 $S = 1/2$ kagome-lattice antiferromagnet herbertsmithite $ZnCu_3(OH)_6Cl_2$

The ground state of $S = 1/2$ kagome lattice Heisenberg antiferromagnet (KLHAF) is proposed to be a host of a QSL state. However, it is not clear what class of QSLs is realized in $S = 1/2$ KLHAF. In particular, no theoretical consensus has been reached even on the existence of an excitation gap from the ground state [14, 17, 23, 39–44]. Some density-matrix renormalization group (DMRG) calculations [17, 23] suggested a gapped Z_2 QSL ground state, while variational Monte Carlo [14, 40, 41] and tensor network [42] studies suggested a gapless $U(1)$ Dirac QSL ground state. Recent DMRG calculation [39] also proposed a $U(1)$ Dirac QSL ground state. Numerical calculations for the frustrated systems are very challenging. Thus experimental studies using model materials are indispensable.

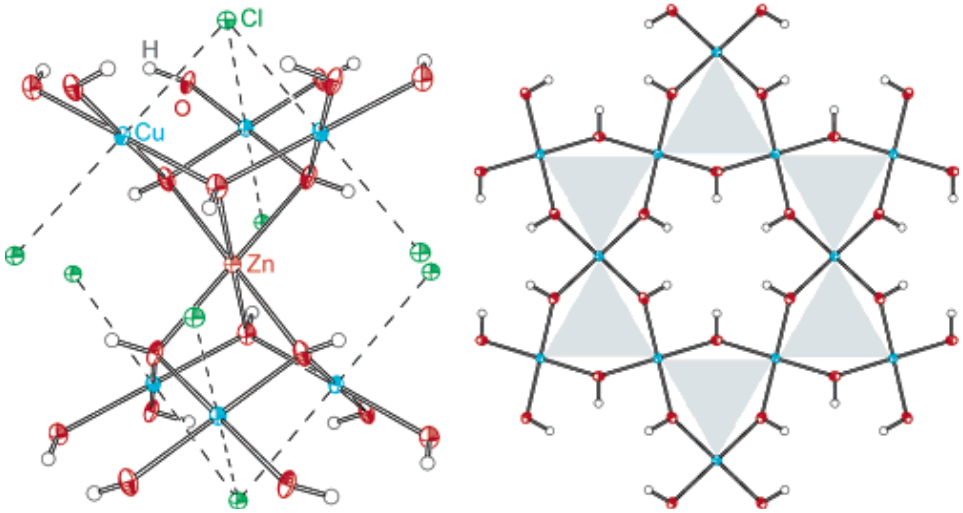

Figure 1.7: Crystal structure of herbertsmithite $ZnCu_3(OH)_6Cl_2$ reported by Shores *et al.* [22]. The left panel shows local environment of $Cu_3(OH)_6$. The Right panels shows a kagome plane viewed along crystallographic c-axis. Cu^{2+} ions formed regular kagome lattice in ab-plane, which stack in a manner of ABC along to c-axis.

Herbertsmithite $ZnCu_3(OH)_6Cl_2$ is one of the most studied KLHAFs as a promising candidate for the QSL [43]. As shown in Fig.1.7, Cu^{2+} ions forms a regular kagome lattice. The kagome layers are separated by Zn^{2+} ions, leading to a good two dimensionality [22].

No magnetic order was observed down to 50 mK ($\sim J/4000$) in the μSR measurement [21], which is highly sensitive to the internal magnetic field, even though the magnitude of the dominant exchange interaction is $J \simeq 17$ meV [20].

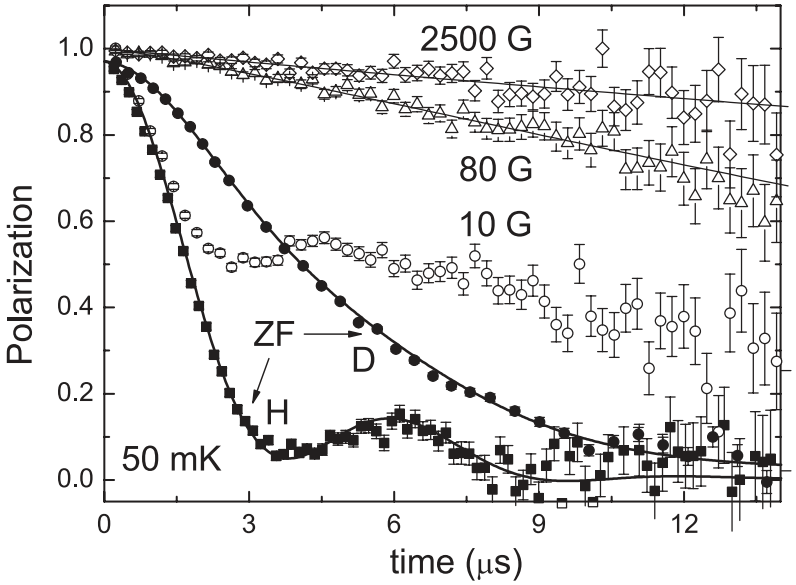

Figure 1.8: μSR time spectra of $ZnCu_3(OH)_6Cl_2$ in at 50 mK measured by Mendels *et al.*. The closed and open symbols represent zero field and longitudinal field data, respectively. No relaxations indicative of a static internal magnetic field were observed.

Specific heat $C(T)$ at low temperatures above 100 mK shows an almost linear temperature dependence, suggesting that the ground state is a gapless QSL [20]. On the other hand, there are some experimental indications that the ground state is a gapped QSL. For example, the ^{17}O NMR study [19] estimated the excitation gap Δ/J to be between 0.03 and 0.07, which is consistent with the DMRG estimate of $\Delta/J = 0.07$ to 0.12 [23].

No magnetic ordering is observed in herbertsmithite $ZnCu_3(OH)_6Cl_2$, but

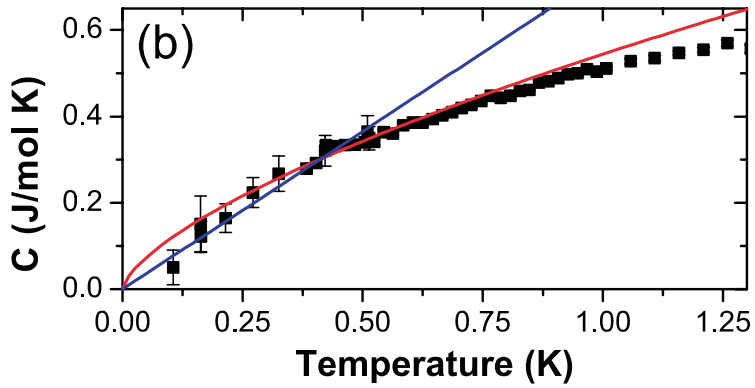

Figure 1.9: $C(T)$ of $ZnCu_3(OH)_6Cl_2$ in a zero magnetic field measured by Helton *et al.*. The blue and red curves are the results of fitting the data using $C(T) = \gamma T^{\alpha}$ with $\alpha = 1$ and 2/3, respectively.

there is no comprehensive explanation on the details of the ground state. In reality, this herbertsmithite has a problem with its crystal structure. Anomalous X-ray scattering using Zn and Cu edges revealed that 15% of the Zn^{2+} ions between the kagome layers are replaced by Cu^{2+} ions [18]. The presence of the Jahn–Teller ion Cu^{2+} ions in the interlayer of the kagome lattice causes local structural disorder, and the effect of the structural disorder should be transmitted into the kagome layer. As will be reviewed in Section 1.4, it has been pointed out that the effect of the intrinsic disorder should have an important influence on the magnetism of frustrated quantum spin systems.

1.4 Randomness induced quantum disordered ground states

1.4.1 Theoretical study by exact diagonalization

While various quantum spin liquid-like magnetism has been reported experimentally [45], there is no consensus on the mechanism of their manifestation. Recently, numerical studies by exact diagonalization indicated that the exchange interaction has a significant effect on the ground state of frustrated magnets [38, 46–52]. Watanabe *et al.* [38] reported a theoretical picture of the ground state of the $S = 1/2$ triangular lattice antiferromagnet κ-ET and dmit salts, in which QSL-like behavior have been observed. Basically, the ground state of the $S = 1/2$ TLHAF with only NN interaction is a magnetically ordered state with a 120° structure [37]. Meanwhile, it has been proposed that a quantum spin liquid can be realized by incorporating additional ingredients, such as next-nearest-neighbor interaction [53] and four-body interaction [54, 55], into the model.

Watanabe *et al.* [38] focused on the inhomogeneity of charge distribution inherent in κ-ET salts, and modeled their magnetism by $S = 1/2$ TLHAF with uniformly distributed NN interactions. The Hamiltonian was defined as

$$\mathcal{H} = \sum_{<I,j>} J_{ij} \boldsymbol{S}_i \cdot \boldsymbol{S}_j, \tag{1.1}$$

$$0 \leq J(1-\Delta) \leq J_{ij} \leq J(1+\Delta), \tag{1.2}$$

where the summation is taken over the nearest-neighbor spin pairs and $J_{ij} > 0$ is the random nearest-neighbor AF coupling obeying the bond-independent uniform distribution between $[(1-\Delta)J, (1+\Delta)J]$ with the mean J. $\Delta = 0$ corresponds to the uniform case and $\Delta = 1$ to the maximally random case. Ground state and finite temperature properties were obtained by exact diagonalization. For $\Delta \geq \Delta_c \simeq 0.6$, magnetic ordering including spin freezing is suppressed, and a QDGS is induced. This randomness-induced QDGS is composed of randomly frozen singlets, which are formed between not only nearest-neighbor spins but also distant spins, as shown in Fig. 1.10. This QDGS is termed the random singlet [56–58] or valence-bond-glass (VBG) state [59, 60].

Figures 1.11 (a) and (b) show a temperature dependence of specific heat C and magnetic susceptibility χ obtained by the numerical calculation. The

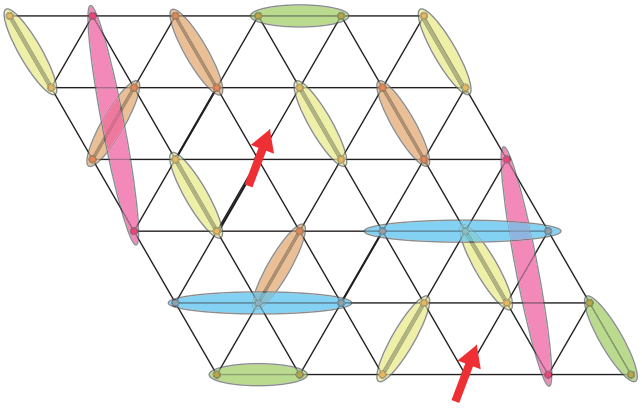

Figure 1.10: Schematic illustration of the valence-bond-glass (VBG) state on a triangular lattice. The ellipse represents a singlet. Not only the nearest-neighbor spin pairs but also various spin pairs form a singlet. The singlet pairs are frozen and do not "resonate". It has been pointed out that the RS state contains almost free orphan spins (red arrows) [46, 61].

randomness-induced QDGS is characterized by a finite magnetic susceptibility and a low-temperature specific heat proportional to the temperature, which arises from the many singlet spin pairs that can be easily excited to triplets with a small or zero energy, as shown in Fig. 1.11 (a) and (b). Furthermore, the magnetization curve shows linear field dependence without 1/3 magnetization plateau in the case with $\Delta \geq \Delta_c$, as shown in Fig. 1.11 (c). These results of this numerical calculation are consistent with gapless features observed in κ-ET and dmit salts [27, 31, 33, 35, 38]. Using a similar approach, it has been theoretically proposed that the RS state emerges under strong bond randomness in several frustrated models, such as kagome-lattice model [50, 51], square lattice J_1-J_2 model [48], honeycomb-lattice J_1-J_2 model [47], and the pyrochlore lattice model [49]. The RS state could be realized in $S=1/2$ kagome-lattice antiferromagnet herbersmithite $ZnCu_3(OH)_6Cl_2$.

1.4.2 Theoretical study by RG and QMC

RS state was originally discussed in a real-space renormalization group analysis of one-dimensional spin-1/2 Heisenberg antiferromagnetic chain (HAFC) with randomly distributed interaction strengths [56–58]. Strong-disorder renormalization group calculations revealed that the staggered averaged spin-spin correlation $C(r)$ in 1D RS state decays asymptotically with distance r as $C(r) \sim r^{-2}$, while as $C(r) \sim \frac{\ln^{1/2}(r)}{r}$ in the absence of bond randomness [58]. The spin correlation C_{ij} of a typical spin pairs between the i-th spin and j-th spin which

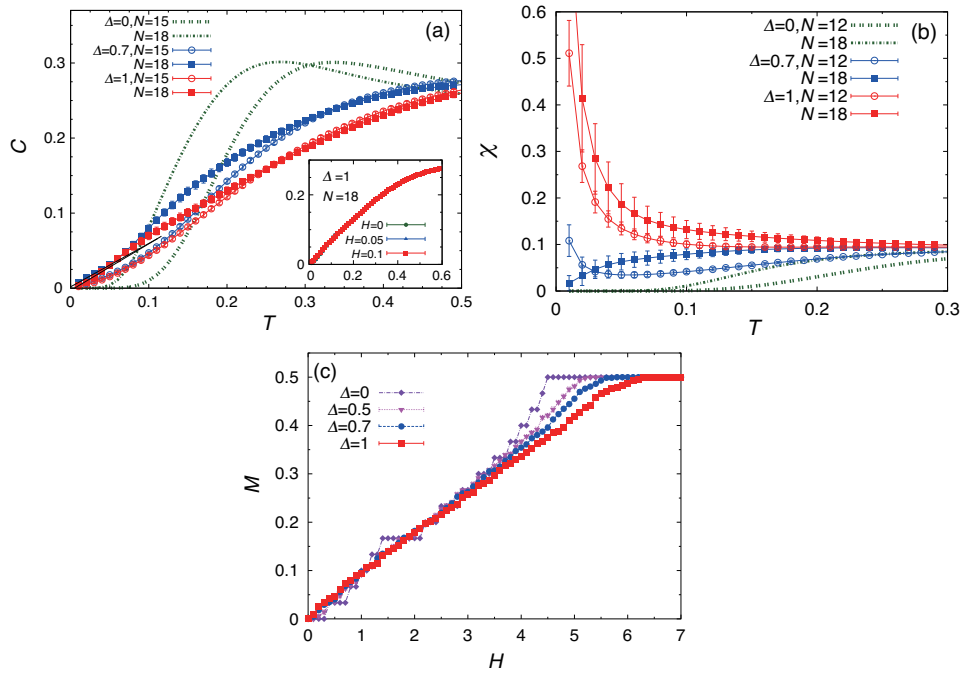

Figure 1.11: The temperature variation of (a) the specific heat per spin C and (b) the uniform susceptibility χ for various values of the Δ and system size. The inset in (a) represents the corresponding data in magnetic fields. (c) The magnetization curves for various values of the Δ. Reprinted from Ref. [38].

do not form a singlet is described as $C_{ij}^{\rm typical} \sim \exp(-c\sqrt{|i-j|})$, while that of distant spin pairs which forms a singlet is $C_{ij}^{\rm rare} \sim \mathcal{O}(1)$. The probability of this rare event forming a singlet is described as $P(|i-j|) \sim 1/|i-j|^2$. By averaging over all the spin sites, a power-law decay $C(r) \sim r^{-2}$ is obtained. This phenomenon is a good realization of the Griffith effect in a 1D system [62]. A few strongly correlated spins eventually dominate the average spin correlations, which can be measured by neutron scattering measurements etc. Such a power-law decay of the mean spin-spin correlation is also expected for the 2D RS state, whereas theoretical studies using exact diagonalization cannot address a spin-spin correlation function because the system size is not large enough.

Liu *et al.* [63, 64] investigated the effects of disorder in $S = 1/2$ square lattice Heisenberg antiferromagnet with nearest-neighbor exchange interactions J and six-spin interactions Q (see Fig. 1.12 (a)) by using a large-scale quantum Monte Carlo simulation. Hamiltonian of the $J-Q$ model is defined by

$$\mathcal{H} = -J\sum_{\langle ij\rangle} P_{ij} - Q\sum_{\langle ijklmn\rangle} P_{ij}P_{kl}P_{mn}, \tag{1.3}$$

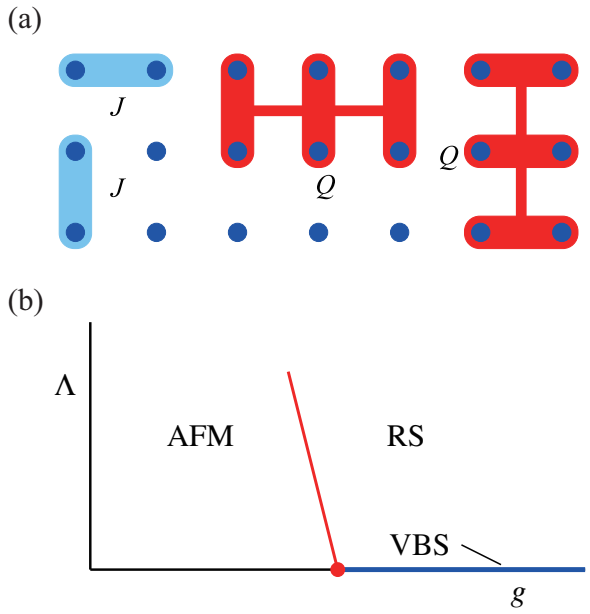

Figure 1.12: (a) Schematic illustration of the interaction in the $J-Q$ model on a square lattice, reprinted from Ref. [63]. Blue dots represents a spin-1/2. Light blue and red thick lines represent the J and Q terms. (b) Sketch of ground state phase diagram for the $J-Q$ model with exchange randomness, reprinted from Ref. [64]. g is a tuning parameter defined as $g = J/Q$ and Λ represents a disorder strength.

where $P_{ij} = 1/4 - \boldsymbol{S}_i \cdot \boldsymbol{S}_j$ is the singlet projector for two $S = 1/2$ spins, $\langle ij \rangle$ indicates nearest-neighbor sites, and the index pairs ij, kl, and mn in $\langle ijklmn \rangle$ are neighbors forming a horizontal or vertical column. This model can address very large system sizes because there is no negative sign problem. In this calculation, they use a bimodal distribution of couplings $J_{ij} \in \{0, \Lambda\}$ or $Q_{ijklmn} \in \{0, \Lambda\}$, with equal probability for the two values, in most cases. Figure 1.12 (b) shows a schematic ground state phase diagram of this model.

In the case with no bond randomness $\Lambda = 0$, there is a quantum phase transition from the antiferromagnetically ordered state to the valence bond solid state driven by varying $g = Q/J$. On the other hand, in the presence of randomness in J or Q, novel QDGS was observed. This QDGS was proposed to be a two-dimensional RS state. In the parameter range where this QDGS is obtained, a power-law decay of the *mean* spin-spin correlation $C(r) \sim r^{-2}$ was observed by the QMC calculations [63, 64]. This is a characteristic of the RS state.

The analysis of the finite temperature dependence of the magnetic susceptibility obtained by QMC calculations of the $J-Q$ model indicates that the dynamic critical exponent is $z > 2$ in the 2D RS state [63]. With a decrease in

z, the 2D RS state shifts to the AFM state at $z = 2$. The r^{-2} decay in the 2D RS state imposes a constraint on the critical exponent η, which is commonly defined for the quantum critical correlation function in d dimensional as

$$C(r) \propto r^{-(d+z-2+\eta)}. \tag{1.4}$$

From this equation, the relationship $\eta = 2 - z$ was obtained. Negative values of η should be obtained for the 2D RS state.

It is worth noting that this power-law decay $C(r) \sim r^{-2}$ of the mean spin-spin correlation is also verified by the DMRG calculation of the $S = 1/2$ square lattice Heisenberg model with random J_1 and J_2, which does not neglect the magnetic frustration [61]. RS phrase should appear in the 2D random system as well as the 1D random system.

1.5 Purpose of this study

The purpose of this study is to elucidate the effect of bond randomness on magnetic properties of frustrated quantum antiferromagnets, especially ground state nature. Recently, it was theoretically demonstrated that the randomness in the magnitude of exchange interaction suppresses the magnetic ordering and induces a quantum disordered ground state (QDGS). This randomness-induced QDGS should be a random singlet (RS) state, in which not only nearest-neighbor but also long-range spin pairs form a singlet, and the singlet covering is frozen. Some theoretical studies have proposed that the RS state exhibits thermodynamic properties similar to those of the quantum spin liquid (QSL) state. Therefore, the QSL candidates reported so far may contain RS states that mimic QSLs. To distinguish the RS state from the QSL state, it is essential to clarify the microscopic properties of the RS state and the magnetic excitations. However, experimental studies have scarcely been progressed due to a lack of suitable model materials in which the magnitude of bond randomness can be systematically tuned.

I explored new frustrated quantum antiferromagnets as a platform to investigate the bond randomness effect. I synthesized model materials for the prototypical frustrated systems of $S = 1/2$ $J_1 - J_2$ SLHAF, focusing on B-site ordered double perovskites. It was found that B-site ordered double perovskites $SrLaCuSbO_6$ and $SrLaCuSbO_6$ were good model materials for $S = 1/2$ $J_1 - J_2$ SLHAF. In addition, Sr^{2+} and La^{3+} ions with different charges are disordered in these compounds, resulting in local structure modulation and

inducing bond randomness as a similar mechanism in the quantum spin liquid candidate $YbMgGaO_4$, where Mg^{2+} and Ga^{3+} ions are disordered. Magnetization, specific heat, ESR, μSR, and neutron powder diffraction measurements were performed at low temperatures to characterize magnetic properties of $SrLaCuSbO_6$ and $SrLaCuSbO_6$, and elucidate the effect of the bond randomness produced by the disorder of the nonmagnetic ions, which are responsible for the "backbone" of the material.

To investigate the effects of stronger bond randomness, polycrystalline samples of $SrLaCuSb_{1-x}Nb_xO_6$ (SLCSNO) were systematically synthesized, in which Nb^{5+} ions were partially substituted for Sb^{5+}. Since the different electronic states of Sb^{5+} and Nb^{5+} ions are crucial for the magnitudes of J_1 and J_2 interactions, the disorder of Sb^{5+} and Nb^{5+} disturbs exchange interactions between spins more directly. Hence, SLCSNO is expected to be $S = 1/2$ square lattice random $J_1 - J_2$ Heisenberg antiferromagnets. Magnetization, specific heat, and μSR measurements were performed at low temperatures. It was found that in SLCSNO, the bond randomness effect strongly suppresses the magnetic order and induces a gapless quantum disordered ground state, in which the spins are strongly entangled both temporally and spatially.

Chapter 2

Experimental Detail

2.1 Sample preparation

Polycrystalline samples of $SrLaCuSb_{1-x}Nb_xO_6$ were synthesized via conventional solid state method for various concentration ratio of $x = 0,\ 0.1,\ 0.2,\ 0.3,\ 0.4,\ 0.5$, and 1. The chemical reaction is as follows:

$$2SrCO_3 + La_2O_3 + 2CuO + (1-x)Sb_2O_5 + xNb_2O_5 \longrightarrow 2SrLaCuSb_{1-x}Nb_xO_6 + 2CO_2$$

Stoichiometric mixture of $SrCO_3$ (99.9 %), La_2O_3 (99.9 %), CuO (99.99 %), Sb_2O_5 (99.99 %), and Nb_2O_5 (99.99 %) was ground well with an agate mortar and fired at 1000°C for 24 hours (Sequence I) in air according to temperature sequence shown in Fig. 2.1. Obtained powder sample was then reground, pelletized, and calcined twice at 1200°C for 24 hours (Sequence II) in air.

2.2 Powder X-ray diffraction measurement

Powder X-ray diffraction measurement was performed to determine the crystal structure of $SrLaCuSb_{1-x}Nb_xO_6$. In this measurement, I confirmed that Nb^{5+} ions substitute for Sb^{5+} ions in $SrLaCuSb_{1-x}Nb_xO_6$ and that the phase separation of the two parent compounds does not occur.

The diffraction data were collected using MiniFlex II. The optical system for the MiniFlex II is shown in Fig. 2.2. The X-ray source is characteristic X-ray emission of the CuKα_1 and CuKα_2, so that double peaks correspond to CuKα_1 and CuKα_2 are observed. The intensity of Kα_1 is twice that of Kα_2. The range of diffraction angle 2θ is $5° \leq 2\theta \leq 150°$.

The crystal structure parameters were refined by Rietveld analysis on the XRD spectra using RIETAN program [66] and Fullprof [67].

2.2.1 Rietveld analysis

Rietveld analysis is a technique to refine crystal structure parameters from angle-dispersive powder diffraction data, which uses a non-linear least squares algorithm. In Rietveld analysis, a set of variable $\boldsymbol{x}$, such as lattice constants, atomic coordinations, occupancies, Debye-Waller factors, and others, are optimized to minimize the sum of weighted squares of residuals

$$S(\boldsymbol{x}) = \sum_{i=1}^{N} w_i [y_i - f_i(\boldsymbol{x})]^2, \tag{2.1}$$

where i is the number of diffraction point, w_i is the statistical weight, y_i is the observed intensity, and $f(\boldsymbol{x}) \equiv f(2\theta_i; x_1, x_2, \cdots, x_\mathrm{n})$ is the calculated intensity at a diffraction angle of $2\theta_i$. The calculated intensity $f(\boldsymbol{x})$ is composed of contributions from Bragg reflections and background correction $y_\mathrm{b}(2\theta_i)$ and is described as

$$f_i(\boldsymbol{x}) = S_\mathrm{R}(\theta_i) A(\theta_i) D(\theta_i) s \sum_K m_K |F(\boldsymbol{h}_K)|^2 P_K L(\theta_K) G(\Delta 2\theta_{iK}) + y_\mathrm{b}(2\theta_i) \tag{2.2}$$

where S_R is a correction factor for surface roughness, $A(\theta_i)$ is a transmission coefficient, $D(\theta_i)$ is a correction factor for the constant irradiation width, s is a

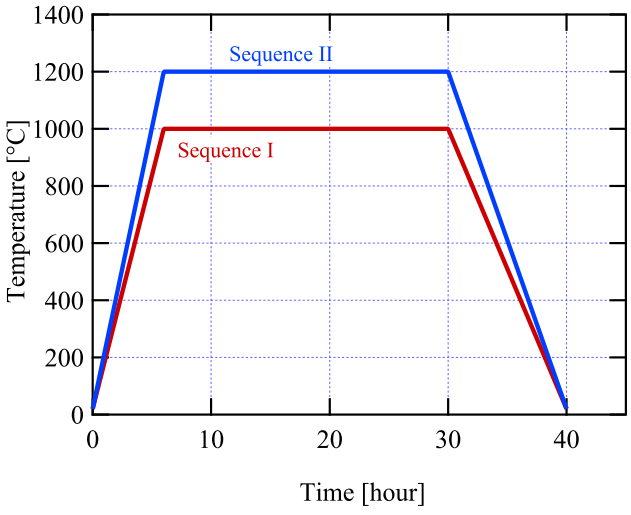

Figure 2.1: Temperature sequences of the preparation for $SrLaCuSb_{1-x}Nb_xO_6$.

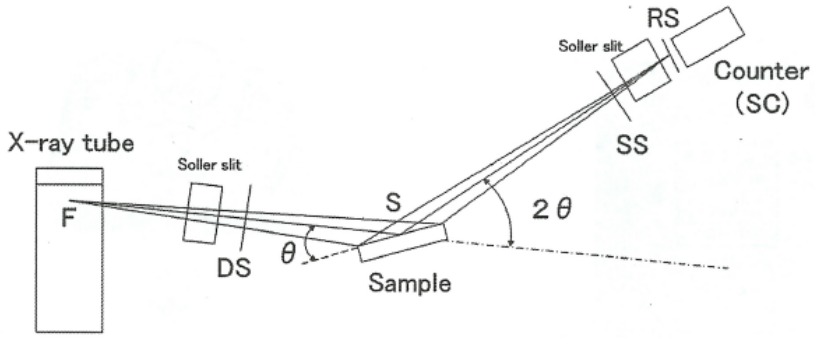

Figure 2.2: Optical system of the MiniFlex II. DS, SS, RS correspond to divergence, scattering, and reception slits, respectively. Reprinted from Ref. [65].

scale factor for the particular phase, K is a reflection number, m_K multiplicity, $F(\boldsymbol{h}_K)$ is a structure factor, $\boldsymbol{h}_K$ is a set of reflection indices hkl, P_K is a correction factor for preferred orientation, $L(\theta_K)$ is a Lorentz and polarization factor, θ_K is a Bragg angle, and $G(\Delta 2\theta_{iK} \equiv G(2\theta_i - 2\theta_K)$ is a profile function. In this study, the Modified split pseudo-Voigt function [68] was used as the profile function.

2.3 Neutron powder diffraction measurement

As compared to powder X-ray diffraction experiments, neutron powder diffraction (NPD) is a very effective method for studying materials containing light elements and magnetic materials [69]. X-rays are scattered by electron clouds, and the scattering cross sections are proportional to the atomic number. Therefore, scattering from light elements is weaker than that from heavy elements, and quantitative analysis of light elements is often difficult with X-ray scattering techniques. In addition, the scattering intensity decreases with increasing scattering angle, reflecting the shape of the electron cloud. On the other hand, since neutrons do not have any charge, scattering is caused by atomic nuclei. The nuclear scattering length is independent of the atomic number, resulting in large scattering cross sections for light elements. Thus, it is possible to distinguish between light elements with similar atomic numbers. Furthermore, neutron scattering has the advantage that the scattering intensity does not decrease as the scattering angle increases.

Since neutrons are spin-1/2 particles, they scattered through dipole interactions with magnetic moments in the sample. By observing this magnetic scattering, magnetic structure can be investigated. The magnetic structure analysis is to determine the magnetic structure factor $\boldsymbol{F}_m(\boldsymbol{Q})$ of the scattering cross section

$$\frac{\mathrm{d}\sigma}{\mathrm{d}\Omega} = r_m^2 g^2 \left|f(\boldsymbol{Q})\right|^2 e^{-2W(\boldsymbol{Q})} \sum_{ij} (\delta_{ij} - \hat{Q}_i \hat{Q}_j) \left|\boldsymbol{F}_m(\boldsymbol{Q})\right|^2, \tag{2.3}$$

$$\boldsymbol{F}_m(\boldsymbol{Q}) = \sum_{r_l} \boldsymbol{m}_r e^{i\boldsymbol{Q}\cdot\boldsymbol{r}_l}$$

where r_m is the characteristic magnetic scattering length, g is the Landé g-factor, $f(\boldsymbol{Q})$ is the magnetic shape factor, $e^{-2W(\boldsymbol{Q})}$ is the Debye–Waller factor, and $\boldsymbol{Q}$ is the scattering vector.

2.3.1 Neutron time-of-flight spectroscopy

The necessary condition for neutron diffraction is known as Bragg's law $\lambda = 2d_{hkl}\sin\theta$. There are two approaches to measure the powder neutron diffraction spectrum $I(d)$.

(a) to use a monochromatic incident beam and sweep a Bragg angle.

(b) to use a polychromatic incident beam with a fixed Bragg angle.

Method (a) is the conventional angular dispersive method, and method (b) is the time-of-flight (TOF) method.

A schematic setup for NPD experiments using the TOF method with a pulsed spallation neutron source is shown in Fig. 2.3. The neutron experiments have been conducted using the SuperHRPD(BL08) time-of-flight diffractometer installed at the Material and Life Science Facility (MLF) at J-PARC, Japan [70, 71]. In the MLF, accelerated protons strike a mercury target to produce high-energy neutrons through a spallation reaction. The high-energy neutrons are moderated by a hydrogen-rich moderator and then utilized as a white pulsed neutron beam for NPD measurements.

As shown in Fig. 2.3, a number of detectors are arranged around the sample. Since the white neutron beam contains neutrons with various wavelengths, the Bragg condition can be satisfied for various lattice spacings d at a fixed scattering angle. If the distance from the moderator through the sample to the detector is L, the neutron velocity $v = L/t$ can be determined by measuring the time t. From de Broglie's relation, the wavelength of the neutron

corresponding to the velocity v can be obtained as $\lambda = \frac{ht}{mL}$, where h is Planck constant and m is the mass of the neutron. The lattice spacing d can be calculated from Bragg's condition as follows;

$$d = \frac{ht}{2mL\sin\theta} \tag{2.4}$$

The TOF-type neutron diffractometer using a pulsed neutron source can efficiently collect the neutron spectrum $I(d)$ by measuring the time of flight. The resolution $\Delta d/d$ can be expressed as

$$\frac{\Delta d}{d} = \sqrt{\left(\frac{\Delta t}{t}\right)^2 + \left(\frac{\Delta L}{L}\right)^2 + \left(\frac{\Delta\theta}{\theta}\right)} \tag{2.5}$$

To improve the resolution, the flight distance L should be increased and the scattering angle 2θ should be closer to 180 degrees.

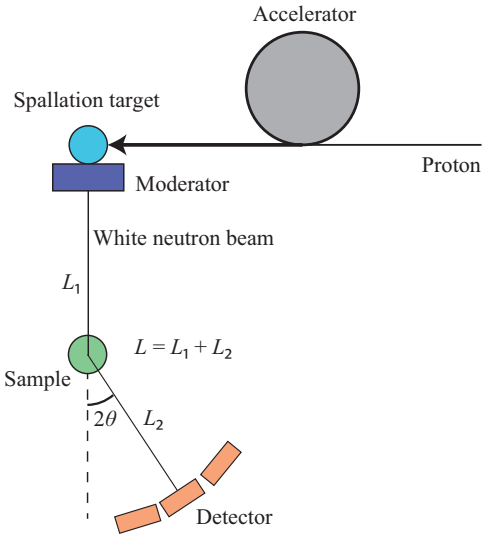

Figure 2.3: Schematic illustration of the experimental environment for the NPD measurement using TOF method with a pulsed spallation source.

2.4 Magnetization measurement

Temperature dependence of the magnetic susceptibility and the magnetic field dependence of the magnetization of pellet samples were measured in magnetic fields of up to 7 T at the temperature range $1.8 - 300\,\mathrm{K}$ using a SQUID magnetometer (Quantum Design MPMS XL). To prevent scattering of the sample powder, approximately 100 mg of sample was covered with nonmagnetic alu-

minum foil and placed in the center of the straw as shown in Fig. 2.4. Figure 2.5 shows a schematic illustration of a detection system with MPMS. The sample was inserted in the center of the pickup coil.

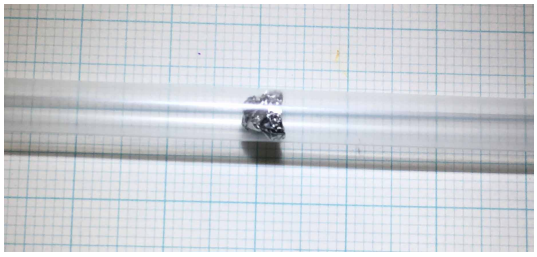

Figure 2.4: Picture of the sample covered with nonmagnetic aluminum foil.

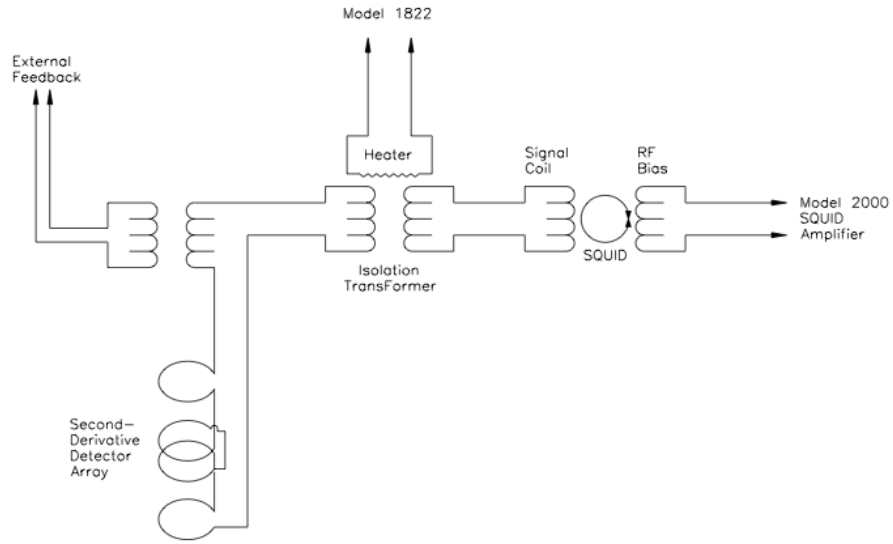

Figure 2.5: Schematic illustration of the detection system with MPMS [72].

Figure 2.6 shows a pickup coil in MPMS and SQUID response. A pickup coil is a quadruple superconducting coil, in which two single-coil is placed in the top and bottom, and a clockwise double coil is placed in the middle. Such a structure rejects signals from a uniform and linearly varying fields along the longitudinal axis. The superconducting current induced by the movement of the sample through the pickup coil is transmitted to the "Signal Coil" of the SQUID via the superconducting transformer and is converted into magnetic flux. This magnetic flux is converted into a voltage by the rf-SQUID and outputted. Since the magnetic flux penetrating the SQUID is quantized so

as to be an integral multiple of the quantum flux, it is possible to detect magnetic flux in the quantum flux unit with SQUID. The voltage output from rf-SQUID has the shape as shown on the right side of Fig. 2.6, and by fitting it, the absolute value of magnetization can be measured.

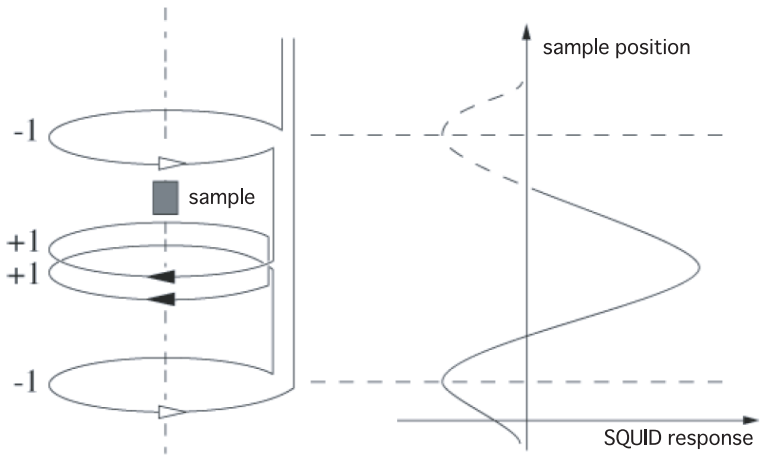

Figure 2.6: Schematic illustration of a pickup coil and SQUID response [72].

2.5 Specific heat measurement

Specific heat measurement was performed down to 0.34 K in magnetic fields of up to 9 T by the relaxation method using Physical Property Measurement System (PPMS, Quantum Design Co., Ltd.) with ^{3}He refrigerator. Figure 2.7 shows the schematic diagram of the sample platform for the specific heat measurement.

The sample was mounted to the sample platform with a small amount of Apiezon-N grease, achieving good thermal contact between the sample and the platform. A small heater and thermometer were installed in the sample platform, and four connecting wires provide thermal and electrical connection to the thermal bath. Since the platform is under vacuum, the heat given to the sample by the heater is conducted only by the four conducting lines.

2.5.1 Theory of the relaxation method: Simple model

In the case of no thermal resistance between the sample and the platform, the thermal system can be represented as Fig. 2.8. The heat balance can be

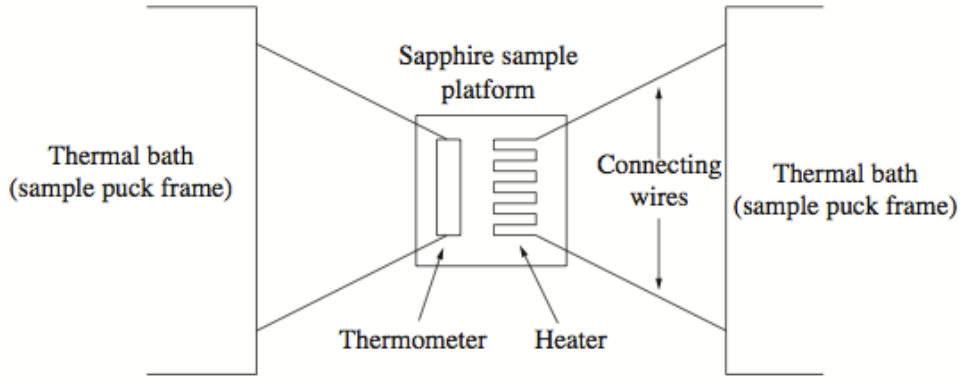

Figure 2.7: Schematic diagram of sample platform for specific heat measurement [73].

described by the following thermal diffusion equations;

$$(C_{\rm s} + C_{\rm p})\frac{dT}{dt} = P(t) - K_{\rm w}(T - T_{\rm b}), \tag{2.6}$$

where $C_{\rm s}$, $C_{\rm p}$, $K_{\rm w}$, $P(t)$, T and $T_{\rm b}$ are specific heat of the sample, specific heat of the platform, thermal conductivity between the platform and thermal bath, time revolution of heater power, temperature of sample, and temperature of heat bath, respectively. When rectangular heat as shown in Fig. 2.9 (a) is applied to the sample, the temperature changes as shown in Fig. 2.9(b) or (c).

In a conventional relaxation method, relaxation curves are measured over a sufficient amount of time until the temperature of the sample reaches a constant value, as shown in Fig. 2.9 (b). The time constant τ is obtained from the relaxation curve, and the total specific heat of $C_{\rm s}$ and $C_{\rm p}$ is calculated from the relation of $C_{\rm s} + C_{\rm p} = \tau K_{\rm w}$. $C_{\rm p}$ can be obtained by using the same method without installing samples, and then C_s is finally obtained by subtracting $C_{\rm p}$.

In a relaxation method with PPMS, a short heat pulse is used to shorten the measurement time so that the relaxation curve has a shape as shown in Fig. 2.9(c). Sample specific heat $C_{\rm s} + C_{\rm p}$ is obtained by the non-linear least-squares fitting to the relaxation curve by using Eq. (2.6). It is noted that in the temperature region crossing the first order phase transition, the relaxation curve is disturbed, as shown in Fig. 2.9(d), so specific heat can not be measured by the relaxation method.

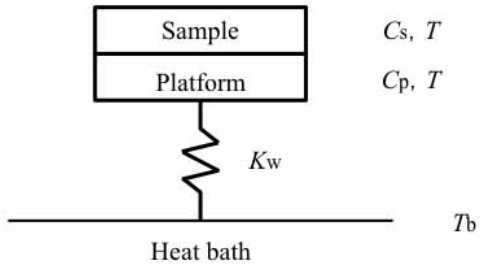

Figure 2.8: Schematic diagram of thermal system without thermal resistance.

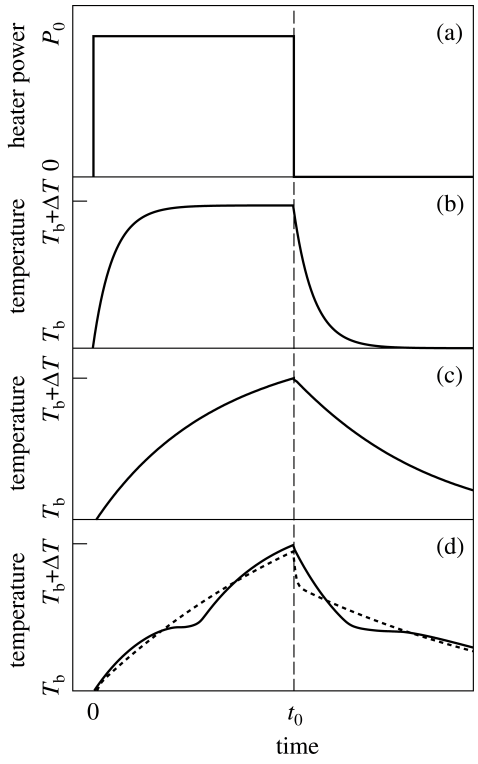

Figure 2.9: (a) Time dependent of heater power. (b) Temperature variation of sample when waiting sufficiently for relaxation, (c) when heater is turned off quickly, and (d) when crossing first-order phase transition [74]

2.5.2 Theory of the relaxation method: Two-Tau model

In the low-temperature region, thermal difference and thermal resistance between the sample and the platform can no longer be ignored. In this case, it is plausible to consider that a thermal system is thermally divided into the sample and the platform, as shown in Fig. 2.11. Then, the heat flow equations can be given by the following thermal diffusion equations;

$$C_{\mathrm{s}}\frac{dT_{\mathrm{s}}}{d_t} = -K_{\mathrm{g}}(T_{\mathrm{s}}(t) - T_{\mathrm{p}}(t)), \tag{2.7}$$

$$C_{\mathrm{p}}\frac{dT_{\mathrm{p}}}{dt} = P(T) - K_{\mathrm{b}}(T_{\mathrm{p}}(t) - T_{\mathrm{b}}) + K_{\mathrm{g}}(T_{\mathrm{s}}(t) - T_{\mathrm{p}}(t)), \tag{2.8}$$

where T_{s}, T_{p}, and K_{g} are the temperature of the sample, the temperature of the platform, and a thermal conductivity between the sample and the platform, respectively. The solution of Eq. (2.8) is represented by the superposition of the exponential function with the time time constant of $\tau_1 = 1/(\alpha - \beta)$ and the exponential function with the time constant of $\tau_2 = 1/(\alpha + \beta)$, where the τ_1 and τ_2 are described as

$$\alpha = \frac{K_{\mathrm{w}}}{2C_{\mathrm{p}}} + \frac{K_{\mathrm{g}}}{2C_{\mathrm{p}}} + \frac{K_{\mathrm{g}}}{2C_{\mathrm{s}}}, \tag{2.9}$$

$$\beta = \frac{\sqrt{K_{\mathrm{g}}^2C_{\mathrm{s}}^2 + 2K_{\mathrm{g}}^2C_{\mathrm{s}}C_{\mathrm{p}} + K_{\mathrm{g}}^2C_{\mathrm{p}}^2 + K_{\mathrm{w}}^2C_{\mathrm{s}}^2 + 2K_{\mathrm{w}}C_{\mathrm{s}}^2K_{\mathrm{g}} - 2K_{\mathrm{w}}C_{\mathrm{s}}K_{\mathrm{g}}C_{\mathrm{p}}}}{2C_{\mathrm{p}}C_{\mathrm{s}}}. \tag{2.10}$$

In particular, Eqs. (2.7) and (2.8) are subjected to Laplace transformation and the solution is given by

$$\begin{aligned} T_p(t) = {} & \frac{P_0}{K_b}\left[1 - \left(\frac{\tau - \tau_2}{\tau_1 - \tau_2}\right)e^{-\frac{t}{\tau_1}} - \left(\frac{\tau_1 - \tau}{\tau_1 - \tau_2}\right)e^{-\frac{t}{\tau_2}}\right]\left[\Theta(t) - \Theta\left(t - \frac{t'}{2}\right)\right] \\ & + \frac{P_0}{K_b}\left[(1 - e^{-\frac{t'}{2\tau_1}})\left(\frac{\tau - \tau_2}{\tau_1 - \tau_2}\right)e^{-\frac{t - t'/2}{\tau_1}} + (1 - e^{-\frac{t'}{2\tau_2}})\left(\frac{\tau_1 - \tau}{\tau_1 - \tau_2}\right)e^{-\frac{t - t'/2}{\tau_2}}\right] \\ & \times \Theta\left(t - \frac{t'}{2}\right) + T_0, \end{aligned} \tag{2.11}$$

where $\Theta(t)$ is a step function, and τ, τ_1, τ_2 are time constants. The time con-

stants are related to the specific heats as following equations,

$$\tau = \frac{C_s + C_p}{K_b} \tag{2.12}$$

$$\tau_1 = \frac{C_s}{2K_a} + \frac{C_s}{2K_b} + \frac{C_p}{2K_b} + \frac{\sqrt{C_s^2K_a^2 + C_s^2K_b^2 + C_p^2K_a^2 + 2C_s^2K_aK_b + 2C_sC_pK_a^2 - 2C_sC_pK_aK_b}}{2K_aK_b} \tag{2.13}$$

$$\tau_2 = \frac{C_s}{2K_a} + \frac{C_s}{2K_b} + \frac{C_p}{2K_b} - \frac{\sqrt{C_s^2K_a^2 + C_s^2K_b^2 + C_p^2K_a^2 + 2C_s^2K_aK_b + 2C_sC_pK_a^2 - 2C_sC_pK_aK_b}}{2K_aK_b} \tag{2.14}$$

The degree of sample coupling in this model is evaluated by $A = 100 \times \frac{K_w}{K_w+K_g}$ %. When sample coupling A is 100%, it becomes the same as Single Time Constant Model. In the specific heat measurement with PPMS, a fit to the solution of the Simple Model and of the Two − Tau Model are performed. The values of the fitting parameter with the smallest deviation determine the heat capacity.

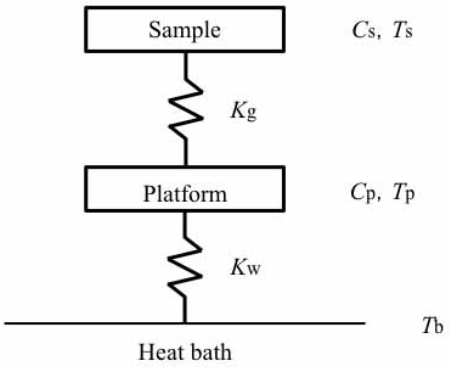

Figure 2.10: Schematic diagram of thermal system in the presence of thermal resistance.

2.6 Electron spin resonance measurement

The electron spin resonance (ESR) experiments were performed to evaluate the magnetic g-factor. The experiments were carried out at room temperature with JES-TE200 ESR SPECTROMETER manufactured by JEOL, Ltd.

When a magnetic field H is applied to an electron with $S = 1/2$, the degenerated energy level splits into two non-degenerate levels, $S_z = +1/2$ and $S_z = -1/2$, owing to the Zeeman effect. The difference between the two levels is given by $\Delta E = g\mu_{\mathrm{B}}H$, where μ_B is the Bohr magneton. When the energy equal to this energy difference ΔE is given externally by applying microwave, the electron dipole transition occurs. The resonance condition is described as the following equation.

$$h\nu = g\mu_B H, \tag{2.15}$$

where h means the Planck constant. This equation is fundamental equation for ESR.

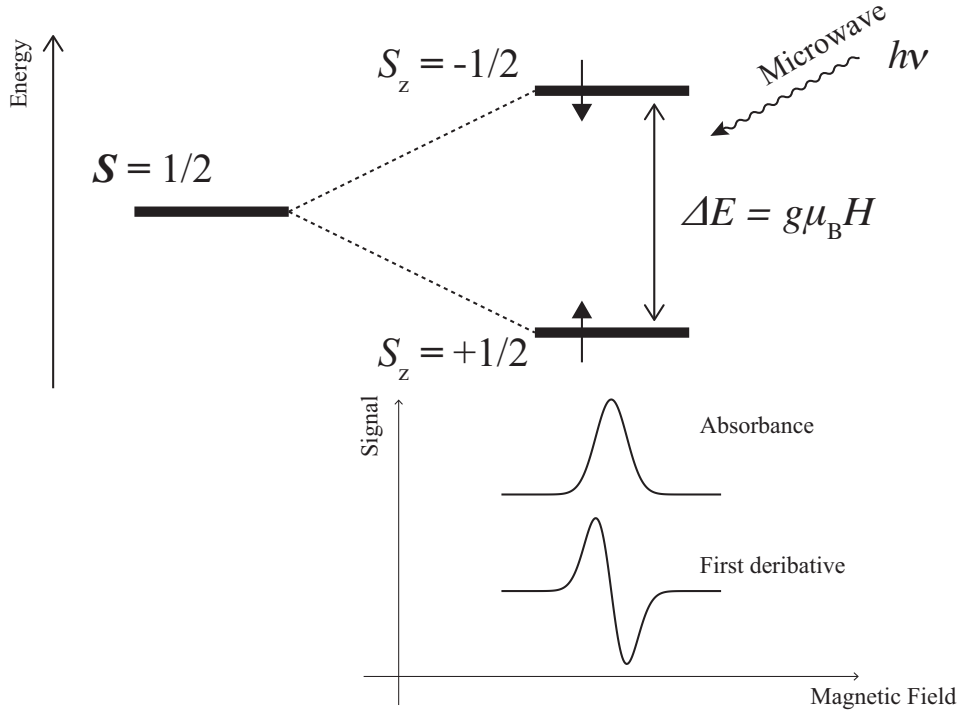

Figure 2.11: Principle of electron spin resonance.

A schematic picture of the experimental setup is shown in Fig. 3.7. A water cooling electromagnet applies magnetic fields of up to 2 T. The monochromatic microwave of the X-band frequency ($\sim$ 9 GHz) is introduced into the cavity

through the waveguide. The intensity of microwave signals from the cavity was monitored while sweeping the magnetic field. An oscillating magnetic field is applied along the external magnetic field so that the field-derivative of absorption signal is recorded. From the resonant spectrum obtained, the magnetic g-factor can be determined. From the line width of ESR signals, the magnitude of magnetic anisotropy is estimated.

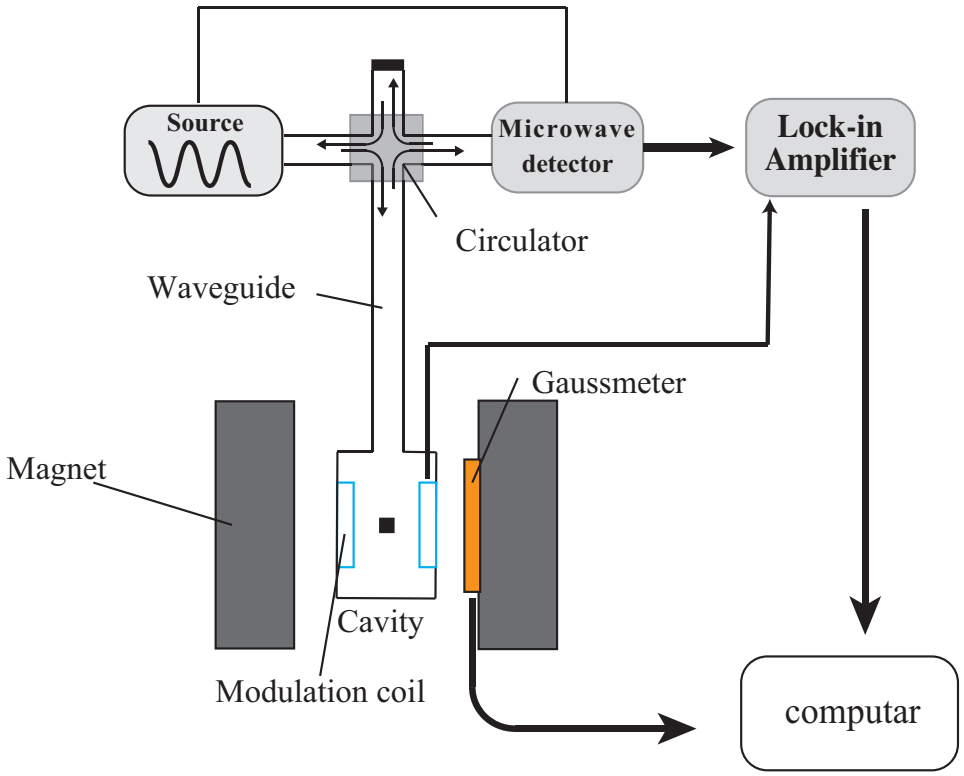

Figure 2.12: Schematic diagram of an ESR spectrometer.

2.7 Muon spin relaxation measurement

The muon spin rotation and relaxation (μSR) method is a very powerful probe for observing not only the static but also the dynamic properties of the internal magnetic field in the matter [75]. μSR measurements have the advantage of using a polarized spin beam, which can be performed in a zero field without an external magnetic field. The time window of μSR is 10^{-5} to 10^{-9} seconds, which is complementary to that of neutron scattering and NMR measurements. In the following, I will explain the principle and outline of μSR measurement.

The muon

In μSR measurements, muons, which are the charged leptons, are used as local magnetic probes. The positive muon has spin-1/2 and elementary charge e. The muon can be artificially produced by using the following pion decay process.

$$\pi^+ \longrightarrow \mu^+ + \nu_\mu \tag{2.16}$$

Since the pion decay process is due to weak interaction, the parity is not conserved. The resulting muon neutrino has helicity $h = \boldsymbol{p} \cdot \boldsymbol{s} = -1$, where $\boldsymbol{p}$ and $\boldsymbol{s}$ are momentum and spin, respectively. Since the spin of charged pions is zero, the direction of the spin polarization of the emitted muon is in the opposite direction of propagation due to the conservation of angular momentum. Therefore, the positive muon beam obtained from the pion decay is almost 100% spin-polarized. In the MLF, J-PARC, where I performed the μSR measurements, pions are produced by accelerated protons impinging a graphite target [76].

Since muons are charged particles, they lose their kinetic energy by repeated Coulomb scattering after being injected into the matter, and eventually come to rest at a location with low electrostatic potential. The stopped muon feels the local magnetic field and exhibits a precessional motion. The muon decays into a positron and two neutrinos;

$$\mu^+ \longrightarrow \mathrm{e}^+ + \nu_\mathrm{e} + \bar{\nu}_\mu, \tag{2.17}$$

where ν_e and $\bar{\nu}_\mu$ are the electron neutrino and muon antineutrino. The μSR measurement can reveal the nature of the local magnetic field by observing this precessional motion. The energy E of the emitted positron has a continuous

distribution because this decay process is a three-body problem. The spatial density distribution spectrum $W(\theta, \varepsilon)$ of positrons is given by

$$W(\theta, \varepsilon) = \frac{\mathrm{d}^2 N}{\mathrm{d}(\cos\theta)\mathrm{d}\varepsilon} \simeq \varepsilon^2(3 - 2\varepsilon)\left(1 + \frac{2\varepsilon - 1}{3 - 2\varepsilon} P_\mu \cos\theta\right) \tag{2.18}$$

, where θ is the angle between the muon spin $\boldsymbol{I}$ and the momentum $\boldsymbol{p}$ of the emitted positron, P_μ is the polarization of the muon, and ε is the ratio of the energy of the emitted positron to $E_{\max}$ as

$$\cos\theta \equiv \frac{\boldsymbol{I}}{I} \cdot \frac{\boldsymbol{p}}{p}, \ \varepsilon \equiv \frac{E}{E_{\max}}. \tag{2.19}$$

For the detection of positrons in all energy ranges, integrating Eq. 2.18 with respect toε yields

$$W(\theta) \simeq 1 + \frac{1}{3} P_\mu \cos\theta. \tag{2.20}$$

It is clearly demonstrated that positrons are frequently emitted in the direction of the muon spin, as shown in Fig. 2.13. By measuring the spatial "asymmetry" of the emitted positrons, the direction of the muon spin can be determined. Furthermore, by measuring the time evolution of the asymmetry, it is possible to clarify the static and dynamical properties of the internal magnetic fields by detecting a precession of the muon spin.

Principle of the μSR measurement

Figure 2.14 shows a schematic illustration of a standard setup of μSR measurements. In the ZF μSR measurement, the positrons associated with muon decay are counted by the forward and backward counters to probe internal magnetic fields in the sample. Here, I present an overview of the principle of the μSR measurement. $t = 0$ is defined as the time when the muon stopped in the sample. Let $N(t, \boldsymbol{n}_{\mathrm{c}})$ be the number of positrons measured by the counter covered by the solid angle $\mathrm{d}\Omega$ subtended from the sample to the counter between time t and $t + \Delta t$. The number of muons in the sample at t $N_\mu(t)$ is given by

$$N_\mu = N_\mu^0 \exp\left(-\frac{t}{\tau_\mu}\right), \tag{2.21}$$

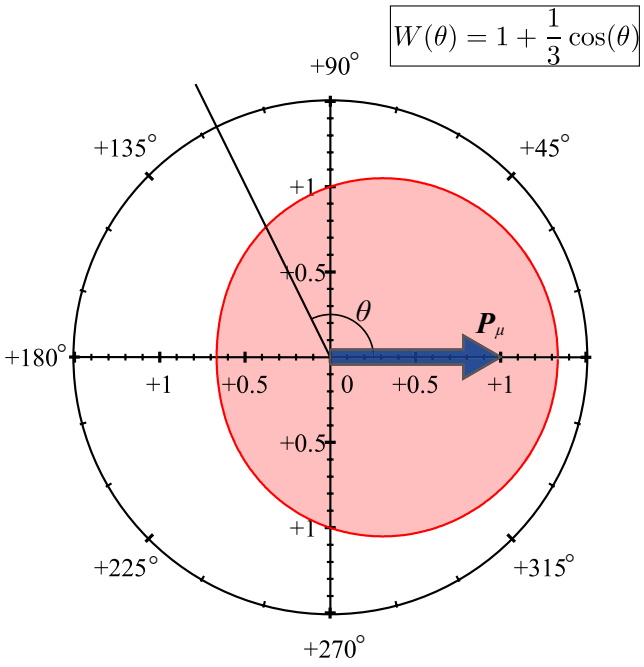

Figure 2.13: Angular distribution of positrons emitted in the decay of positive muons in a polar plot. The arrows indicate the muon polarization vector.

where τ_μ is the lifetime of the muon and N_μ^0 is the number of muons in the sample at $t = 0$. The number of positrons $N(t, E, \boldsymbol{nc})\mathrm{d}t\mathrm{d}t\mathrm{d}\Omega$ whose energy is from E to $E + \mathrm{d}E$ between time t and $t + \mathrm{d}t$ is obtained from Eq. 2.18 as

$$N(t, E, \boldsymbol{n}_\mathrm{c})\mathrm{d}E\mathrm{d}t\mathrm{d}\Omega = N_\mu^0 \exp\left(-\frac{t}{\tau_\mu}\right) \varepsilon^2(3 - 2\varepsilon)\left[1 + \frac{3\varepsilon - 1}{3 - 2\varepsilon}\frac{\langle I(t)\rangle}{I} \cdot \boldsymbol{n}_\mathrm{c}\right] \mathrm{d}\varepsilon\frac{\mathrm{d}t}{\tau_\mu}\mathrm{d}\Omega, \tag{2.22}$$

where $\boldsymbol{I}/I$ is an unit vector along to the muon spin, and $\varepsilon = E/E_\mathrm{max}$ is a ratio of the muon energy E to the maximum energy E_max of muons. The muon spin polarization at time t is

$$\boldsymbol{P}(t) = (P_x(t), P_y(t), P_z(t)) = \left(\frac{\langle I_x\rangle}{I}, \frac{\langle I_y\rangle}{I}, \frac{\langle I_z\rangle}{I}\right). \tag{2.23}$$

When positrons with energies above the cutoff E_c are detected, the counting rate of positrons associated with muon decay is described as

$$N(t, \boldsymbol{n}_\mathrm{c}) = \int_{\varepsilon_\mathrm{c}}^{1} \mathrm{E} \int \mathrm{d}\Omega N(t, E, \boldsymbol{n}_c) \tag{2.24}$$

$$= N_0 \exp\left(-\frac{t}{\tau_\mu}\right)\left[1 + \bar{A}\boldsymbol{P}(t) \cdot \boldsymbol{n}_\mathrm{c}\right], \tag{2.25}$$

where $\bar{A}$ is an anisotropy parameter averaged over the energy of the measured positron and the solid angle covered by the counter. Note that $\bar{A}$ is independent of the sample.

Let N_{F} and N_{B} be the count rates measured at time t by the forward and backward counters, respectively. Integrating Eq. 2.25 over the solid angle covered by the detecter, the following equations are obtained;

$$N_{\mathrm{F}}(t) = N(t, \theta = 180^{\circ}) = N_{\mathrm{F}}(0) \exp\left(-\frac{t}{\tau_{\mu}}\right)\left[1 - \bar{A}P_z(t)\right] \tag{2.26}$$

$$N_{\mathrm{B}}(t) = N(t, \theta = 0^{\circ}) = N_{\mathrm{B}}(0) \exp\left(-\frac{t}{\tau_{\mu}}\right)\left[1 + \bar{A}P_z(t)\right], \tag{2.27}$$

where z-axis is defined as a direction of the polarization direction of the incident muon beam. The "asymmetry" $A(t)$ to be analyzed in the μSR measurement is

$$A(t) \equiv \frac{N_{\mathrm{B}}(t) - \alpha N_{\mathrm{F}}(t)}{N_{\mathrm{B}}(t) + \alpha N_{\mathrm{F}}(t)} = AP_z(t) = AP(0)G_z(t), \tag{2.28}$$

where $G_z(t)$ is the longitudinal relaxation function of the muon spin. This result indicates that the local magnetic field in the sample can be detected by measuring the asymmetry since the longitudinal relaxation function of the muon spin reflects the electronic state in the sample. In the case with LF μSR measurements, longitudinal magnetic fields were applied along to the z-axis. By measuring the decoupling process of muon spins from the internal field by applied longitudinal magnetic fields, it is possible to evaluate the magnitude of the internal field and to clarify the nature of the fluctuations of the internal field.

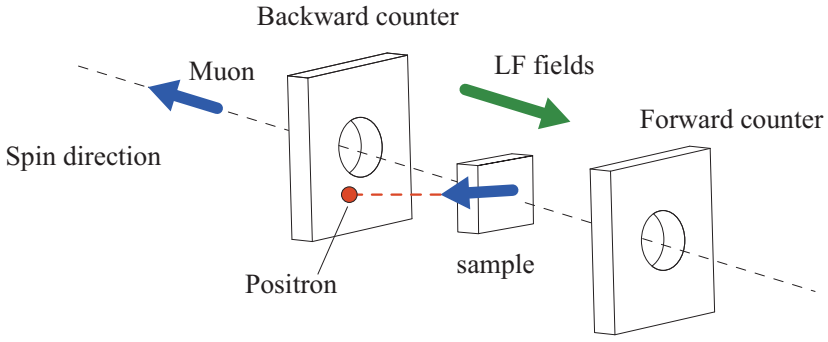

Figure 2.14: Schematic illustration of μSR experimental geometry.

Chapter 3

Effect of Weak Bond Randomness in Spin-1/2 J_1-J_2 Quasi-Square-Lattice Heisenberg Antiferromagnets: $SrLaCuSbO_6$ and $SrLaCuNbO_6$

To clarify the effect of exchange randomness on the quantum frustrated antiferromagnets, it is essential to cultivate a series of materials in which bond randomness can be easily and systematically controlled. Copper oxides A_2CuBO_6 with a B-site ordered double perovskite structure, which has presented novel properties by the combination of A- and B-site ions, have attracted much attention. In particular, I have focused on $SrLaCuMO_6$, in which the A-site is randomly occupied by Sr^{2+} and La^{3+} ions. For example, it has been pointed out that the bond randomness effect is caused by the structural disorder in QSL candidate $YbMgGaO_4$. The bond randomness effect is expected to appear in $SrLaCuMO_6$ due to a similar mechanism in $YbMgGaO_4$.

In this chapter, I will discuss the magnetic properties of $SrLaCuSbO_6$ and $SrLaCuNbO_6$ based on the results of magnetization, specific heat, neutron diffraction, ESR, and μSR measurements.

3.1 Introduction

3.1.1 $S = 1/2$ Square-Lattice $J_1 - J_2$ Heisenberg model

The square lattice $J_1 - J_2$ Heisenberg model with the nearest-neighbor interaction J_1 and next-nearest-neighbor interaction J_2 has been studied theoretically and experimentally. The Hamiltonian is given by

$$\mathcal{H} = J_1 \sum_{\langle i,j \rangle} \boldsymbol{S}_i \cdot \boldsymbol{S}_j + J_2 \sum_{\langle\langle i,j \rangle\rangle} \boldsymbol{S}_i \cdot \boldsymbol{S}_j, \tag{3.1}$$

where the summation in the first and second terms are taken over the nearest-neighbor and next-nearest-neighbor spin pairs, respectively. For the classical case, three types of ground states are realized, depending on the sign and ratio of J_2 to J_1. When the antiferromagnetic J_2 is dominant, a columnar antiferromagnetic (CAF) state is stabilized independently of the sign of J_1, while when J_1 is dominant, antiferromagnetic J_1 induces a Néel antiferromagnetic (NAF) state, and ferromagnetic J_1 induces a ferromagnetic (FM) state. For quantum spins with $S = 1/2$, on the other hand, a quantum disordered ground states appear near the CAF/NAF and CAF/FM boundaries. Figure 3.1 shows a phase diagram of ground states for quantum spins. The QDGS has been predicted to emerge in a critical range of $\alpha_1 < J_1/J_2 < \alpha_2$ with $\alpha_1 \simeq 0.4$ and $\alpha_2 \simeq 0.6$ [77–101]. However, no theoretical consensus has been achieved on the nature of the ground state, even for the existence of an excitation gap. For $J_1 < 0$ a spin nematic state is theoretically predicted [92], while for $J_1 > 0$, theories predict various gapped nonmagnetic states such as the columnar valence bond crystal (VBC) [93–95, 97, 98], the plaquette VBC [78, 84, 87, 95, 99], Z_2 spin liquid[86, 101]. Some theoretical studies suggest that the intermediate disordered state is gapless [77, 96, 100].

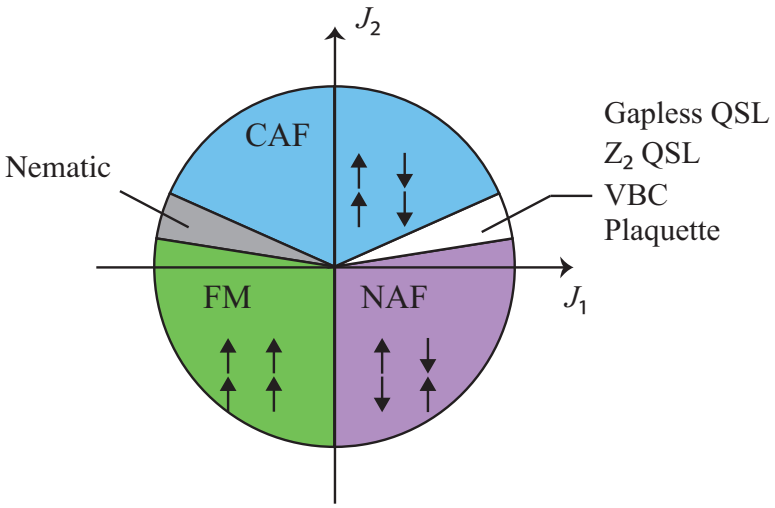

Figure 3.1: Schematic phase diagram of the $S = 1/2$ square lattice $J_1 - J_2$ Heisenberg model. CAF, NAF, and FM indicate the columnar antiferromagnetic, Néel antiferromagnetic, and ferromagnetic states, respectively.

3.1.2 *B*-site Ordered Double Perovskites Sr_2CuMO_6 (M =Te^{6+}, W^{6+})

Crystal Structure

B-site ordered double perovskite Sr_2CuMO_6 (M =Te^{6+}, W^{6+}) [102] is one of the candidates for the $S = 1/2$ square lattice Heisenberg antifferomagnet (SLHAF). The crystal structure with space group $I4/m$ is illustrated in Fig. 3.2 (a). CuO_6 and MO_6 octahedra are arranged alternately in the *ab*-plane, sharing their corners as shown in Fig. 3.2 (b). The CuO_6 octahedra are elongated along the *c*-axis due to a Jahn–Teller effect.

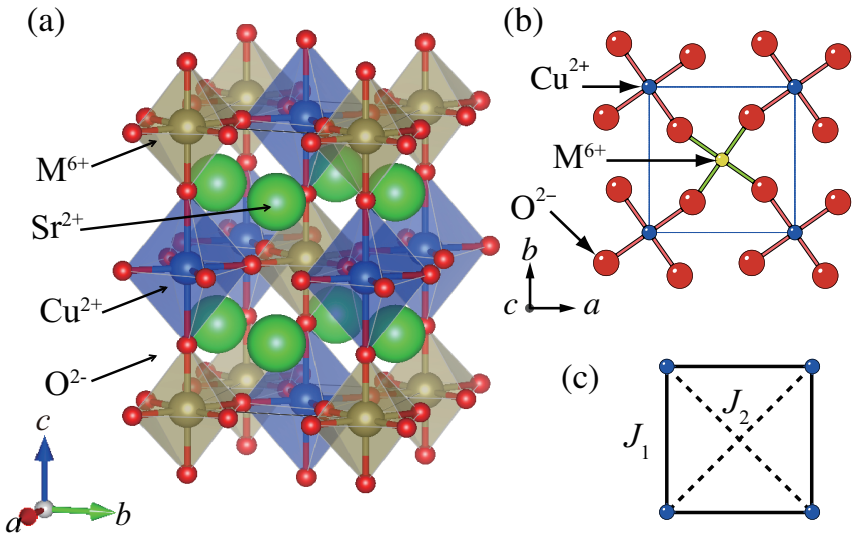

Figure 3.2: (a) Crystal structure of Sr_2CuMO_6. (b) Linkage of CuO_6 and MO_6 octahedral in the *ab*-plane of Sr_2CuMO_6. (c) Illustration of exchange interaction between Cu^{2+} ions.

The electronic configuration of Cu^{2+} is [Ar]$3d^9$ that is equivalent to one hole occupying the $3d$ orbital. In Sr_2CuMO_6 (M =Te^{6+}, W^{6+}), Cu^{2+} is subjected to a crystal field by six octahedrally coordinated O^{2-} ions. The crystal field in an octahedral environment splits the five-hold degenerated $3d$ hole orbitals into the two-fold degenerated E_g and three-fold degenerated T_{2g} states. Moreover, tetragonal distortion by the Jahn-Teller effect lifts the degeneracy of E_g and T_{2g}, so that the $d(x^2 - y^2)$ orbital becomes the lowest in energy as shown in Figure 3.3. The hole of Cu^{2+} in B-site ordered double perovskites with Jahn-Teller distortion exists only on the $d(x^2 - y^2)$ orbital since the difference of energy between the B_{1g} ground state and the excited states is of order of 10^4 K.

Because hole orbitals $d(x^2-y^2)$ of Cu^{2+} ions with $S=1/2$ are spread in the ab-plane, exchange interaction is dominant in the ab-plane, while the interlayer exchange interaction becomes small. Non-magnetic Sr^{2+} ions are placed in the space among the CuO_6 and MO_6 octahedra. These features indicate a good two-dimensionality.

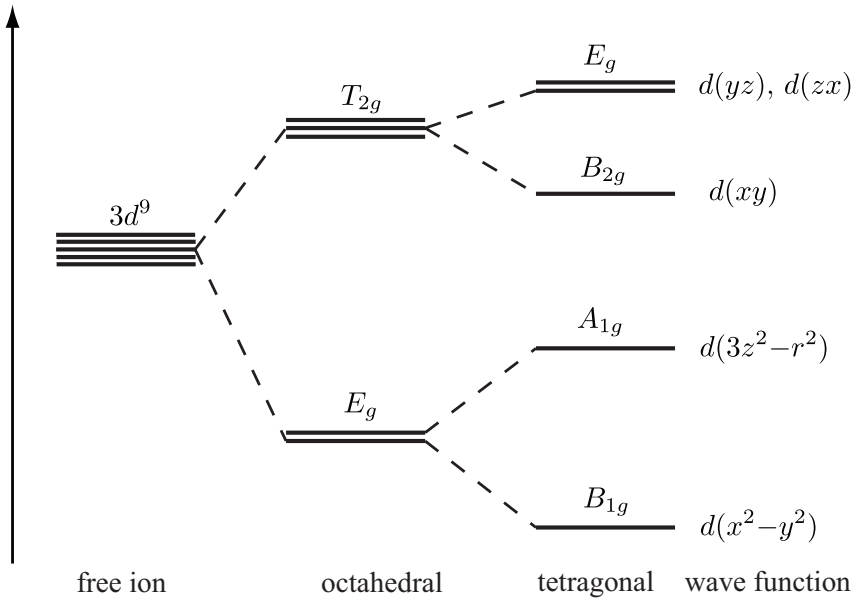

Figure 3.3: Energy levels of hole orbitals of the Cu^{2+} ion under octahedral and tetragonal crystalline fields.

Magnetic Properties of Sr_2CuMO_6 (M =Te^{6+}, W^{6+})

Sr_2CuMO_6 (M =Te^{6+}, W^{6+}) have been studied as a candidate material of the $S=1/2$ J_1-J_2 square lattice Heisenberg antiferromagnet. Sr_2CuWO_6 and Sr_2CuTeO_6 exhibit antiferromagnetic ordering at $T_N = 24$ [103] and 29 K [104, 105], respectively, due to the weak interlayer exchange interactions. The exchange interactions were evaluated as shown in Table 3.1 [106–108]. The previous studies suggest that J_1 is dominant in Sr_2CuTeO_6, while J_2 is dominant in Sr_2CuWO_6.

Table 3.1: Exchange interaction in Sr_2CuMO_6 (M =Te^{6+}, W^{6+})

		Ref. [108]	Ref. [106]	Ref. [109]	Ref. [107]
Sr_2CuTeO_6	J_1/k_B [K]	77	83	–	–
	J_2/k_B [K]	0	2.4	–	–
Sr_2CuWO_6	J_1/k_B [K]	–	–	22.6	14
	J_2/k_B [K]	–	–	91.2	110
Measurement		susceptibility	INS*	susceptibility	INS*

*Inelastic Neutron Scattering.

Neuton powder scattering experiments show that the columnar antiferromagnetic and Néel antiferromagnetic states are realized in Sr_2CuWO_6 [105] and Sr_2CuTeO_6 [103], respectively. This is in agreement with the fact that the dominant exchange interaction is J_2 in Sr_2CuWO_6, while J_1 is dominant in Sr_2CuTeO_6. The ordered magnetic moments in Sr_2CuTeO_6 and Sr_2CuWO_6 were found to be reduced to $0.696(6)\mu_B$ at 1.5 K and $0.57(1)\mu_B$ at 3 K, respectively, from the classical value of $1\mu_B$ due to the quantum fluctuations enhanced by the low-dimensionality [105, 108]. These moment size were consistent with theoretical calculations for quantum spin systems on square lattice [110, 111].

Koga *et al.* qualitatively explained this different magnetism in Sr_2CuTeO_6 and Sr_2CuWO_6 in the context of electronic states of the outermost filled orbital of the nonmagnetic M^{6+} [103]. In the Sr_2CuMO_6 system, J_1 can be considered to be the total of two super-exchange interactions via different paths. One of dominant paths is $Cu^{2+}-O^{2-}-O^{2-}-Cu^{2+}$, which is commonly antiferromagnetic in M =W and M =Te. The other dominant path is $Cu^{2+}-O^{2-}-M^{6+}-O^{2-}-Cu^{2+}$, which has different sign with respect to M =W and M =Te. This super-exchange interaction could be ferromagnetic for M = W, while it is antiferromagnetic for M =Te. In the case of M =Te, hole orbitals of Cu^{2+}, O^{2-}, and Te^{6+} are overlapped and form a molecular or-

bital since an outermost filled orbital of Te^{6+} is the d orbital. Two hole spins of Cu^{2+} ions occupy the same molecular orbital, which makes J_1 antiferromagnetic owing to the Pauli exclusion principle. On the other hand, in the case of $M =$W, since an outermost filled orbital of W^{6+} is the p orbital, hole orbitals of Cu^{2+} and O^{2-} forms two molecular orbitals with the p_x or p_y orbitals of W^{6+}. Two hole spins of Cu^{2+} ions occupy different molecular orbitals, which gives a ferromagnetic contribution to the J_1 owing to Hund's rule. Because antiferromagnetic super-exchange via $Cu^{2+}-O^{2-}-O^{2-}-Cu^{2+}$ path and ferromagnetic super-exchange via $Cu^{2+}-O^{2-}-W^{6+}-O^{2-}-Cu^{2+}$ path almost cancel out, the J_1 value of Sr_2CuWO_6 becomes smaller. For Sr_2CuTeO_6, super-exchange interactions via $Cu^{2+}-O^{2-}-O^{2-}-Cu^{2+}$ and $Cu^{2+}-O^{2-}-Te^{6+}-O^{2-}-Cu^{2+}$ paths are both antiferromagnetic, which leads to strong antiferromagnetic J_1 interaction.

Some theoretical studies by using *ab initio* calculations pointed out that Te outermost occupied $4d$ orbitals are core-like and hardly hybridize with the Cu $3d$ and the oxygen $2p$ orbitals [106]. $Cu^{2+}-O^{2-}-Te^{6+}-O^{2-}-Cu^{2+}$ could be negligible, while $Cu^{2+}-O^{2-}-O^{2-}-Cu^{2+}$ should be responsible for the predominant J_1. DFT+U calculations show that unoccupied W $5d$ orbitals are strongly hybridized with the oxygen p orbitals [112]. $Cu^{2+}-O^{2-}-W^{6+}-O^{2-}-Cu^{2+}$ through the $5d$ orbital of W is responsible for the predominant J_2.

In Sr_2CuMO_6, the nonmagnetic M ions give a significant effect on the magnetism. It is believed that the difference in the electronic state of M determines the size of J_1 and J_2, whereas there is no experimental evidence to explain this.

3.2 Experimental results

3.2.1 Crystal structure

Neutron powder diffraction (NPD) measurements were performed at 20 and 300 K using the SuperHRPD(BL08) time-of-flight diffractometer installed at the Material and Life Science Facility (MLF) at J-PARC, Japan [70, 71]. The crystal structures of SLCSO and SLCNO were refined using the high-resolution NPD profiles obtained from the backscattering (BS) bank by Rietveld analysis with the Fullprof program [113].

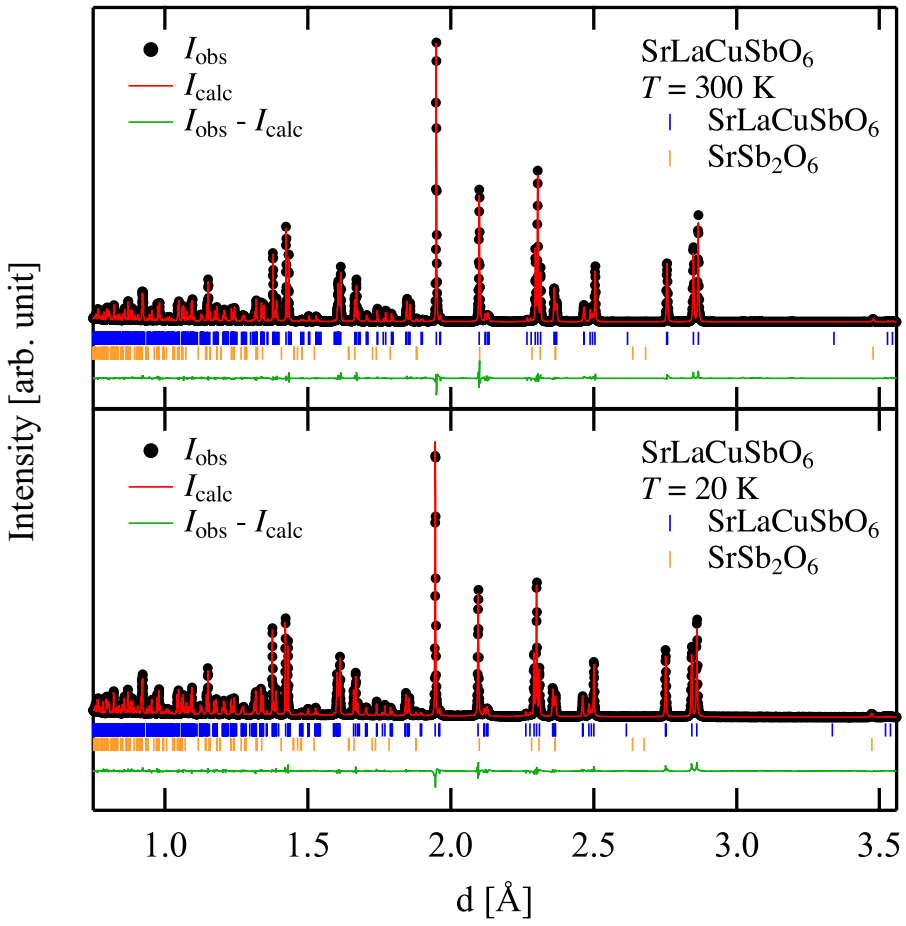

Figure 3.4: NPD patterns of SLCSO collected at 300 and 20 K, and the results of Rietveld fitting (red lines). Green curves show the differences between the observed and calculated intensities. A minor 0.96(3) wt% nonmagnetic impurity of $SrSb_2O_6$ was found.

Figure 3.4 shows NPD patterns for SLCSO collected from the BS bank at 300 and 20 K, and the results of Rietveld analysis. The analysis was based on the $P2_1/n$ structure reported by Attfield *et al.* [114]. It was found that

the SLCSO sample contains a minor 0.96(3) wt% nonmagnetic impurity of $SrSb_2O_6$. Also, there is no structural transition and SLCSO retains the $P2_1/n$ structure down to 3.8 K. The structural parameters obtained by Rietveld analysis are listed in Tables 3.2 and 3.3.

Table 3.2: Structural parameters of $SrLaCuSbO_6$ obtained by Rietveld analysis of neutron power diffraction spectra at 300 K.

300 K						
	Space group: $P2_1/n$ (No.14) $a = 5.51406(2)$ Å, $b = 5.510057(20)$ Å, $c = 8.39673(3)$ Å $\alpha = 90°$, $\beta = 90.4888(3)°$, $\gamma = 90°$ $R_p = 9.33\,\%$, $R_{wp} = 11.7\,\%$, $R_e = 2.26\,\%$ $R_B = 3.89\,\%$, $R_F = 3.08\,\%$					
Atom	Site	x	y	z	g	B_{iso}
Sr/La	4e	0.0109(2)	0.0207(2)	0.24859(14)	0.5/0.5	0.61(2)
Cu	2c	1/2	0	1/2	1	0.34(3)
Sb	2d	1/2	0	0	1	0.11(3)
O1	4e	0.2815(3)	0.2808(3)	0.03912(19)	1	0.84(3)
O2	4e	0.2218(3)	−0.2190(3)	0.03807(19)	1	0.84(3)
O3	4e	−0.0695(2)	0.4919(3)	0.27144(16)	1	0.65(2)

Table 3.3: Structural parameters of $SrLaCuSbO_6$ obtained by Rietveld analysis of neutron power diffraction spectra at 20 K.

20 K					
	Space group: $P2_1/n$ (No.14) $a = 5.504498(18)$ Å, $b = 5.503628(17)$ Å, $c = 8.38456(2)$ Å $\alpha = 90°$, $\beta = 90.5138(3)°$, $\gamma = 90°$ $R_p = 8.80\,\%$, $R_{wp} = 9.04\,\%$, $R_e = 0.88\,\%$ $R_B = 4.60\,\%$, $R_F = 3.22\,\%$				
Atom	x	y	z	g	B_{iso}
Sr/La	0.01099(19)	0.02336(20)	0.24861(12)	0.5/0.5	0.29(2)
Cu	1/2	0	1/2	1	0.17(2)
Sb	1/2	0	0	1	0.06(3)
O1	0.2829(3)	0.2834(3)	0.04046(18)	1	0.70(2)
O2	0.2203(3)	−0.2184(3)	0.03937(17)	1	0.67(3)
O3	−0.0724(2)	0.4909(3)	0.27164(15)	1	0.56(3)

Figure 3.5 shows NPD patterns for SLCNO collected from the BS bank at 300 and 20 K, and the results of Rietveld analysis. The analysis was performed based on a structural model with the space group $P\bar{1}$ reported by West and Davies [115]. Structural parameters of $SrLaCuTaO_6$ [115], which is isostructural with SLCNO, were chosen as initial parameters of Rietveld refinement, and the isotropic atomic displacement parameter B_{iso} was fixed for each type of atom. A minor 1.0(1) wt% nonmagnetic impurity of La_3NbO_7 was found. The structural parameters obtained by Rietveld analysis are listed in Table 3.4 and 3.5.

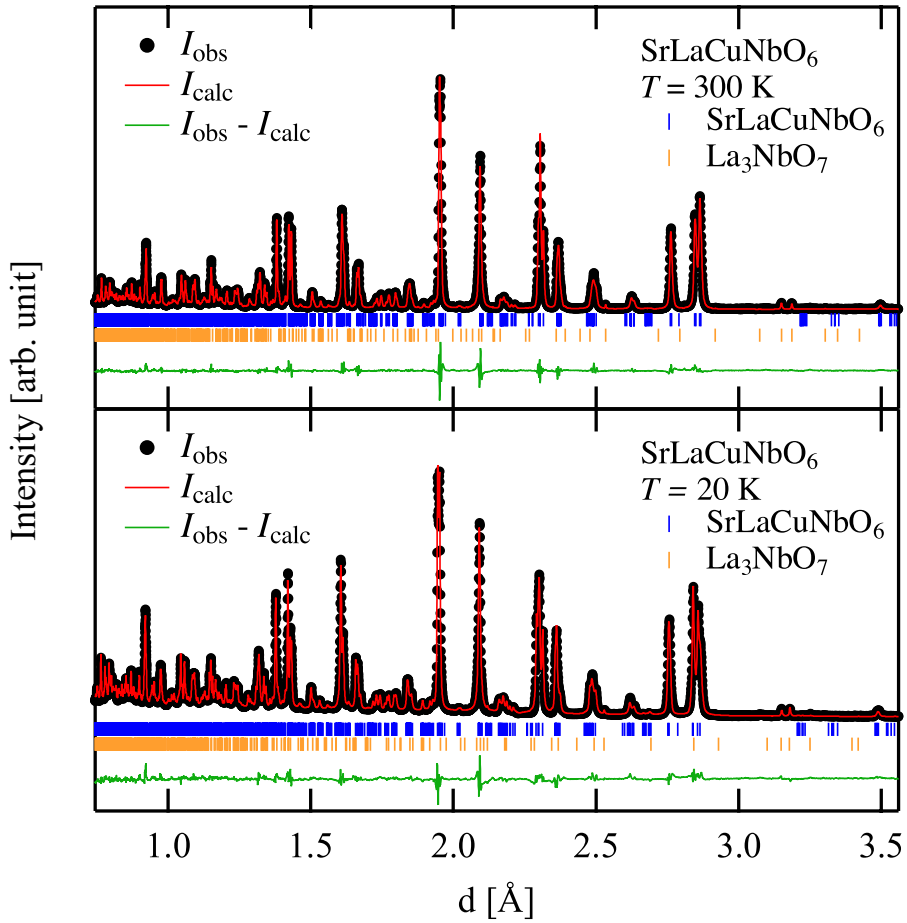

Figure 3.5: NPD patterns of SLCNO collected at 300 and 20 K, and the results of Rietveld fitting (red lines). Green curves show the differences between the observed and calculated intensities. A minor 1.0(1) wt% nonmagnetic impurity of La_3NbO_7 was found.

Table 3.4: Structural parameters of $SrLaCuNbO_6$ obtained by Rietveld analysis of neutron power diffraction spectra at 300 K.

300 K						
Space group: $P\bar{1}$ (No.2) $a = 7.80121(6)$ Å, $b = 7.82001(7)$ Å, $c = 8.36915(8)$ Å $\alpha = 89.6533(11)°$, $\beta = 89.6630(9)°$, $\gamma = 89.9235(9)°$ $R_p = 9.02\,\%$, $R_{wp} = 10.1\,\%$, $R_e = 2.44\,\%$ $R_B = 3.38\,\%$, $R_F = 5.09\,\%$						
Atom	Site	x	y	z	g	B_{iso}
Sr1/La1	2i	0.2499(16)	0.4855(15)	0.4960(15)	0.5/0.5	1.09(3)
Sr2/La2	2i	0.2525(16)	−0.0150(15)	0.4916(14)	0.5/0.5	1.09(3)
Sr3/La3	2i	0.2514(15)	0.4822(15)	−0.0195(12)	0.5/0.5	1.09(3)
Sr4/La4	2i	0.7529(15)	0.0155(15)	0.0136(14)	0.5/0.5	1.09(3)
Nb1	2i	0.004(2)	0.252(2)	0.7549(17)	1	0.24(6)
Nb2	2i	0.505(2)	0.255(2)	0.2515(18)	1	0.24(6)
Cu1	2i	0.003(2)	0.253(2)	0.2534(19)	1	0.61(5)
Cu2	2i	0.5002(20)	0.256(2)	0.7563(17)	1	0.61(5)
O11	2i	0.0400(18)	0.002(2)	0.2255(17)	1	1.11(2)
O12	2i	−0.0501(18)	0.2737(18)	−0.0145(15)	1	1.11(2)
O13	2i	−0.0311(18)	0.500(2)	0.2893(18)	1	1.11(2)
O14	2i	0.0356(18)	0.2113(18)	0.5187(15)	1	1.11(2)
O21	2i	0.2482(20)	0.2936(18)	0.2265(15)	1	1.11(2)
O22	2i	0.250(2)	0.2248(19)	0.7928(17)	1	1.11(2)
O23	2i	0.246(2)	0.7257(20)	0.2987(17)	1	1.11(2)
O24	2i	0.250(2)	0.7857(18)	0.7166(16)	1	1.11(2)
O31	2i	0.4625(19)	0.003(2)	0.2187(19)	1	1.11(2)
O32	2i	0.5292(19)	0.283(2)	0.0195(17)	1	1.11(2)
O33	2i	0.4530(18)	0.209(2)	0.4801(17)	1	1.11(2)
O34	2i	0.5301(18)	0.499(2)	0.2934(19)	1	1.11(2)

Table 3.5: Structural parameters of $SrLaCuNbO_6$ obtained by Rietveld analysis of neutron power diffraction spectra at 20 K.

20 K						
	Space group: $P\bar{1}$ (No.2) $a = 7.78131(5)$ Å, $b = 7.80553(5)$ Å, $c = 8.36347(7)$ Å $\alpha = 89.5094(8)°$, $\beta = 89.6578(6)°$, $\gamma = 89.9049(7)°$ $R_p = 10.3\,\%$, $R_{wp} = 8.13\,\%$, $R_e = 0.745\,\%$ $R_B = 5.84\,\%$, $R_F = 5.88\,\%$					
Atom	Site	x	y	z	g	B_{iso}
Sr1/La1	2i	0.2512(19)	0.483(2)	0.494(2)	0.5/0.5	0.30(3)
Sr2/La2	2i	0.2522(17)	-0.019(2)	0.483(3)	0.5/0.5	0.30(3)
Sr3/La3	2i	0.2480(18)	0.484(2)	−0.018(3)	0.5/0.5	0.30(3)
Sr4/La4	2i	0.7495(18)	0.017(2)	0.009(2)	0.5/0.5	0.30(3)
Nb1	2i	0.005(2)	0.253(2)	0.755(2)	1	0.03(3)
Nb2	2i	0.499(2)	0.2618(16)	0.2581(16)	1	0.03(3)
Cu1	2i	0.005(2)	0.253(2)	0.253(3)	1	0.03(3)
Cu2	2i	0.504(3)	0.255(2)	0.750(3)	1	0.03(3)
O11	2i	0.042(2)	0.0103(19)	0.220(3)	1	0.57(2)
O12	2i	−0.047(2)	0.277(2)	−0.023(2)	1	0.57(2)
O13	2i	−0.033(2)	0.502(2)	0.287(3)	1	0.57(2)
O14	2i	0.041(2)	0.209(2)	0.514(2)	1	0.57(2)
O21	2i	0.248(3)	0.292(3)	0.221(3)	1	0.57(2)
O22	2i	0.252(3)	0.225(3)	0.798(3)	1	0.57(2)
O23	2i	0.254(3)	0.723(3)	0.297(4)	1	0.57(2)
O24	2i	0.250(3)	0.792(3)	0.723(3)	1	0.57(2)
O31	2i	0.466(3)	−0.002(3)	0.211(3)	1	0.57(2)
O32	2i	0.5230(17)	0.2810(18)	0.022(2)	1	0.57(2)
O33	2i	0.4491(16)	0.2044(18)	0.4739(17)	1	0.57(2)
O34	2i	0.534(3)	0.497(3)	0.285(3)	1	0.57(2)

Figures 3.6 (a) and (b) shows schematic crystal structures for SLCSO and SLCNO, respectively. It was confirmed from the present structural refinement that all the CuO_6 octahedra are elongated approximately along the c-axis owing to the Jahn–Teller effect in both compounds. The hole orbital $d(x^2-y^2)$, which gives the lowest orbital level of the Cu^{2+} ion, is spread in the ab-plane, as shown in Figs. 3.6 (c) and (d). Hence, the super-exchange interactions mediated via O^{2-} ions in the ab-plane must be much larger than those along the c-axis, which leads to the good two-dimensionality in SLCSO and SLCNO. The crystal structures of SLCSO and SLCNO have lower symmetry than those of Sr_2CuTeO_6 and Sr_2CuWO_6 due to the mismatch of ionic radii between Sr^{2+} and La^{3+}, which randomly occupy the A-site. However, the crystal lattices of SLCSO and SLCNO are nearly tetragonal, as shown in Tables 3.2 and 3.4; thus, the NN and NNN exchange interactions are expected to be approximately uniform in both compounds.

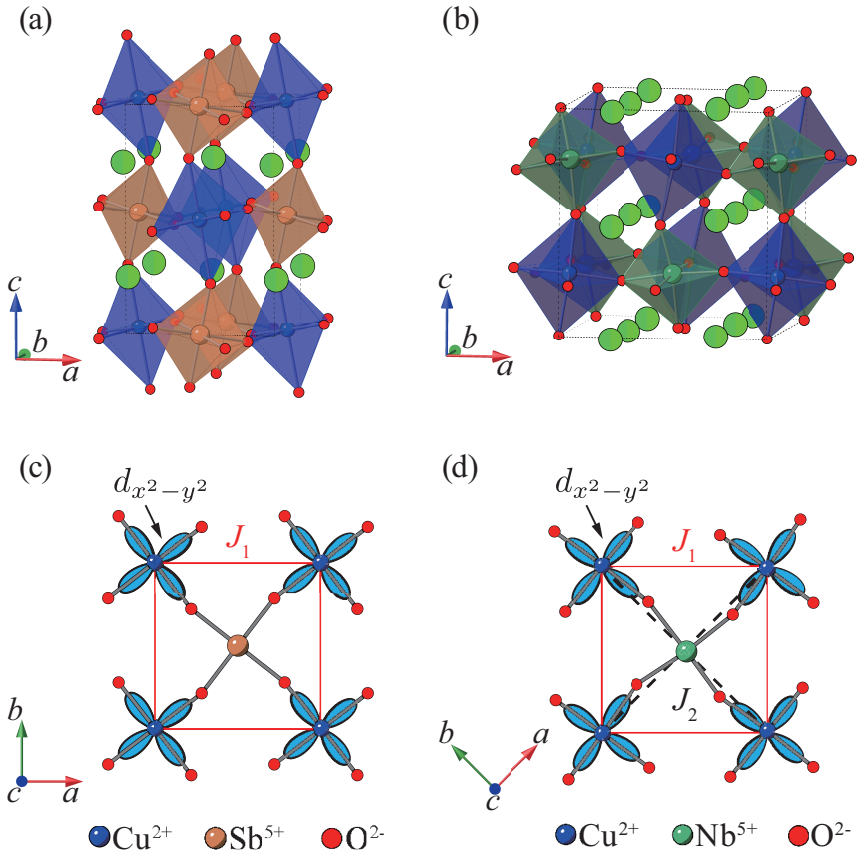

Figure 3.6: Schematic view of the crystal structures of (a) $SrLaCuSbO_6$ (SLCSO) and (b) $SrLaCuNbO_6$ (SLCNO) with the B-site ordered double perovskite structure. Blue, brown, and green indicate CuO_6, SbO_6, and NbO_6 octahedra, respectively. Green and red spheres are Sr/La and oxide ions, respectively. (c) and (d) show the linkages of CuO_6 and $Sb(Nb)O_6$ octahedra in the ab-plane of SLCSO and SLCNO, respectively. The hole orbitals $d(x^2-y^2)$ of Cu^{2+} ions are shown in blue. The uniform NN interactions J_1 and NNN interactions J_2 are illustrated by red solid and black dashed lines in (d), respectively.

3.2.2 Electron spin resonance

To estimate g-factors, ESR measurements using X-band microwave were performed on polycrystalline samples of SLCSO and SLCNO. Figures 3.7 (a) and (b) show the field derivative of the ESR absorption intensity dI/dH for SLCSO and SLCNO, respectively, measured at room temperature. The microwave frequency is fixed at $\nu = 9.44079\,\mathrm{GHz}$ for SLCSO and $\nu = 9.439860\,\mathrm{GHz}$ for SLCNO, respectively, and the magnetic field was swept from 0.2 T to 0.4 T. The shape of the ESR spectrum of SLCSO is typical of the powder averaged spectrum for Cu^{2+} ions. In an elongated octahedral environment, Cu^{2+} ion has two principal values of the g-factors $g_{\parallel}$ and $g_{\perp}$ for magnetic fields parallel and perpendicular to the elongated axis, respectively. Fitting a superposition of field derivatives of two pseudo-Voigt functions to the ESR spectrum for SLCSO, $g_{\parallel} = 2.437$ and $g_{\perp} = 2.076$ were obtained for SLCSO. The blue solid line in Fig. 3.7 (a) indicates the fit. These g-factors are typical for copper (II) oxides with elongated CuO_6 octahedra.

The ESR spectrum of SLCNO is symmetric, but its linewidth is much broader than that of SLCSO. It is inferred that line broadening arises due to the additional magnetic anisotropy, such as the antisymmetric exchange interaction of the Dzyaloshinskii–Moriya type, which arises from the low symmetry of the crystal lattice. $g_{\parallel} = 2.259$ and $g_{\perp} = 2.100$ were evaluated from the same analysis as that applied to the ESR spectrum of SLCSO. Note that the ESR spectrum of SLCNO is not well reproduced by the fit with a single component of the derivative pseudo-Voigt function.

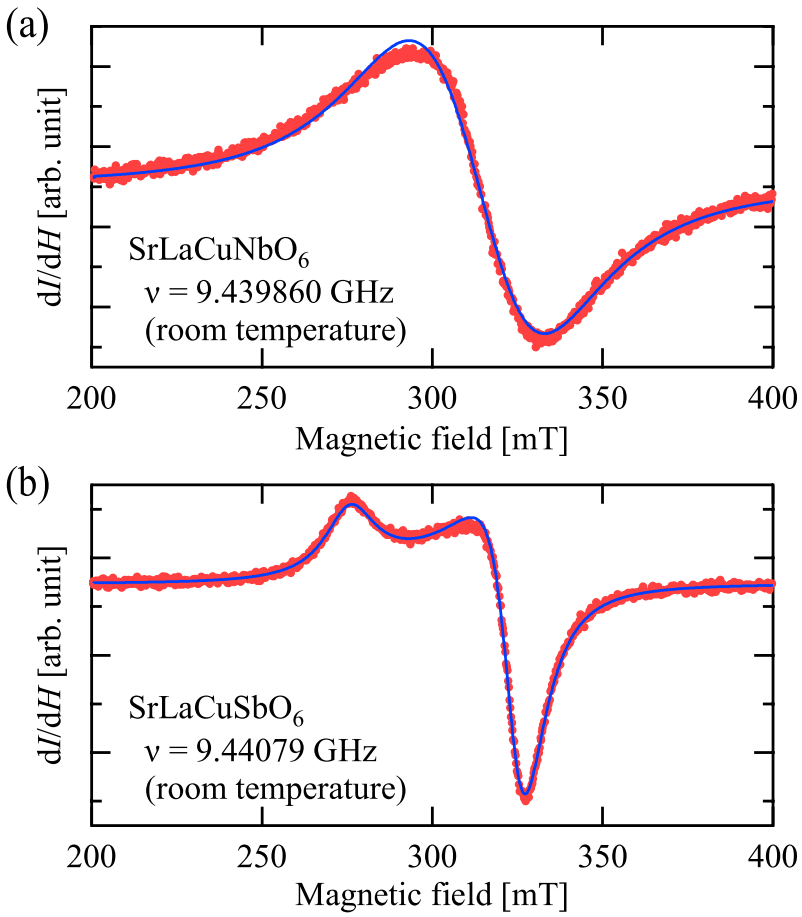

Figure 3.7: Field derivative of the ESR absorption intensity $\mathrm{d}I/\mathrm{d}H$ for (a) SLCSO and (b) SLCNO. Blue solid lines are fits using two pseudo-Voigt functions with the anisotropic g-factors given in the text.

3.2.3 Magnetic susceptibility and magnetization

The temperature variation of the magnetic susceptibilities of SLCSO and SLCNO measured at $\mu_0 H = 0.1\,\mathrm{T}$ is shown in Fig. 3.8 (a). With decreasing temperature, the magnetic susceptibility $\chi(T)$ displays a broad maximum at $T_{\max} = 71\,\mathrm{K}$ for SLCSO and at $T_{\max} = 44\,\mathrm{K}$ for SLCNO. The broad maximum is attributable to the development of magnetic short-range correlations, which is characteristic of two-dimensional SLHAFs [116–118]. Below $T_{\max}$, small hump anomalies indicative of magnetic ordering are observed at $T_{\mathrm{N}} = 13.6\,\mathrm{K}$ for SLCSO and at $T_{\mathrm{N}} = 15.7\,\mathrm{K}$ for SLCNO. These anomalies were also observed in $\mathrm{d}(\chi T)/\mathrm{d}T$ corresponding to the right-hand axis in Fig. 3.8 (b) Above 150 K, the magnetic susceptibilities of both compounds are described by the Curie–Weiss law $\chi = C/(T - \Theta)$ with $C \simeq 0.51\,\mathrm{emu\,K\,mol^{-1}}$ and $\Theta \simeq -120\,\mathrm{K}$ for SLCSO, and $C \simeq 0.47\,\mathrm{emu\,K\,mol^{-1}}$ and $\Theta \simeq -77\,\mathrm{K}$ for SLCNO. The large Weiss constants Θ indicate that the dominant exchange interaction is antiferromagnetic and large. The magnitude of the estimated Curie constant of SLCSO is larger than that of SLCNO, suggesting that the g-value of SLCSO is larger than that of SLCNO. This is consistent with the results obtained by ESR measurements.

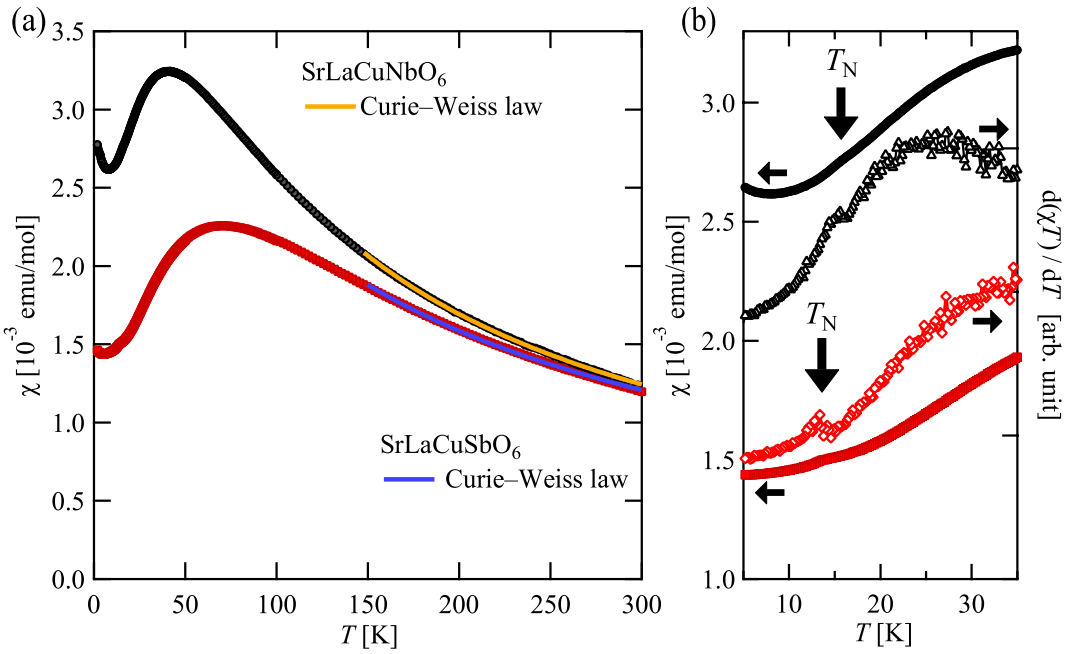

Figure 3.8: (a) Temperature dependence of magnetic susceptibilities χ of SLCSO (red squares) and SLCNO (black circles) measured at $\mu_0 H = 0.1\,\mathrm{T}$. The solid lines are the best fits of Curie–Weiss fitting, described in the main text. (b) An enlargement of the magnetic susceptibilities of SLCSO and SLCNO between 5 and 35 K. The red and black open symbols represent $\frac{\mathrm{d}(\chi T)}{\mathrm{d}T}$ for SLCSO and SLCNO. Downward arrows indicate small kinks suggestive of magnetic phase transitions at $T_\mathrm{N} = 13.6\,\mathrm{K}$ for SLCSO and at $T_\mathrm{N} = 15.7\,\mathrm{K}$ for SLCNO.

Figure 3.9 shows the magnetization process $M(H)$ and its field derivative $\mathrm{d}M/\mathrm{d}H$ for SLCSO and SLCNO at 1.8 K. A small cusp anomaly of $\mathrm{d}M/\mathrm{d}H$ is observed around 1.4 T for SLCSO, which indicates a spin-flop transition. Since ordered spins lie in the *ab*-plane as shown in Sec. 3.2.6, the spin-flop transition is caused by easy-axis anisotropy in the *ab*-plane. The spin-flop transition was not detected in SLCNO powder, which suggests that the in-plane anisotropy is negligible in SLCNO.

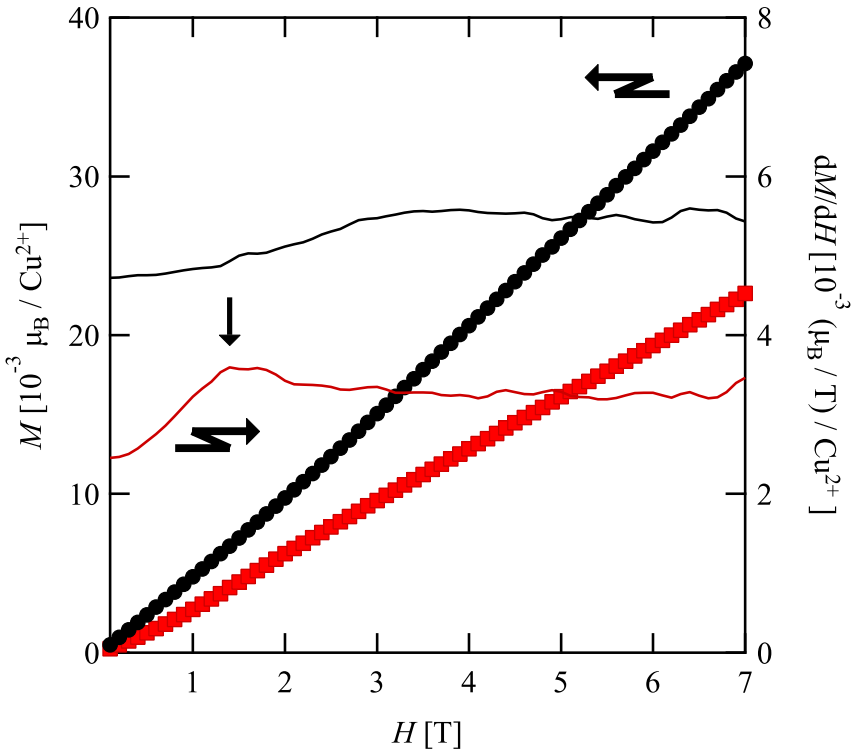

Figure 3.9: Magnetization curves of SLCSO and SLCNO measured at 1.8 K. The solid curves show the field derivatives $\mathrm{d}M/\mathrm{d}H$. The downward arrow indicates a small bend anomaly in the $\mathrm{d}M/\mathrm{d}H$ data of SLCNO, which is suggestive of a spin-flop transition.

3.2.4 Specific heat

Figure 3.10 shows the temperature dependence of the total specific heat divided by temperature C/T in SLCSO, SLCNO, and nonmagnetic $SrLaZnSbO_6$ measured at zero magnetic field. No anomaly indicative of a structural phase transition was observed down to 1.8 K in these three compounds. The magnetic contribution of the specific heat $C_{\rm mag}$ was extracted by subtracting the lattice contribution from the raw data. The lattice contribution was evaluated using the nonmagnetic counterpart $SrLaZnSbO_6$, which has a similar crystal structure to SLCSO and SLCNO. Figures 3.11 (a) and (b) show the temperature dependence of $C_{\rm mag}$ at zero magnetic field.

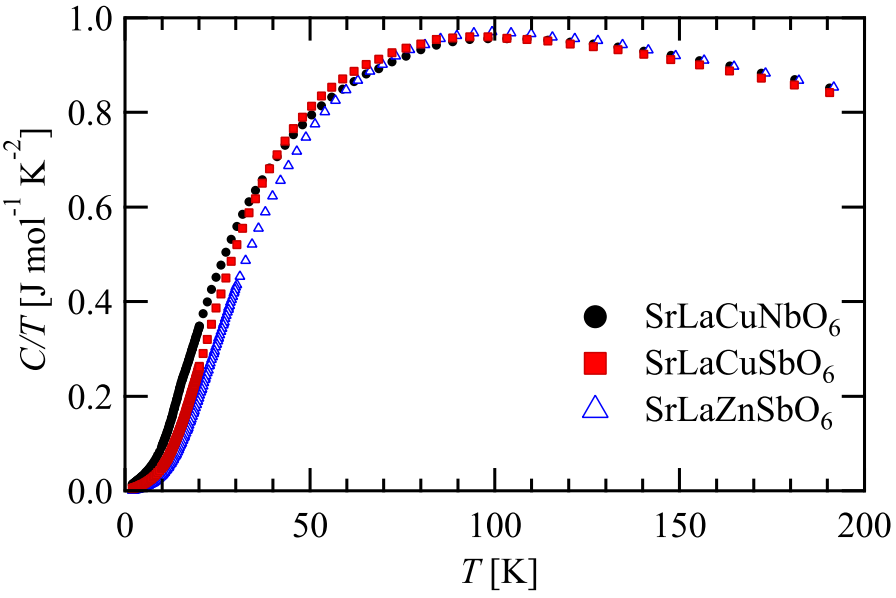

Figure 3.10: Temperature dependence of total specific heat divided by temperature C/T in SLCSO, SLCNO, and nonmagnetic $SrLaZnSbO_6$ powders measured at zero magnetic field.

The magnetic entropy $S_{\rm mag}(T)$ was obtained by integrating $C_{\rm mag}/T$ over the interval 1.8 K to T as the following formula;

$$S_{\rm mag}(T) = \int_{1.8{\rm K}}^{T} \frac{C_{\rm mag}(T)}{T} dT. \tag{3.2}$$

The obtained $S_{\rm mag}(T)$ is shown on the right vertical axis of Figs. 3.11 (a) and (b). The magnetic entropies at 100 K are $S_{\rm mag} \simeq 0.89R\ln 2$ and $0.94R\ln 2$ for SLCSO and SLCNO, respectively, which are consistent with the theoretically expected value of $R\ln 2$ for the $S = \frac{1}{2}$ systems.

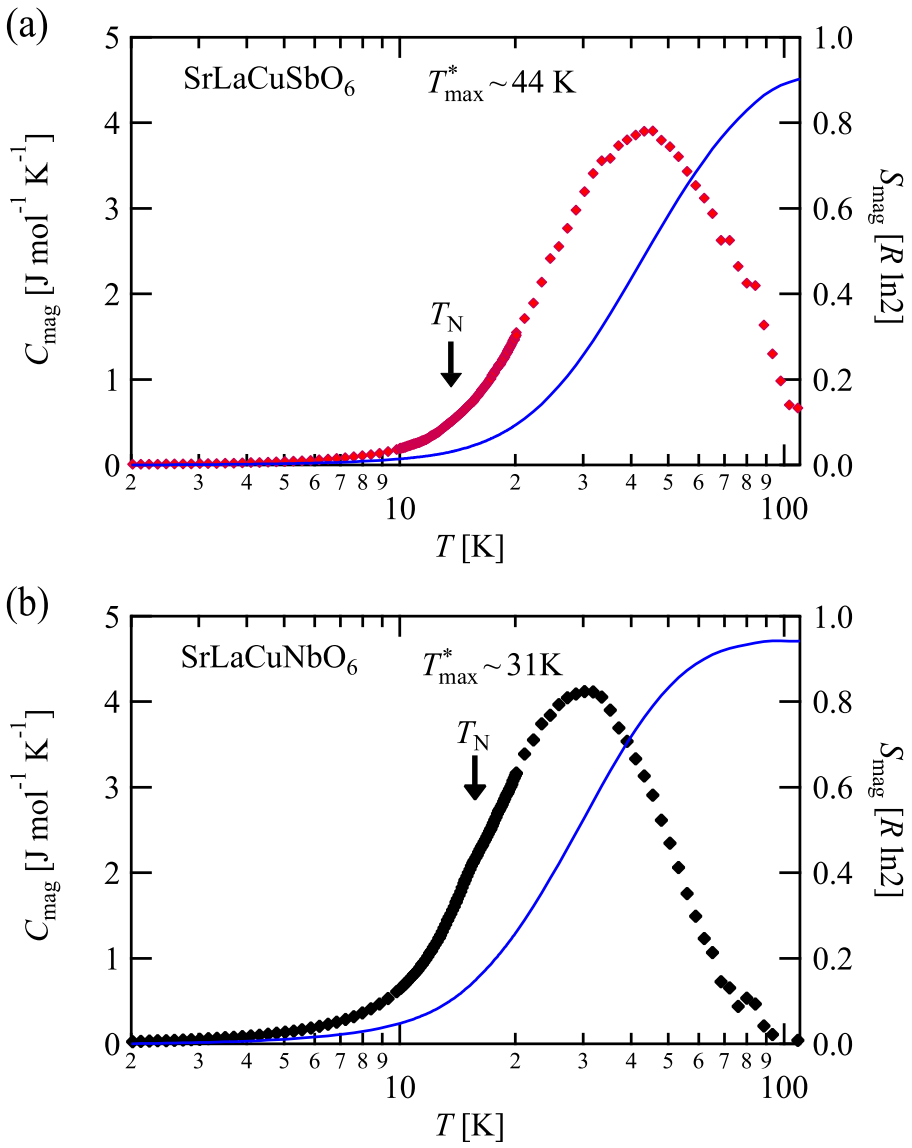

Figure 3.11: Temperature dependence of C_{mag} for (a) SLCSO and (b) SLCNO at zero magnetic field. Solid curves represent the magnetic entropy S_{mag}. Vertical arrows indicate ordering temperatures T_{N} determined from the magnetic susceptibility data.

Small kinks were observed in C_{mag} at temperatures very close to the ordering temperatures T_{N} determined from the magnetic susceptibility data for both compounds, indicative of the magnetic ordering, as shown in Figs. 3.11 (a) and (b). These anomalies were feeble since most of the magnetic entropy was released by the development of short-range correlations above T_{N}. The residual entropy at T_{N} is $S(T_{\mathrm{N}}) \simeq 0.03R\ln 2$ and $0.11R\ln 2$ for SLCSO and SLCNO, respectively, which is considerably decreased. A similar behavior of specific heat was also found in other $S = \frac{1}{2}$ $J_1 - J_2$ SLHAFs Sr_2CuMO_6 (M = Te and

W) [119].

Magnetic specific heat $C_{\rm mag}$ exhibits a rounded maximum at $T^*_{\rm max} = 44\,{\rm K}$ for SLCSO and $T^*_{\rm max} = 31\,{\rm K}$ for SLCNO owing to the short range spin correlation, as shown in Fig. 3.11 (a). This is consistent with a rounded maximum observed in the temperature dependence of magnetic susceptibility. Particularly in SLCSO, the value of the $C_{\rm mag}$ at $T^*_{\rm max}$ is $C^{\rm max}_{\rm mag} = 0.47\,R$, which coincides with that for an $S = 1/2$ SLHAF with the NN interaction [120] although SLCSO has a monoclinic structure.

3.2.5 μSR measurements

A magnetic phase transition was observed as a hump anomaly in the temperature dependence of magnetic susceptibility and specific heat. However, it is premature to conclude from these bulk measurements alone whether the entire sample is in a magnetically ordered state. Highly sensitive local probe measurements are necessary to reveal the magnetic state. Therefore, I carried out μSR measurements, which can detect a magnetic phase separation and internal magnetic fields in materials with ultra-high sensitivity. μSR measurements were conducted in a zero field (ZF), longitudinal field (LF), and weak transverse field (TF) mode (2 mT) using the ARTEMIS spectrometer with a conventional ^{4}He flow cryostat installed at the Material and Life Science Facility (MLF), J-PARC. The temperature range is from 3.5 K to 300 K, and the applied LF is up to 300 mT. The muon source at MLF is a pulsed muon source. The μSR experiment using a pulsed muon source has a lower time resolution than using a continuous muon source, but it is possible to measure muon relaxation over a long time scale up to 15μs. All of the μSR data were analyzed using the musrfit software package [121].

TF-μSR

Figures 3.12 and 3.13 show the μSR time spectra of SLCSO and SLCNO measured by applying a 2 mT transverse field. Rotational signal with $\nu = \gamma_\mu \mu_0 H_{\rm TF}/2\pi \sim$ 0.27 MHz corresponding to 2 mT was found. $\gamma_\mu = 2\pi \times 135.5\,{\rm MHz/T}$ is the gyromagnetic ratio for muons. The initial total asymmetry $A_{\rm tot}$ was determined by fitting the data measured at 300 K for SLCSO and 100 K for SLCNO, which is sufficiently higher than $T_{\rm N}$, with the following function

$$A(t) = A_{\rm tot} \exp\left(-(\lambda t)^\beta\right) \cos(2\pi\nu t + \phi) \tag{3.3}$$

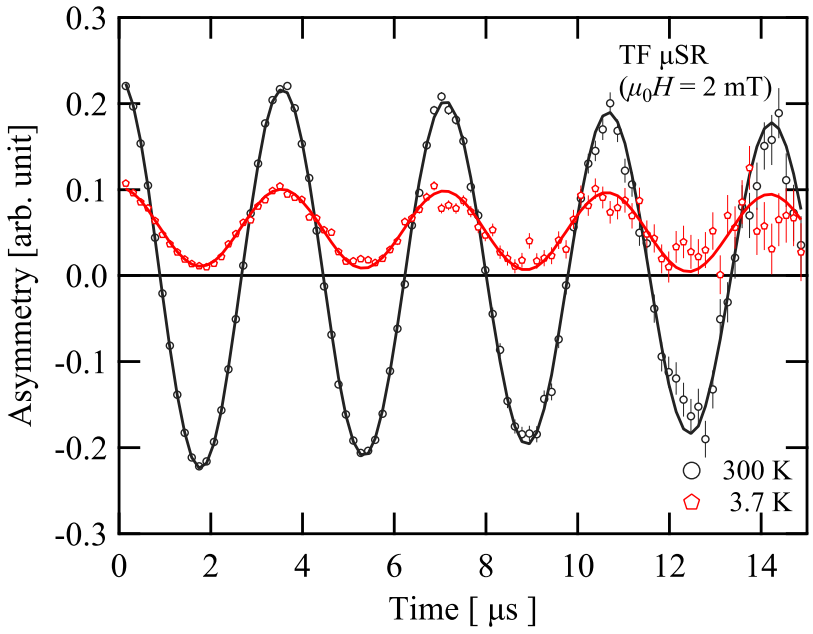

Figure 3.12: μSR spectra of SLCSO measured with a 2 mT transverse field at 300 K and 3.7 K. Black and red solid curves are results of fitting by Eq. 3.3 and Eq. 3.4, respectively.

Rotational signals with an upward shift were found in the TF-μSR spectra collected at 3.7 K as shown in Figs. 3.12 and 3.13. These spectra are typical for the presence of magnetic order. Since the internal magnetic field is much larger than the applied field in the magnetically ordered state, the precessional motion of the muon spin is mainly dependent on the internal magnetic field. μSR measurement using a pulsed muon beam cannot capture the fast rotation due to the lack of time resolution. Therefore, the 2/3 component of $A_{\rm tot}$ corresponding to the rapid rotation signal due to the internal magnetic field was lost, while the residual 1/3 of $A_{\rm tot}$ was observed as the upward shift. It is noted that the shift in the center of rotation is slightly relaxed, which suggests that some of the spins could fluctuate due to magnetic frustration.

The observed rotational component at 3.7 K is originated from the muon implanted in the silver sample holder. Since silver has a very small nuclear moment, the muon implanted in the silver is affected only by the applied transverse field. Hence, the background $A_{\rm BG}$ was estimated by evaluating the fraction of the rotational component. As shown in Figures 3.12 and 3.13, the TF spectrum at the lowest temperature was reproduced by the equation 3.4.

$$A(t) = A_{\rm BG}\cos(\omega t + \phi) + A_{\rm c}\exp(-\lambda t) \tag{3.4}$$

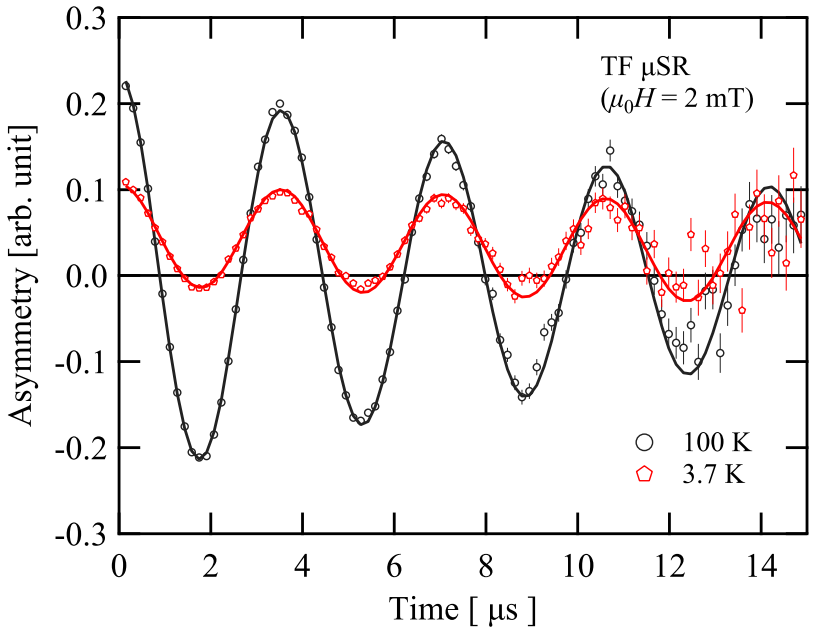

Figure 3.13: μSR of SLCNO measured with a 2 mT transverse-field at 100 K and 3.7 K. Black and red solid curves are results of fitting by Eq. 3.3 and Eq. 3.4, respectively.

$A_{\mathrm{BG}}/A_{\mathrm{tot}} = 0.20$ and 0.25 were obtained for SLCSO and SLCNO, respectively. These value are consistent with other experiments [122, 123]. The shift of the center of rotation was estimated as $A_{\mathrm{c}}/(A_{\mathrm{tot}} - A_{\mathrm{BG}}) = 0.31$ and 0.27 for SLCSO and SLCNO, respectively. These value are slightly smaller than "1/3" expected for the case of the whole sample being in a magnetically ordered state. This implies that some of the spins still fluctuate without magnetic ordering at 3.7K. Note that this upward shift of the asymmetry should be zero, if dynamic fluctuations are still retained, as in the quantum disordered ground state [119, 124].

ZF-μSR

Figures 3.14 and 3.15 show representative spectra measured in a zero magnetic field for SLCSO and SLCNO, respectively. The temperature range is from 3.9 K to 296 K for SLCSO and from 3.5 K to 296 K for SLCNO. In both compounds, the relaxation curve evolved from Gaussian to Lorentzian with decreasing temperatures. In the high-temperature region, the contribution from the nuclear magnetic moment is dominant, which produces the Gaussian relaxation. On the other hand, in the low-temperature region, the magnetically ordered state develops, and the contribution of electron spins becomes dominant. Therefore, the shape of the μSR spectrum changed with decreasing temperature. Remarkably, the initial asymmetry $A(0)$ decreased with decreasing temperature. In general, for the magnetically ordered state, an oscillating signal should be observed in the ZF μSR spectrum because the existence of magnetic order causes muon spin rotation due to the internal magnetic field. There are two possible explanations for the loss of initial asymmetry without an oscillation signal. One is that the asymmetry corresponding to the rotational component disappears due to the fast undetectable precession caused by the strong static internal field. The other is that a wide distribution of internal fields around the non-zero mean value causes fast damping, and the asymmetry corresponding to the fast damping component is lost. This damping is independent of whether the internal fields are static or dynamic. Thus LF-μSR measurements are necessary to clarify the nature of the magnetic state.

All the spectra were reasonably fitted by a phenomenological stretched exponential decay, which is described by

$$A(t) = A^{\mathrm{ZF}} \exp((-\lambda^{\mathrm{ZF}} t)^{\beta}) + A_{\mathrm{BG}}, \tag{3.5}$$

where A^{ZF} is asymmetry of the relaxing component, λ^{ZF} is the depolarization rate of muon spin, and A_{BG} is the background asymmetry estimated from the TF μSR measurement. β is a lineshape parameter.

$\lambda(T)$ obtained by fitting the ZF μSR data is shown in Fig. 3.16 for SLCSO and Fig. 3.17 for SLCNO. Below T_{N}, $\lambda(T)$ is steeply suppressed and A^{ZF} decreases toward a constant value with decreasing temperatures as represented in Fig. 3.18 for SLCSO and Fig. 3.19 for SLCNO. This behavior of $A^{\mathrm{ZF}}(T)$ is indicative of a static internal field originating from magnetic ordering. If the spontaneous magnetization in a polycrystalline sample is oriented in a random direction, the 1/3 component parallel to the muon spin polarization exhibits

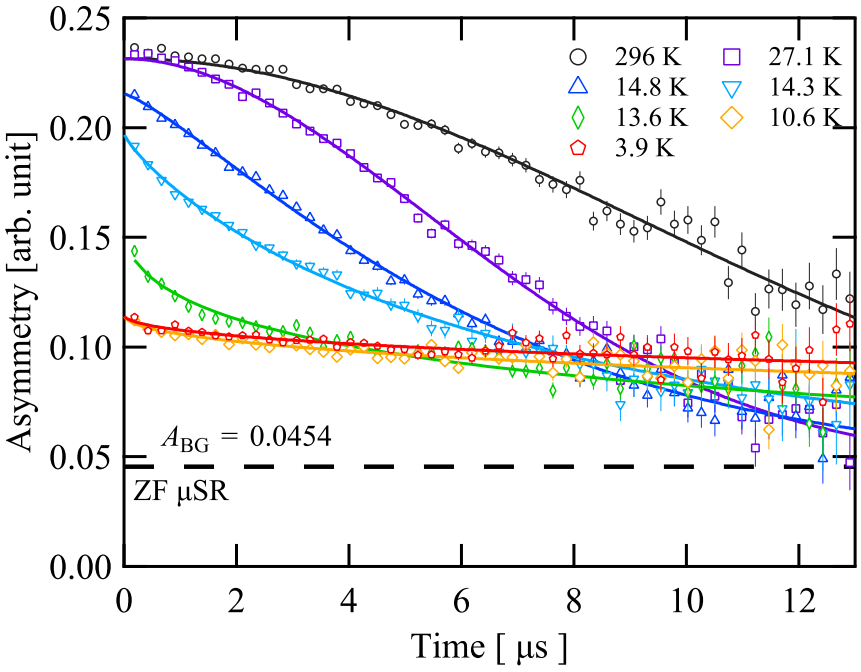

Figure 3.14: ZF μSR spectra of SLCSO measured at various temperatures. Solid curves are results of fitting by Eq. 3.5.

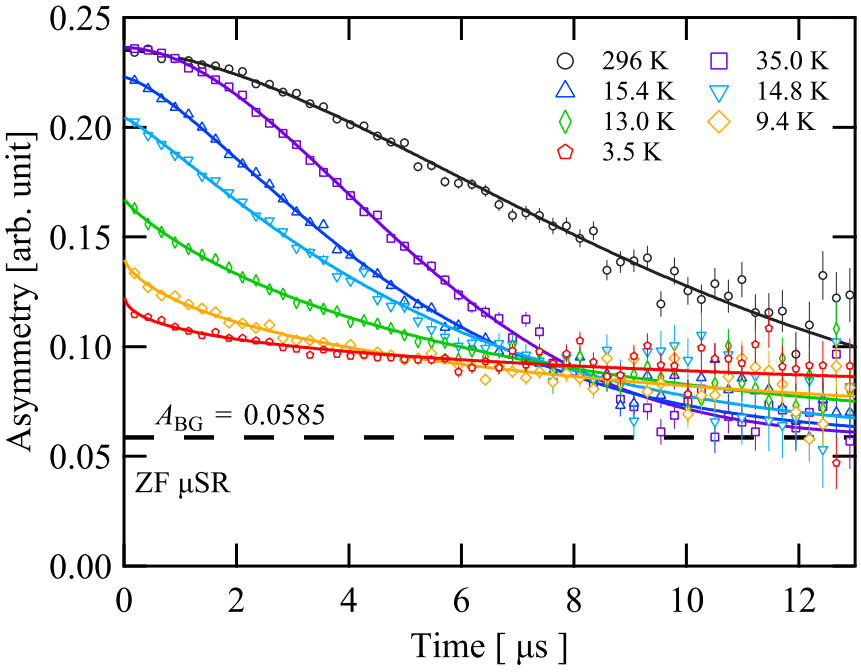

Figure 3.15: ZF μSR spectra of SLCNO measured at various temperatures. Solid curves are results of fitting by Eq. 3.5.

spin-lattice relaxation, and the 2/3 component perpendicular to the muon spin polarization exhibits precession. The $A^{\mathrm{ZF}}(T \to 0)/A_{\mathrm{sample}} \sim 1/3$ indicates that almost all portions of the sample are in a magnetically ordered state, and a static internal magnetic field emerges.

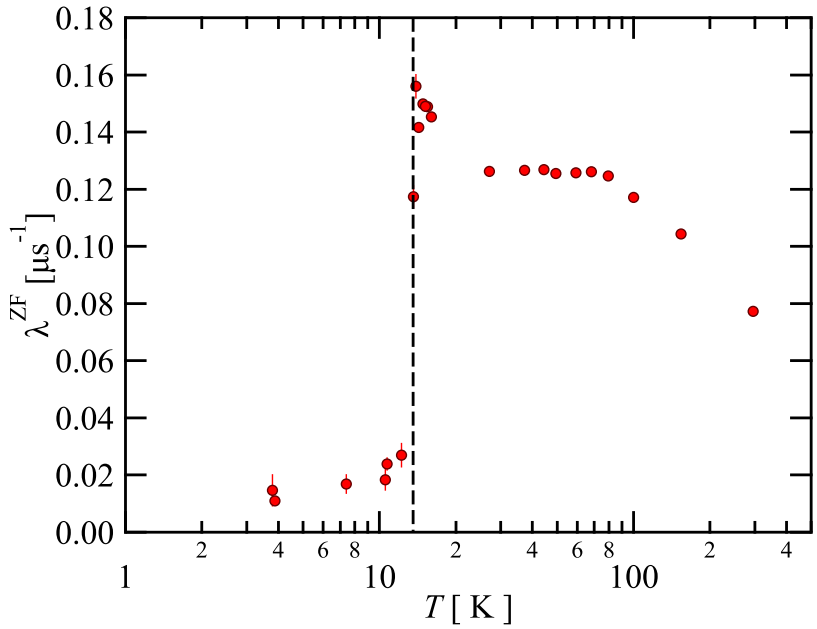

Figure 3.16: Temperature dependence of spin relaxation rate of SLCSO obtained obtained by fitting the ZF μSR data.

Figures 3.20 and 3.21 show a temperature dependence of a line shape parameter $\beta(T)$. In the high-temperature region, muon spin relaxation due to random static internal fields caused by the nuclear magnetic moments is dominant, which gives the Gaussian shape ($\beta = 2$). With decreasing temperatures, magnetic correlation in the electron spins developed and affected the μSR spectral shape. Particularly below T_{N}, $\beta(T)$ rapidly decreased and converged to values below 1 for both compounds. This result could be due to the emergence of a wide distribution of the relaxation rate. The stretched exponential function is derived by integrating a continuous distribution of relaxation times as follows [125];

$$A^{\mathrm{ZF}} \exp((-\lambda^{\mathrm{ZF}} t)^{\beta}) = A^{\mathrm{ZF}} \int_0^{\infty} \rho(\tau) \exp(-t/\tau) d\tau, \tag{3.6}$$

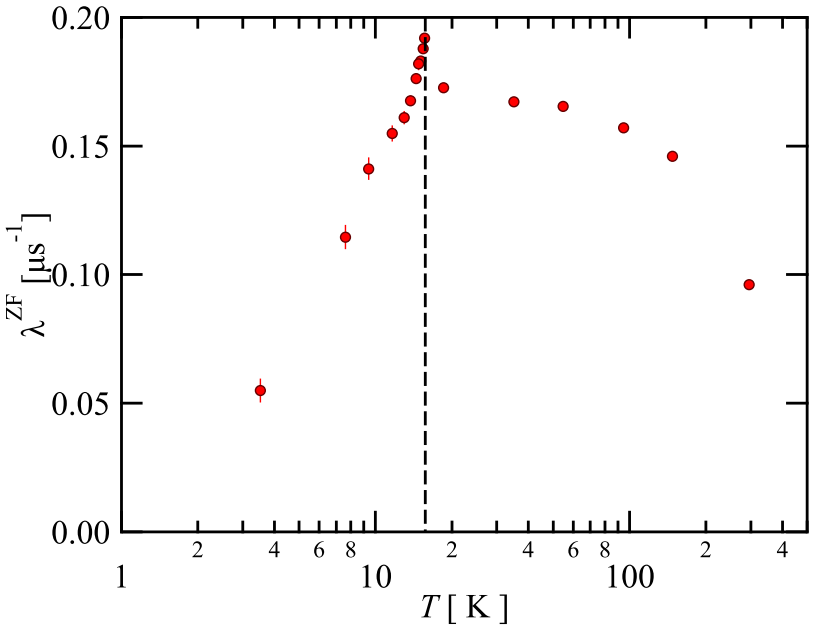

Figure 3.17: Temperature dependence of spin relaxation rate of SLCNO obtained obtained by fitting the ZF μSR data.

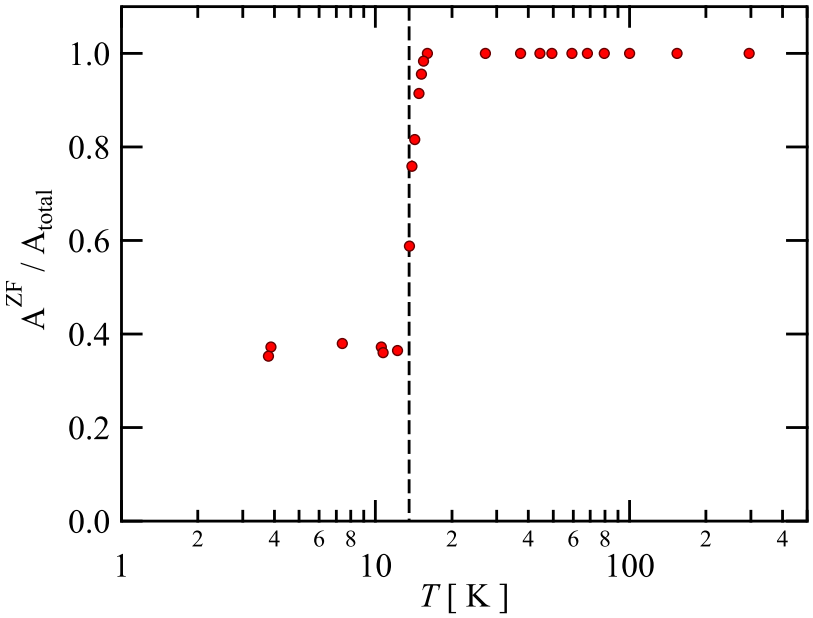

Figure 3.18: A fraction of asymmetry of the relaxation component as a function of temperature for SLCSO.

where $\rho(\tau)$ is given by [126]

$$\pi\tau\rho(\tau) = -\sum_{l=1}^{\infty} \frac{(-1)^l \Gamma(1+l_\kappa)}{l!} \left(\tau\lambda^{\mathrm{ZF}}\right) \sin(\pi\kappa l). \tag{3.7}$$

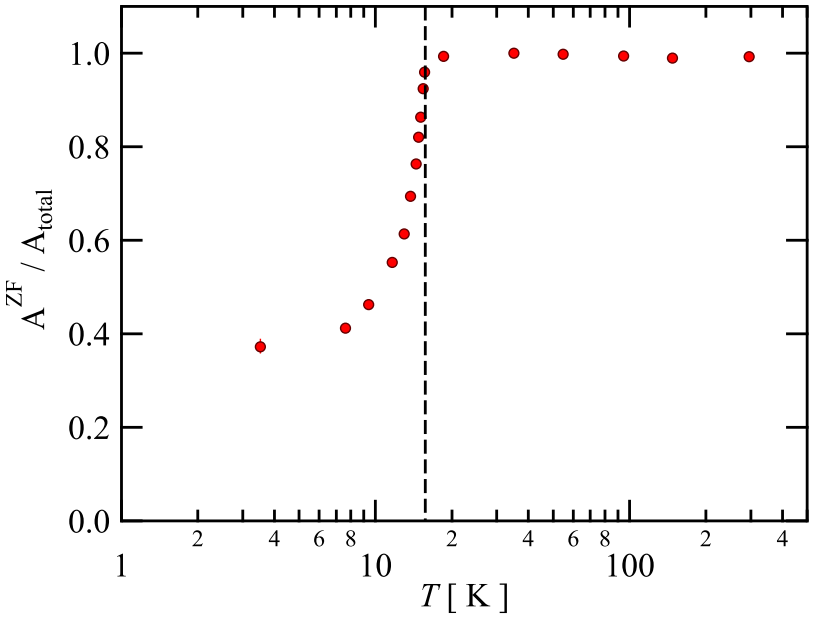

Figure 3.19: A fraction of asymmetry of the relaxation component as a function of temperature for SLCNO.

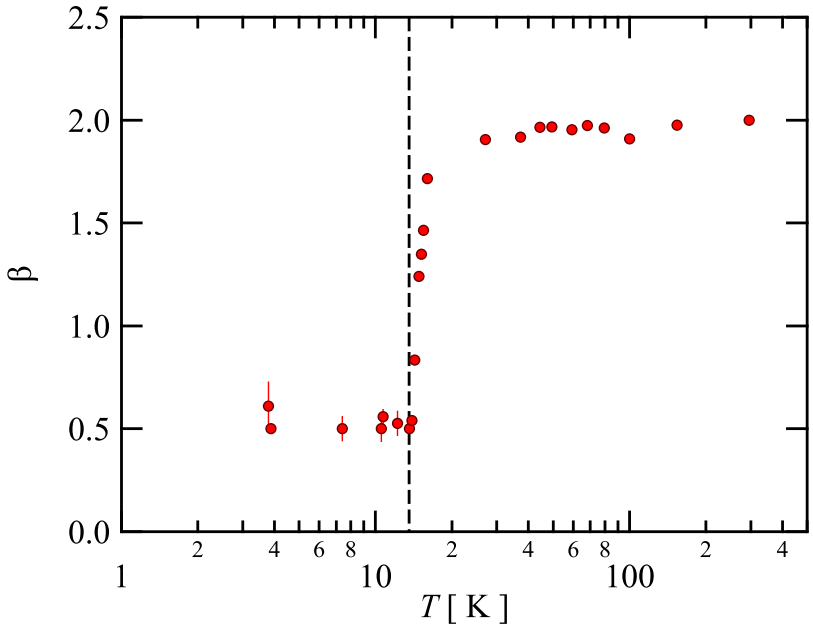

Figure 3.20: Shape factor β as a function of temperature for SLCSO.

Figure 3.22 shows distributions of the relaxation time computed by the series expansion method reported in [125]. The smaller value of β than unity implies that there is a wide distribution in the relaxation time. In SLCSO and SLCNO,

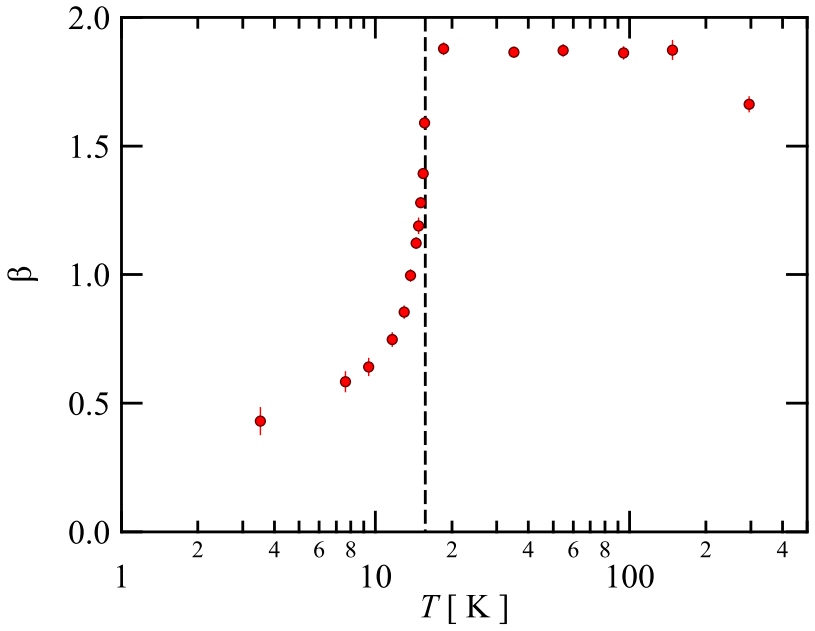

Figure 3.21: Shape factor β as a function of temperature for SLCNO.

the site disorder of Sr^{2+} and La^{3+} ions disturbs the local crystal structure leading to bond randomness. The bond randomness could make the ordered magnetization inhomogeneous, giving rise to a distribution in the relaxation time.

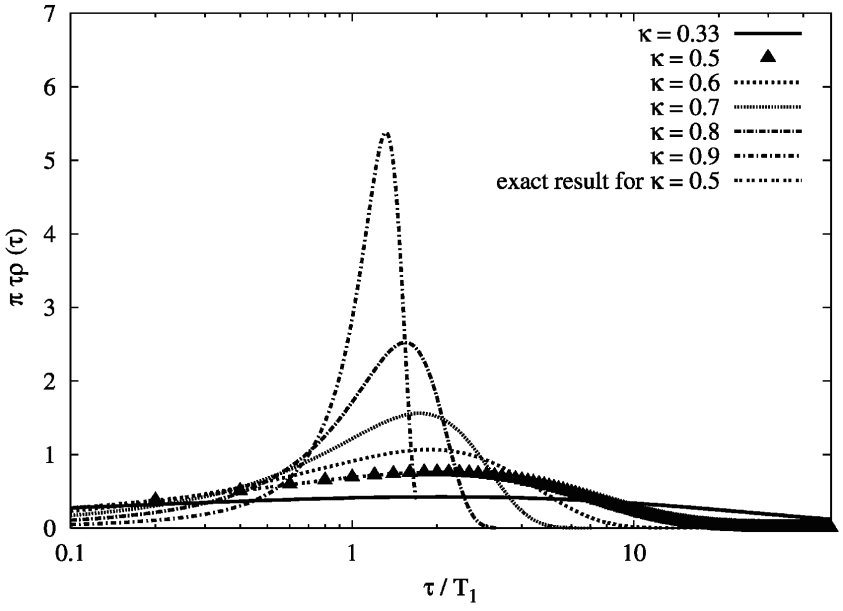

Figure 3.22: Computed relaxation rate distribution for various values of the stretched exponential exponent κ, reprinted from Ref. [125]

LF-μSR

To clarify whether the internal magnetic field is dynamic or static, LF μSR measurements were performed. Figures 3.23 and 3.24 show the LF μSR spectra measured at $T = 3.8\,\mathrm{K}$ in an applied field of $\mu_0 H = 0 - 300\,\mathrm{mT}$. The μSR data are successfully described by the following stretched exponential function as well as the ZF μSR;

$$A(t) = A^{\mathrm{LF}} \exp((-\lambda^{\mathrm{LF}} t)^{\beta}) + A_{\mathrm{BG}}, \tag{3.8}$$

where β and A_{BG} were estimated by ZF and TF μSR experiments, respectively. With increasing the applying longitudinal fields, the relaxation spectrum shifted upward. This is typical behavior of muon spin decoupling from a "static" internal field. Note that in the presence of a dynamic internal field, no upward shift of the spectrum occurs, but only a decrease in the relaxation rate should be observed.

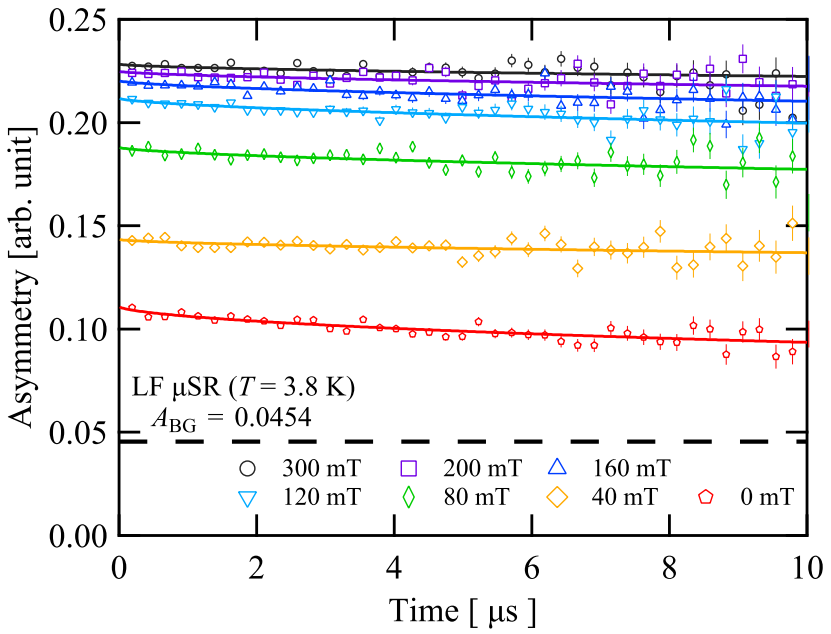

Figure 3.23: LF μSR spectra of SLCSO measured at 3.8 K. Solid curves are results of fitting by Eq. 3.8

Figures 3.25 and 3.26 show an applied field dependence of a fraction $A_{\mathrm{LF}}/A_{\mathrm{sample}}$ for SLCSO and SLCNO, respectively, where $A_{\mathrm{sample}} \equiv A_{\mathrm{tot}} - A_{\mathrm{BG}}$. The magnitude of the internal static field is equal to that of the applied longitudinal field at $A_{\mathrm{LF}}/A_{\mathrm{sample}} = 0.5$ [75]. The magnitude of the internal magnetic field at the

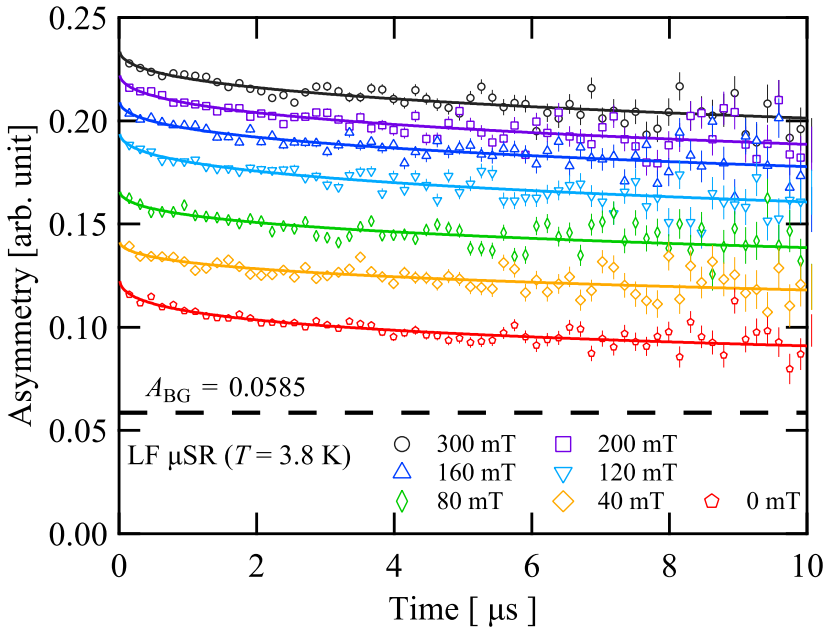

Figure 3.24: LF μSR spectra of SLCNO measured at 3.8 K. Solid curves are results of fitting by Eq. 3.8

muon stop site was estimated to be 35 mT for SLCSO and 45 mT for SLCNO. If there is a uniform internal magnetic field of 35 mT in the samples, the corresponding muon rotational frequency is 4.7 MHz. Since this is almost the upper limit of detection ($\sim$ 5 MHz), the rotation signal could not be detected by the ZF μSR measurement. In the present measurements using pulse muon beams, there is an uncertainty of the time in the start time of the muon rotation due to the width of the pulse. The muon beam width in this experiment is $\delta \sim 100$ ns [76]. The corresponding Nyquist frequency is $f_N = 1/2\delta \sim 5$ MHz, which is the upper limit of the detectable rotation frequency.

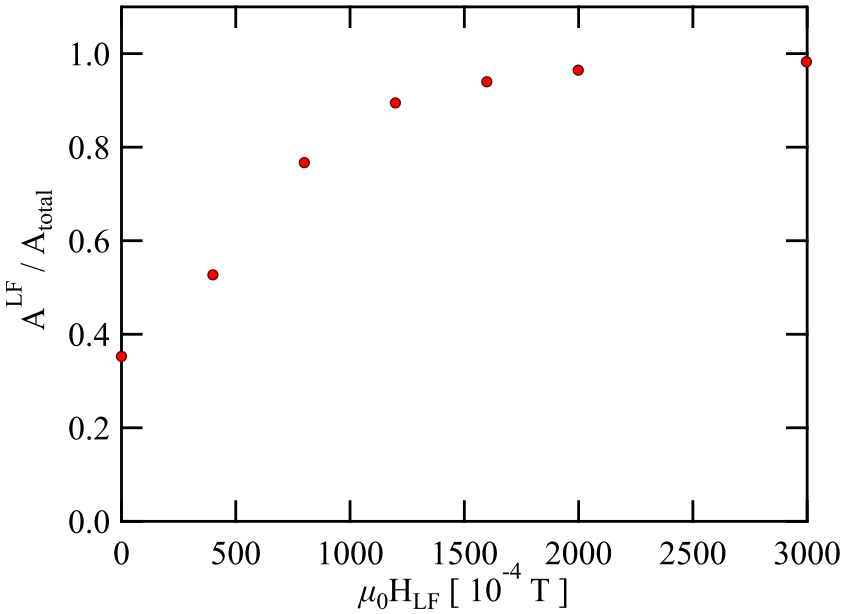

Figure 3.25: A fraction of asymmetry of the relaxation component in longitudinal fields as a function of applied fields for SLCSO.

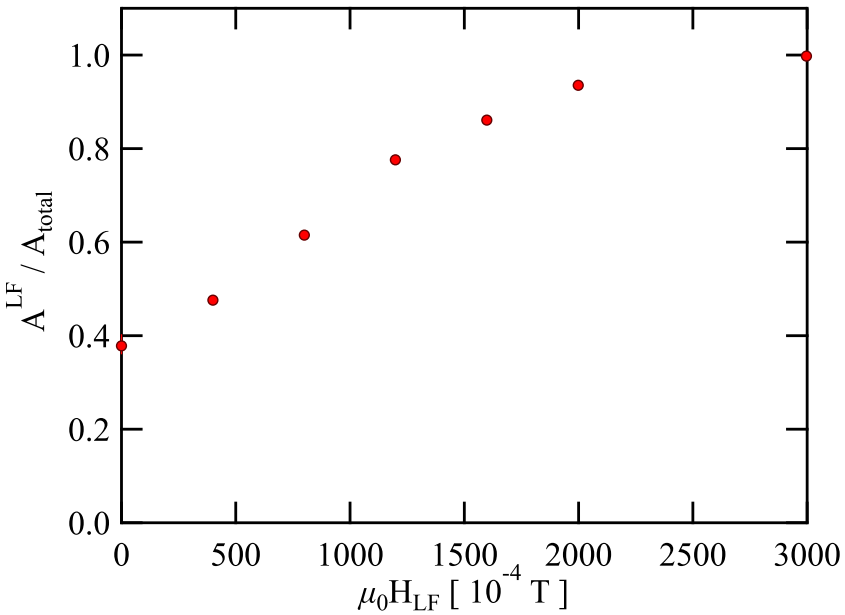

Figure 3.26: A fraction of asymmetry of the relaxation component in longitudinal fields as a function of applied fields for SLCNO.

3.2.6 Magnetic structure

To investigate magnetic structures of SLCSO and SLCNO below T_N, neutron powder diffraction (NPD) measurements were performed at 2.6 K using the SuperHRPD(BL08) time-of-flight diffractometer installed at the Material and Life Science Facility (MLF) at J-PARC, Japan [70, 71]. Irreducible representation analyses for SLCSO and SLCNO were conducted by using the SARAh program [127]. The magnetic structures of SLCSO and SLCNO were refined using the NPD profiles obtained from the 90 degrees (QA) bank and low-angle (LA) bank by Rietveld analysis with the Fullprof program [113].

$SrLaCuSbO_6$

Figure 3.27 shows neutron powder diffraction (NPD) spectra of SLCSO collected from the LA and QA banks at 3.5 K, where the diffraction spectrum at 20 K ($> T_N = 13.6$ K) has been subtracted, so that only magnetic Bragg peaks are extracted. All the magnetic peaks can be indexed by the propagation vector $\boldsymbol{k} = (1/2, 1/2, 0)$ on the body-centered structure. Therefore, the magnetic structure in the two-dimensional (2D) layer of SLCSO is determined to be NAF, as observed in Sr_2CuTeO_6 [103]. The absence of superlattice magnetic reflection for the doubling of the lattice constant c is consistent with good two-dimensionality.

To determine the magnetic structure in the ordered state of SLCSO, we performed the irreducible representation analysis using the SARAh program [127] for the space group $P2_1/n$ with $\boldsymbol{k} = (1/2, 1/2, 0)$. In SLCSO, Cu occupies the Wyckoff $2c$ position, which has two identical sites of $(x, y, z) = (1/2, 0, 1/2)$ and $(0, 1/2, 0)$. Because the decomposition of the magnetic representation of the Cu site is expressed as $\Gamma_{\rm mag} = 3\Gamma_2^1 + 3\Gamma_4^1$ in Kovalev's notation, there are two possible models corresponding to Γ_2 and Γ_4, as shown in Fig. 3.28. In the Γ_2 model, if one sublattice magnetic moment is expressed as (m_x, m_y, m_z), where the x-, y-, and z-axes are chosen to be parallel to the lattice vectors $\boldsymbol{a}$, $\boldsymbol{b}$, and $\boldsymbol{c}$, respectively, the other is expressed as $(m_x, -m_y, m_z)$. On the other hand, in the Γ_4 model, if one sublattice magnetic moment is expressed by the basis vector (m_x, m_y, m_z), the other is defined by $(-m_x, m_y, -m_z)$. However, from "powder-averaged" neutron diffraction data, it is difficult to distinguish the Γ_2 and Γ_4 models. Thus, to estimate the size of the magnetic moment m, we examined the three Γ_2-based magnetic models, in which the magnetic moments are aligned parallel to the a-, b-, and c-axes. As shown in Fig. 3.27, the Rietveld analysis of the magnetic structure reveals that the experimental

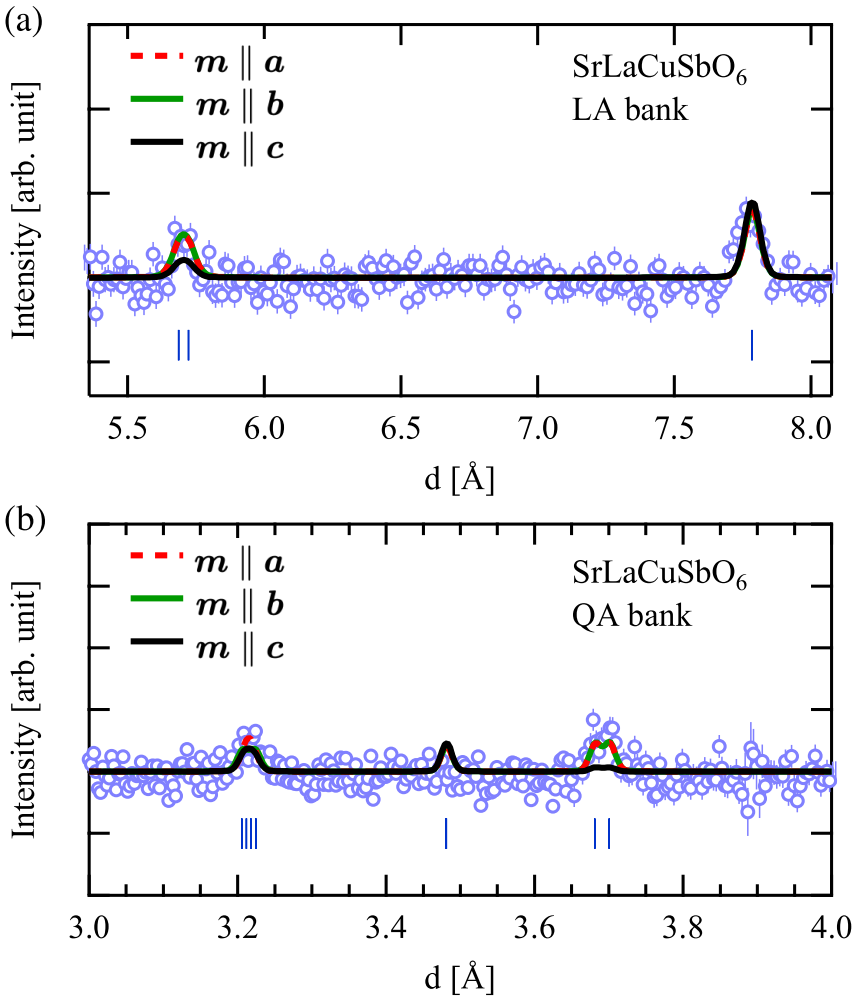

Figure 3.27: NPD spectra collected from the (a) LA and (b) QA banks at 3.5 K for SLCSO, where the diffraction spectrum at 20 K was subtracted as the background. The red, green, and black lines are patterns calculated in accordance with the Γ_2-based model described in the text. The vertical bars are the expected magnetic reflection positions for the propagation vector $\boldsymbol{k} = (1/2, 1/2, 0)$.

diffraction patterns are well reproduced by the models with $\boldsymbol{m} \parallel \boldsymbol{a}$ and $\boldsymbol{m} \parallel \boldsymbol{b}$ rather than $\boldsymbol{m} \parallel \boldsymbol{c}$, although the former two models are indistinguishable with the present data. The R-factors and magnetic moments for these models are listed in Table 3.6. From these results, it is concluded that the ordered magnetic moments lie in the ab-plane in the magnetically ordered state of SLCSO. The refined Cu^{2+} total magnetic moment, that is, the average of those for the two Γ_2 models with $\boldsymbol{m} \parallel \boldsymbol{a}$ and $\boldsymbol{m} \parallel \boldsymbol{b}$, is $0.39(3)\,\mu_B$, which is considerably smaller than $m = 0.69(6)\,\mu_B$ observed at 1.6 K for Sr_2CuTeO_6 [103].

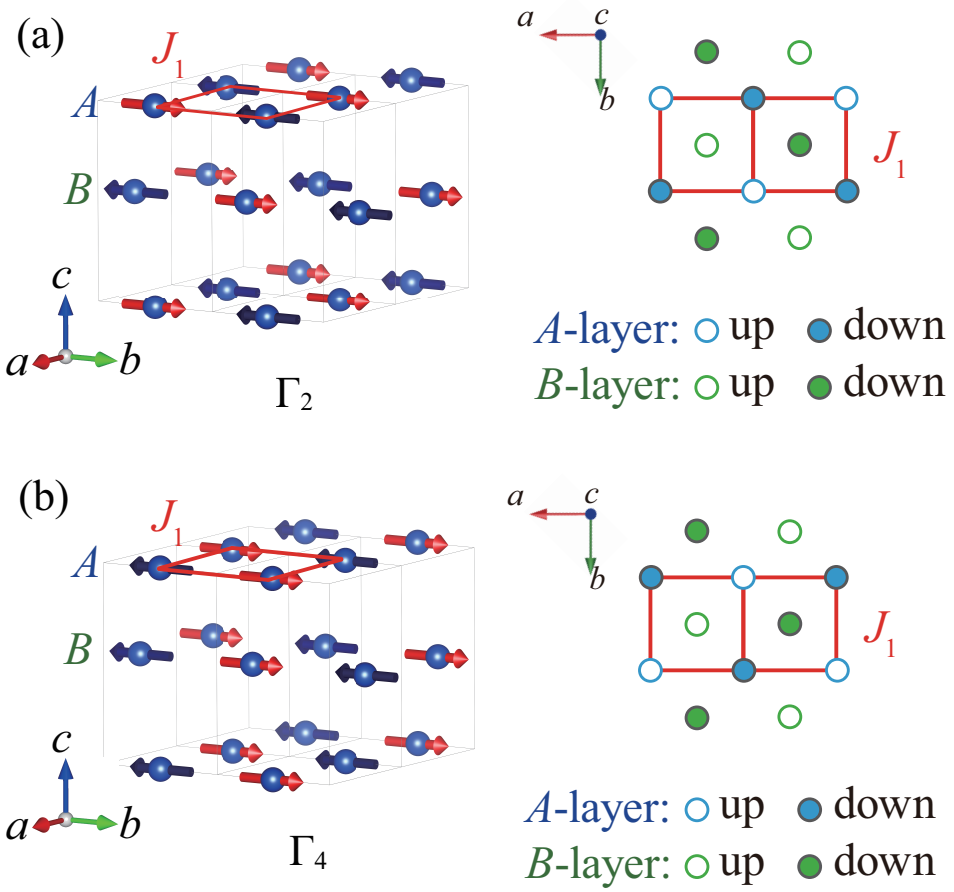

Figure 3.28: Possible magnetic structures of (a) Γ_2 and (b) Γ_4 models for SLCSO obtained by the irreducible representation analysis of the $P2_1/n$ crystal structure.

Table 3.6: R-factors and magnetic moments obtained by magnetic structure refinement based on the three Γ_2 models for $SrLaCuSbO_6$.

	LA bank			QA bank			
Model	$R_{wp}(\%)$	$R_e(\%)$	χ^2	$R_{wp}(\%)$	$R_e(\%)$	χ^2	$m\,(\mu_B)$
$\boldsymbol{m} \parallel \boldsymbol{a}$	74.1	65.5	1.28	84.6	71.3	1.41	0.38(2)
$\boldsymbol{m} \parallel \boldsymbol{b}$	74.2	65.5	1.28	84.0	71.3	1.39	0.39(2)
$\boldsymbol{m} \parallel \boldsymbol{c}$	76.0	65.5	1.35	95.0	71.3	1.78	0.29(2)

$SrLaCuNbO_6$

Figure 3.29 shows NPD spectra of SLCNO collected from the LA bank at 3.5 K, where the diffraction spectrum at 20 K ($> T_N = 15.7$ K) has been subtracted so that only magnetic Bragg peaks are extracted. All the magnetic peaks can be indexed by the propagation vector $\boldsymbol{k} = (-1/2, 1/2, 1/2)$ on the face-centered structure. This indicates that the magnetic structure in the 2D layer of SLCNO is CAF, which is also observed in Sr_2CuWO_6 [105].

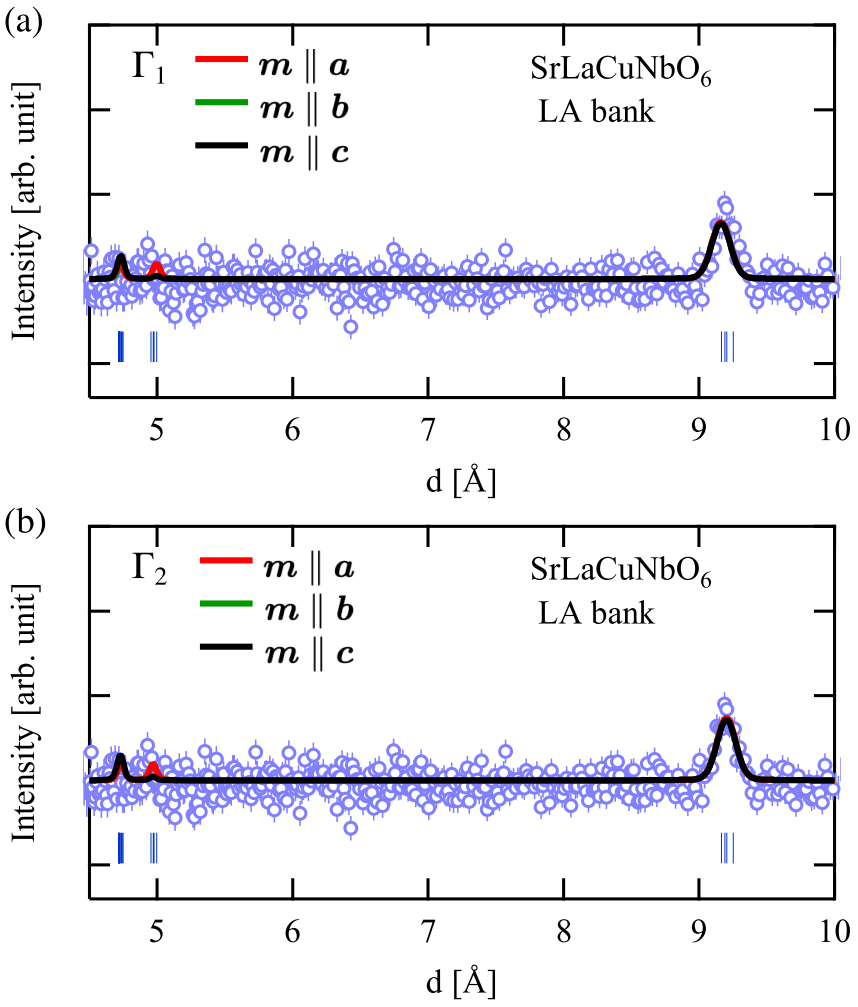

Figure 3.29: NPD spectra of SLCNO collected from the LA bank at 3.5 K, where the diffraction spectrum at 20 K was subtracted as the background. The red, green, and black lines are patterns calculated in accordance with the (a) Γ_1- and (b) Γ_2-based models described in the text. The vertical bars are the expected magnetic reflection positions for the propagation vector $\boldsymbol{k} = (-1/2, 1/2, 1/2)$.

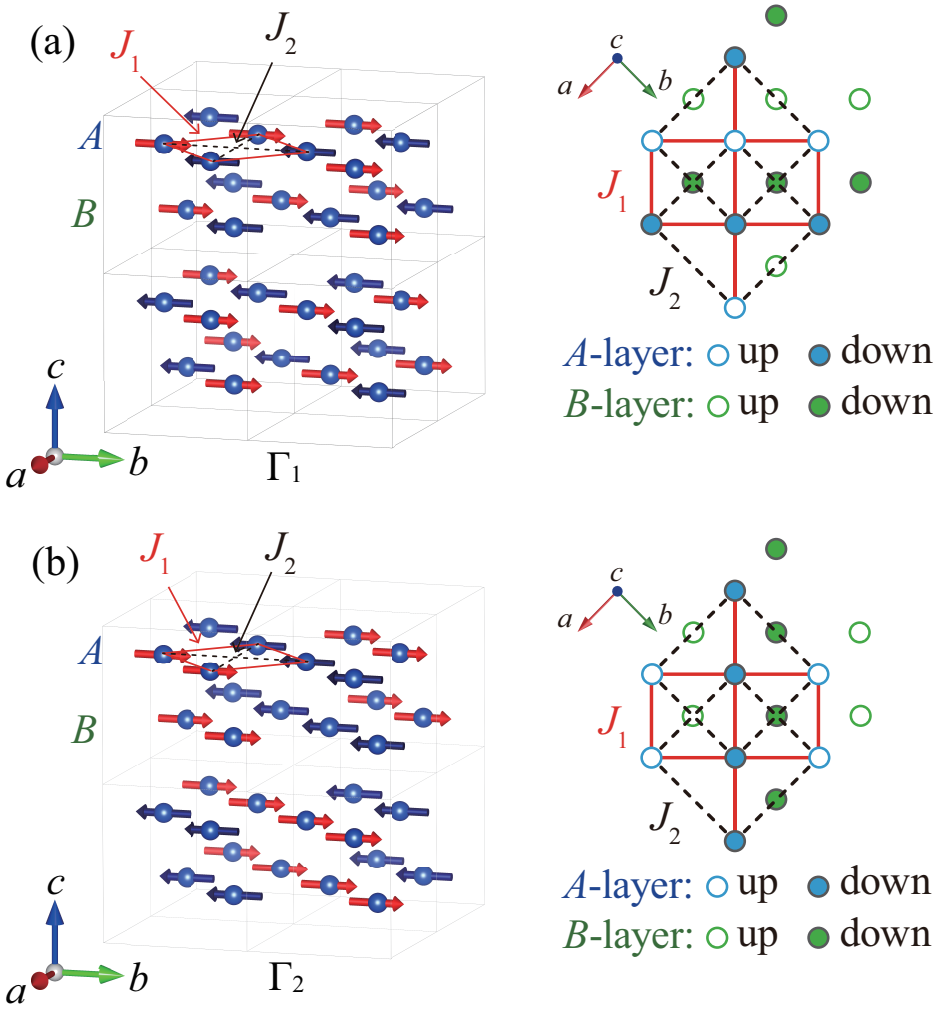

Figure 3.30: Possible magnetic structures of (a) Γ_1 and (b) Γ_2 models for SLCNO obtained by the irreducible representation analysis of the $P\bar{1}$ crystal structure.

To determine the possible magnetic structures of SLCNO, irreducible representation analysis using the SARAh program [127] was performed for the $P\bar{1}$ crystal structure. In SLCNO, both Cu1 and Cu2 occupy the Wyckoff $2i$ position, which has two identical sites of $(x, y, z) = (X, Y, Z)$ and $(-X, -Y, -Z)$. The magnetic representation of both the Cu1 and Cu2 sites are described by $\Gamma_{\mathrm{mag}} = 3\Gamma_1^1 + 3\Gamma_2^1$ in Kovalev's notation for $\boldsymbol{k} = (-1/2, 1/2, 1/2)$ in the $P\bar{1}$ crystal structure. This indicates that there are two possible magnetic structures corresponding to $\Gamma_{\mathrm{mag}} = 3\Gamma_1$ and $3\Gamma_2$, assuming that magnetic moments on the Cu1 and Cu2 sites belong to the same irreducible representation, as shown in Fig. 3.30. In the Γ_1 model, if one sublattice magnetic moment is expressed as (m_x, m_y, m_z), where the x-, y-, and z-axes are chosen to be parallel to the lattice vectors $\boldsymbol{a}$, $\boldsymbol{b}$, and $\boldsymbol{c}$, respectively, the other is expressed as

(m_x, m_y, m_z). On the other hand, in the Γ_2 model, if one sublattice magnetic moment is expressed by the basis vector (m_x, m_y, m_z), the other is given by $(-m_x, -m_y, -m_z)$.

For both the Γ_1 and Γ_2 models, a strong diffraction peak is observed around at $d \approx 9.2$ Å. This peak is $(1/2, 1/2, -1/2)$ reflection with $d = 9.165$ Å for the Γ_1 model, while for the Γ_2 model, it is $(-1/2, 1/2, 1/2)$ reflection with $d = 9.205$ Å. The d-spacing for the $(-1/2, 1/2, 1/2)$ reflection is slightly larger than that for $(1/2, 1/2, -1/2)$, indicative of Γ_2 structure with $\boldsymbol{k} = (-1/2, 1/2, 1/2)$. The R-factors of the refinement and magnetic moments for the Γ_1 and Γ_2 models are listed in Table 3.7. We can see that the Γ_2 model reproduces the experimental diffraction patterns more accurately than the Γ_1 model. However, it is difficult to determine the orientation of the ordered moment from the present experiment. To evaluate the magnitude of the ordered magnetic moment, we examined three Γ_2-based models with magnetic moments parallel to the a-, b-, and c-axes, and took the average. The refined Cu^{2+} total magnetic moment was evaluated to be $0.37(1)\,\mu_B$, which is approximately two-thirds of $m = 0.57(1)\,\mu_B$ observed at 3 K for Sr_2CuWO_6 [105].

Table 3.7: R-factors and magnetic moments obtained by magnetic structure refinement based on the Γ_1 and Γ_2 models for $SrLaCuNbO_6$.

	Γ_1			Γ_2		
Model	$R_{wp}(\%)$	χ^{21}	$m(\mu_B)$	$R_{wp}(\%)$	χ^{21}	$m\,(\mu_B)$
$\boldsymbol{m} \parallel \boldsymbol{a}$	73.7	1.42	0.36(2)	66.3	1.15	0.37(1)
$\boldsymbol{m} \parallel \boldsymbol{b}$	73.2	1.40	0.36(2)	66.8	1.16	0.37(1)
$\boldsymbol{m} \parallel \boldsymbol{c}$	74.3	1.44	0.34(1)	68.7	1.23	0.35(1)

3.3 Discussion

3.3.1 Super-exchange interaction in $SrLaCuSbO_6$ and $SrLaCuNbO_6$

The present NPD experiments reveal that the magnetic structure in the 2D layer of SLCSO is NAF, which is identical to that of Sr_2CuTeO_6 [103], while the magnetic structure in the 2D layer of SLCNO is CAF, which is identical to that of Sr_2CuWO_6 [105]. These results confirm that the NN interaction J_1 and the NNN interaction J_2 are dominant in SLCSO and SLCNO, respectively. This difference can be explained by the super-exchange interactions according to the Kanamori theory [128] as an analog to the cases of Sr_2CuTeO_6 and Sr_2CuWO_6.

In SLCSO and SLCNO, the $Cu^{2+} - O^{2-} - O^{2-} - Cu^{2+}$ path is one of the dominant paths between the NN Cu ions, as shown in Fig. 3.31 (a), and is considered to be antiferromagnetic, as observed in many magnetic materials. The super-exchange interaction via this path gives an antiferromagnetic contribution to the J_1 interaction. The other possible dominant path is $Cu^{2+} - O^{2-} - M^{5+} - O^{2-} - Cu^{2+}$, as shown in Figs. 3.31 (b) and (c), which is composed of corner-sharing CuO_6 and MO_6 octahedra with $M =$ Nb and Sb. The difference in the electronic structure of the nonmagnetic pentavalent Sb^{5+} and Nb^{5+} ions explain the difference in the magnitude of J_1 and J_2. In SLCSO, the Sb^{5+} outermost occupied $4d$ orbitals should be core-like below

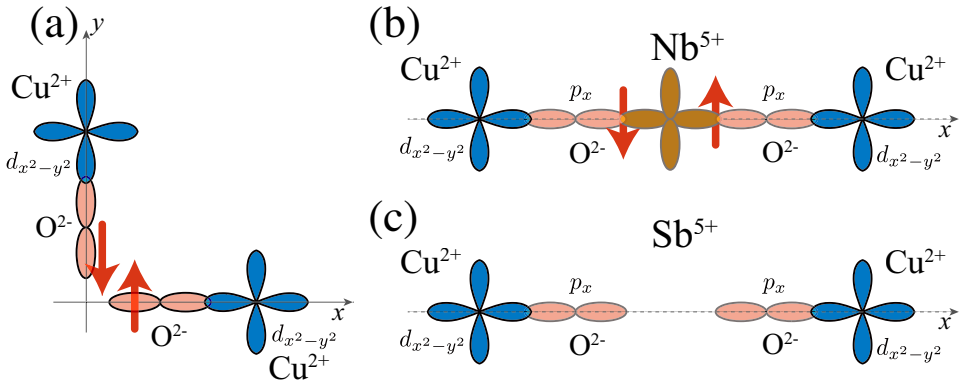

Figure 3.31: Schematic pictures of super-exchange hopping process in the c-plane. (a) $Cu^{2+} - O^{2-} - O^{2-} - Cu^{2+}$ path between nearest neighbor Cu^{2+} ions in SLCSO and SLCNO and (b) $Cu^{2+} - O^{2-} - Nb^{5+} - O^{2-} - Cu^{2+}$. path between next-nearest neighbor Cu^{2+} ions in SLCNO. (c) In SLCSO, the super-exchange hopping between next-nearest neighbor Cu^{2+} ions is suppressed by the core-like Sb^{5+} electronic state.

the valence $3d$ orbital of Cu and the $2p$ orbital of O as in the case of hexavalent Te^{6+} ions in Sr_2CuTeO_6 according to the *ab initio* calculations [106, 112, 129]. The orbital hybridization between the $4d$ orbital of Sb^{5+}, the $3d$ orbital of Cu^{2+}, and the $2p$ orbital of O^{2-} should be small. Therefore, the contribution of the $Cu^{2+}-O^{2-}-Sb^{5+}-O^{2-}-Cu^{2+}$ super-exchange path to J_2 interactions is expected to be negligible. On the other hand, in SLCNO, since the $4d$ orbital of Nb^{5+} is unoccupied, the $4d$ orbital can hybridize with the Cu^{2+} $3d$ and O^{2-} $2p$ orbitals in the valence band as in the case of hexavalent W^{6+} ions in Sr_2CuWO_6 [112, 129]. This hybridization allows the $Cu^{2+}-O^{2-}-Nb^{5+}-O^{2-}-Cu^{2+}$ super-exchange path, leading to the prominent antiferromagnetic contribution to the J_2 interaction. For these reasons, it is deduced that in SLCSO, the NN interaction J_1 is strongly antiferromagnetic and the NNN interaction J_2 is negligible, while in SLCNO, J_2 is stronger than J_1, but they are of the same order of magnitude.

3.3.2 Magnetic models of $SrLaCuSbO_6$ and $SrLaCuNbO_6$

We estimate the exchange constants of SLCSO from the magnetic susceptibility data using the [5, 5] Padé approximation combined with the result of the high-temperature series expansion (HTSE) for the magnetic susceptibility of $S=\frac{1}{2}$ J_1–J_2 SLHAF model up to the tenth order of J/k_BT [118]. The best fit between 25 and 300 K under the condition of $|J_1|>|J_2|$ is obtained with $J_1/k_B=74.7(1)$ K and $J_2/k_B=1.62(4)$ K using an average g-factor of $g_{avg}=2.197$ determined from the ESR measurement. The magnetic susceptibility calculated with these parameters is shown by a blue solid line in Fig. 3.32. The calculated magnetic susceptibility fit well the experimental result, although slight disagreement is observed around the broad anomaly at $T_{max}=71$ K. In SLCSO, CuO_6 octahedra are rotated in the same direction around the b-axis as shown in Fig. 3.6 (a), which could induce spatial anisotropy in exchange interactions.

Magnetic specific heat C_{mag} exhibits a rounded maximum at $T^*_{max}=44$ K owing to the short-range spin correlation, as shown in Fig. 3.11 (a). The value of the C_{mag} at T^*_{max} is $C^{max}_{mag}=0.47\,R$, which coincides with that for an $S=1/2$ SLHAF with the NN interaction [120]. Using a relation $T^*_{max}=0.582\,J/k_B$ for the $S=1/2$ SLHAF with the NN interaction [120], we obtain $J/k_B,=76$ K, which is very close to $J_1/k_B=74.7$ K obtained from the analysis of the magnetic susceptibility based on the $S=1/2$ J_1–J_2 SLHAF model. From these specific heat results, we can deduce that SLCSO is described as a uniform $S=1/2$

J_1-J_2 SLHAF with dominant NN interaction, and that the exchange constants $J_1/k_B = 74.7\,\mathrm{K}$ and $J_2/k_B = 1.62\,\mathrm{K}$ obtained from the magnetic susceptibility data are reasonable.

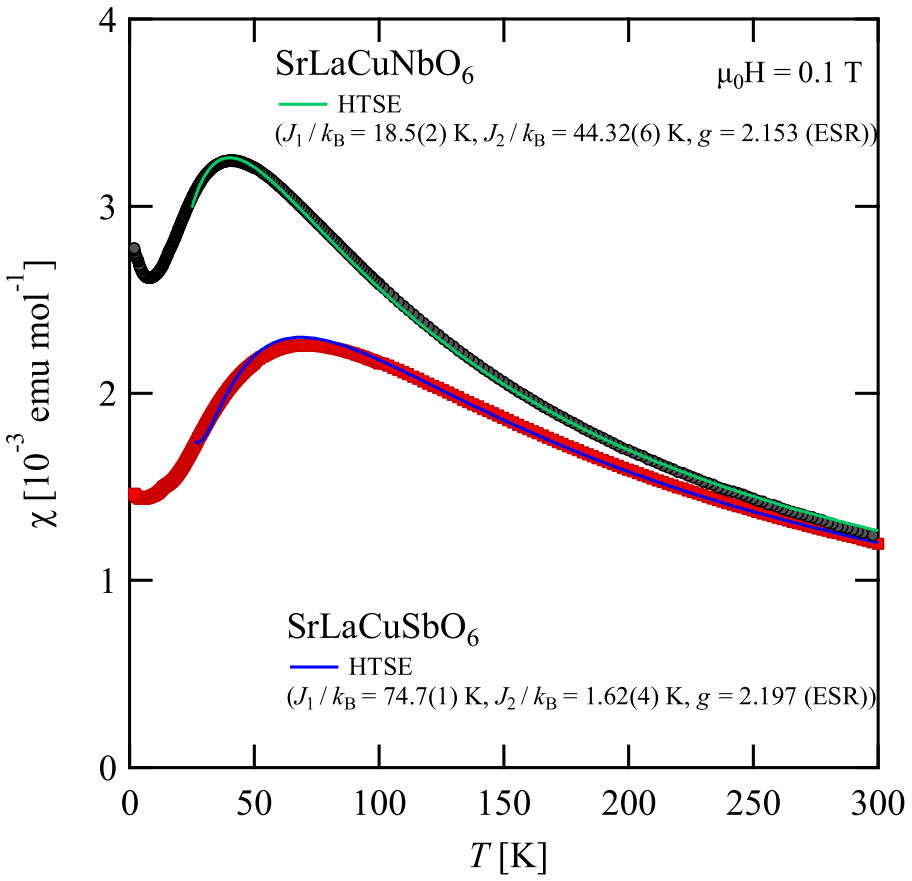

Figure 3.32: Temperature dependence of magnetic susceptibilities χ of SLCSO (red squares) and SLCNO (black circles) measured at $\mu_0 H = 0.1\,\mathrm{T}$. The green and blue solid curves are fits by the HTSEs of the $S = 1/2$ $J_1 - J_2$ SLHAF for SLCNO and SLCSO, respectively.

The exchange constants J_1 and J_2 of SLCNO were estimated by the [5, 5] Padé approximation using the result of HTSE for the magnetic susceptibility of the $S = 1/2$ $J_1 - J_2$ SLHAF up to the tenth order of $J_n/k_B T$ ($n = 1$ and 2) [118] in a similar way to the analysis of SLCSO. The best fit between 25 and 300 K under the condition of $|J_2| > |J_1|$ is obtained with $J_1/k_B = 18.5(2)$ and $J_2/k_B = 44.32(5)\,\mathrm{K}$ using $g_{\mathrm{avg}} = 2.153$ evaluated from the ESR measurement, which is shown by the green solid line in Fig. 3.8 (a). The calculated magnetic susceptibility is in good agreement with the experimental data. Thus, it is concluded that SLCNO is described as an $S = 1/2$ $J_1 - J_2$ SLHAF with $J_1/J_2 = 0.42$.

From the Rietveld analysis, the magnitudes of the ordered moments of

SLCSO and SLCNO were found to be $m = 0.39(3)\,\mu_B$ and $0.37(1)\,\mu_B$ at 3.5 K, respectively. These values are significantly smaller than those of their counterparts Sr_2CuTeO_6 and Sr_2CuWO_6, in which $m = 0.69(6)\,\mu_B$ at 1.5 K [103] and $0.57(1)\,\mu_B$ at 3 K, respectively [105]. The linear spin wave theory (LSWT) [111] does not reproduce well the magnitudes of the observed magnetic moments of SLCSO and SLCNO. The LSWT calculation for the uniform $S = 1/2$ SLHAF gives $m_{calc} = 0.303\,g_{avg} = 0.666\,\mu_B$ [130]. The calculated ordered moment is 1.7 times larger than the experimental value for SLCSO. For SLCNO, the LSWT calculation for the $S = 1/2$ $J_1 - J_2$ SLHAF with $J_1/k_B = 18.5$ K and $J_2/k_B = 44.3$ K gives $m_{calc} = 0.65\,\mu_B$, which is 1.75 times larger than the observed value for SLCNO. We infer that the small observed ordered magnetic moment is ascribed to the bond randomness effect caused by the site disorder of Sr^{2+} and La^{3+} ions. Some theories show that when frustration is weak, the bond randomness does not destroy the magnetic ordering, while it reduces the magnitude of the ordered moment [48, 131]. In the μSR measurement, very fast damping was observed in the ZF μ SR spectrum, indicative of a wide distribution of static internal magnetic fields. This suggests that the ordered magnetization may be spatially inhomogeneous. It is considered that the site disorder of Sr^{2+} and La^{3+} ions in SLCSO and SLCNO disturbs the local crystal structure and induce weak randomness in the exchange interactions J_1 and J_2.

3.4 Summary

We have presented the results of NPD, ESR, μSR, magnetization, and specific heat measurements on SLCSO and SLCNO powders. Magnetization and specific heat measurements show that the quasi-two-dimensional $S = 1/2$ SLHAFs SLCSO and SLCNO undergo three-dimensional magnetic ordering at $T_N = 13.6$ and 15.7 K, respectively. From NPD measurements, the magnetic structures in 2D layers of SLCSO and SLCNO were determined to be of the Néel antiferromagnetic (NAF) type characterized by the propagation vector $\boldsymbol{k} = (1/2, 1/2, 0)$ on the body-centered structure and of the columnar antiferromagnetic (CAF) type described by the propagation vector $\boldsymbol{k} = (-1/2, 1/2, 1/2)$ on the face-centered structure, respectively. The exchange parameters of SLCSO were estimated to be $J_1/k_B = 74.7$ K and $J_2/k_B = 1.62$ K, which are in the parameter range for the NAF order. On the other hand, the exchange parameters of SLCNO were estimated to be $J_1/k_B = 18.5$ K and $J_2/k_B = 44.3$ K, which are in the parameter range for the CAF order. The difference in the relative size of

J_2 to J_1 between these two compounds is attributed to whether the electronic configuration of the nonmagnetic pentavalent ions of Nb^{5+} and Sb^{5+} is d^0 or d^{10}. The magnitudes of the ordered moments of SLCSO and SLCNO were evaluated to be $m = 0.39(3)\,\mu_B$ and $0.37(1)\,\mu_B$ at 3.5 K, respectively, both of which are significantly smaller than those observed in the related systems Sr_2CuTeO_6 and Sr_2CuWO_6, and those calculated by the linear spin wave theory. This is consistent with the results of μSR measurements, which imply a broad internal field distribution due to spatially inhomogeneous ordered magnetization. We infer that the small ordered magnetic moments observed in SLCSO and SLCNO are ascribed to the effect of bond randomness arising from the disorder of Sr^{2+} and La^{3+} ions. SLCSO and SLCNO are thus magnetically described as $S = 1/2$ $J_1 - J_2$ SLHAFs with weak bond randomness.

Chapter 4

Effect of Strong Bond Randomness in Spin-1/2 J_1-J_2 Square-Lattice Antiferromagnets: $SrLaCuSb_{1-x}Nb_xO_6$

B-site ordered double perovskites $SrLaCuSbO_6$ (SLCSO) and $SrLaCuNbO_6$ (SLCNO) are magnetically described as $S=1/2$ J_1-J_2 quasi-square lattice antiferromagnet with weak bond randomness as shown in Chap. 3. The temperature dependence of the magnetic susceptibility and specific heat of these materials showed good two-dimensionality, while long-range magnetic ordering was observed at $T=13.6\,\mathrm{K}$ in SLCSO and at $T=15.7\,\mathrm{K}$ in SLCNO. Bond randomness is expected to be induced by the random occupation of the A-site by Sr^{2+} and La^{3+} ions. However, the bond randomness caused by the structural disorder was not strong enough to destroy their magnetic ordering.

To clarify the nature of the ground state when stronger bond randomness is introduced, I focused on the solid solution $SrLaCuSb_{1-x}Nb_xO_6$. In the parent materials, SLCSO and SLCNO, it was found that the difference in the electronic states of the nonmagnetic Sb and Nb ions makes a drastic effect on the magnitude of J_1 and J_2. Therefore, stronger randomness of the exchange interaction is expected to be induced in $SrLaCuSb_{1-x}Nb_xO_6$, where Sb and Nb are disordered.

4.1 Introduction

4.1.1 Theoretical study of bond randomness effects in square lattice quantum antiferromagnets

The $S=1/2$ square lattice Heisenberg antiferromagnet (SLHAF) is a prototypical quantum spin model, in which frustration does not occur in the case of nearest-neighbor interactions only. The bond-randomness effect in the SLHAF was studied theoretically in Ref. [51, 131]. The model Hamiltonian is given by

$$\mathcal{H} = \sum_{i,j} J_{i,j} \boldsymbol{S}_i \cdot \boldsymbol{S}_j \tag{4.1}$$

where $\boldsymbol{S}_i = (S_i^x, S_i^y, S_i^z)$ is an $S=1/2$ spin operator at the i-th site on the square lattice and $J_{i,j}$ (> 0) is the random nearest-neighbor antiferromagnetic coupling. In Ref. [51], the random interaction $J_{i,j}$ is considered to be uniformly distributed between $(1-\Delta)J$ and $(1+\Delta)J$. The exact diagonalization calculation shows that sublattice magnetization survives against the bond randomness as shown in Figure 4.1. In addition, the calculated ground-state static spin structure factor $S(\boldsymbol{q})$ shows no clear difference between $\Delta=0$ and $\Delta=1$ cases, as shown in Figure 4.2. In the square lattice, an antiferromagnetic long-range ordering is robust against the bond-randomness.

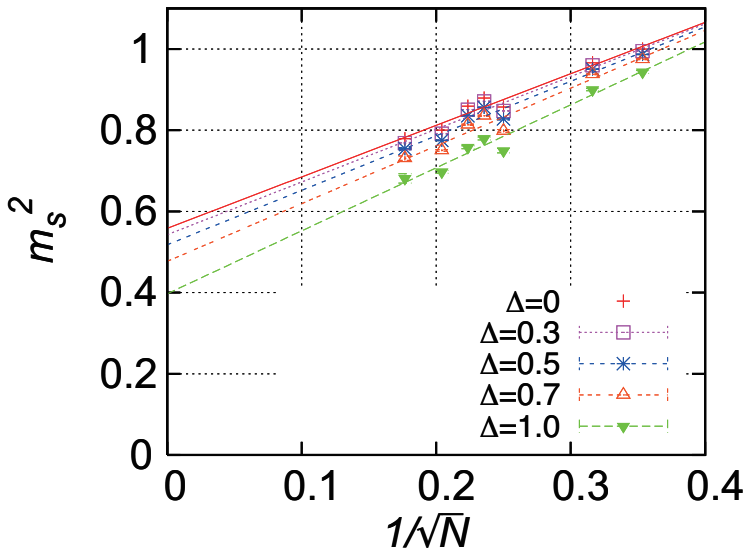

Figure 4.1: The rescaled ground-state squared sublattice magnetization per spin, m^2, of the square lattice Heisenberg antiferromagnet plotted vs $1/\sqrt{N}$ (N the lattice size) for several values of the randomness Δ, reprinted from Ref. [51].

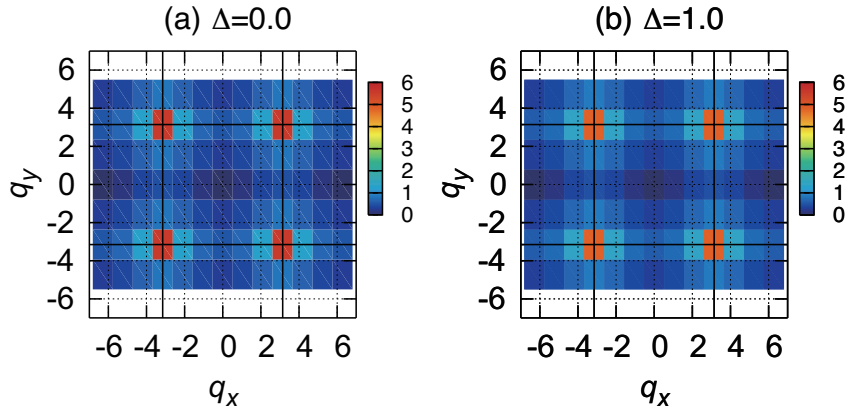

Figure 4.2: Intensity plots of the ground-state static spin structure factor $S(\boldsymbol{q})$ of the square lattice Heisenberg antiferromagnet in the wave-vector (q_x, q_y) plane for the randomness $\Delta = 0$ (a), and 1 (b). The solid black line represents the zone boundary of the first Brillouin Zone (BZ) of the square lattice, reprinted from Ref. [51].

4.1.2 Theoretical study on the effect of the exchange randomness on the frustrated quantum magnets

The effect of exchange randomness on the frustrated quantum magnets was investigated theoretically [38, 46–52, 60, 63, 64, 123, 132, 133]. Here, I briefly summarize theoretical results on the $S = 1/2$ random J_1-J_2 SLHAFs studied by Uematsu and Kawamura [48].

They discussed the bond-random $S = 1/2$ isotropic Henisenberg model on the square lattice with antiferromagnetic nearest-neighbor and next-nearest-neighbor interactions ($J_1 > 0$ and $J_2 > 0$). The Hamiltonian is given by

$$\mathcal{H} = J_1 \sum_{\langle i,j \rangle} j_{ij} \boldsymbol{S}_i \cdot \boldsymbol{S}_j + J_2 \sum_{\langle\langle i,j \rangle\rangle} j_{ij} \boldsymbol{S}_i \cdot \boldsymbol{S}_j \tag{4.2}$$

where the sums $\langle i, j \rangle$ and $\langle\langle i, j \rangle\rangle$ are taken over all the nearest-neighbor and next-nearest-neighbor pairs on the lattice, respectively, while j_{ij} is randomly distributed between $1 - \Delta$ and $1 + \Delta$ with $0 \leq \Delta \leq 1$. In the analysis, the J_1 is fixed to be $J_1 = 1$, and J_2 and Δ were set to be free. $\Delta = 0$ corresponds to the uniform case and $\Delta = 1$ to the maximally random case. They calculated the sublattice magnetization, spin freezing parameters, thermodynamic properties, and dynamical spin structure factors, using exact diagonalization for up to 32 sites.

They presented the ground-state phase diagram for J_2 versus Δ as shown in Figure 4.3. It was revealed that the exchange randomness suppresses a

magnetic ordering and stabilize the random singlet (RS) or the spin-glass (SG) state for the frustrated case ($J_2 \neq 0$ and 1). The RS state is one of QDGSs, which is composed of randomly frozen singlets, which are formed between not only nearest-neighbor spins but also distant spins.

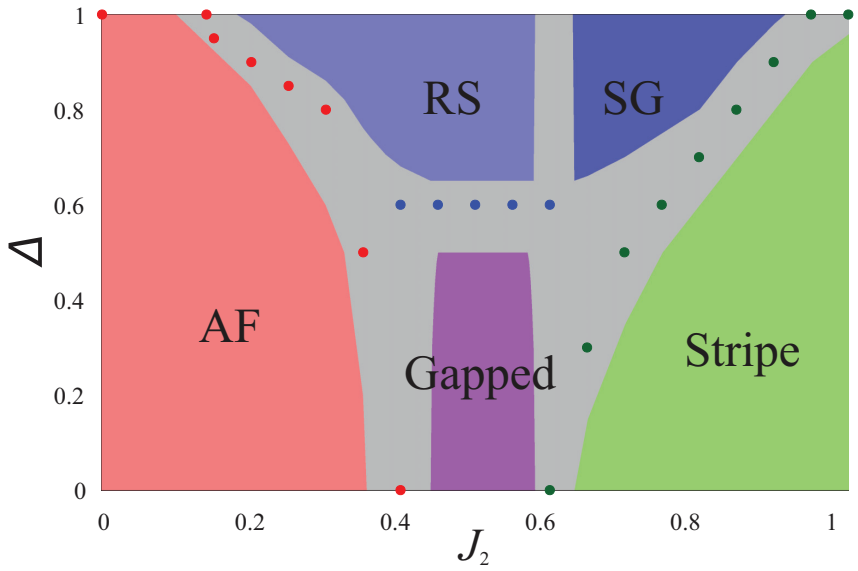

Figure 4.3: Ground state phase diagram of the $S = 1/2$ random bond J_1-J_2 Heisenberg model on the square lattice on the frustration (J_2) versus the randomness (Δ) plane, reprinted from Ref. [48].

The numerical calculation revealed a finite Curie-like paramagnetic susceptibility and a low-temperature specific heat proportional to the temperature T, which arises from a number of singlet spin pairs that can be easily excited to triplets with a small or zero energy, as shown in Figure 4.4.

Sign-problem free quantum Monte Carlo calculation of $S = 1/2$ $J-Q$ model on a square lattice indicated that the temperature dependence of the magnetic susceptibility $\chi(T)$ and specific heat $C(T)$ in the low-temperature region are represented as

$$\chi(T) \propto T^{-\gamma}, \tag{4.3}$$

$$C(T) \propto T^{1-\gamma}, \tag{4.4}$$

with $0 < \gamma < 1$, where γ is defined as $\gamma = 1 - 2/z$ with dynamic critical exponent z. $\chi(T)$ and $C(T)/T$show the same divergence.

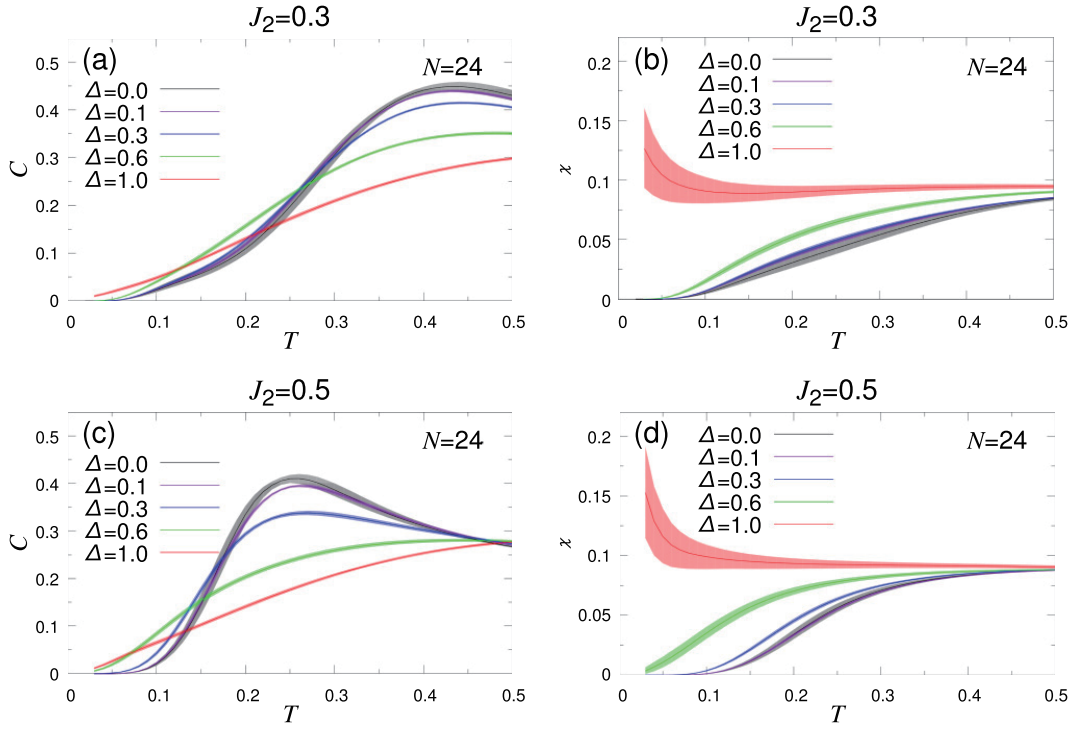

Figure 4.4: Temperature dependence of the specific heat C, and of the uniform susceptibility χ for various values of Δ for (a) and (b) $J_2 = 0.3$, and (c) and (d) $J_2 = 0.5$. Reprinted from Ref. [48].

4.1.3 Spin-1/2 random $J_1 - J_2$ square lattice antiferromagnet $Sr_2CuTe_{1-x}W_xO_6$

To the best of my knowledge, $Sr_2CuTe_{1-x}W_xO_6$ is the first model material for $S = 1/2$ random $J_1 - J_2$ SLHAF [109, 119]. Two parent compounds, Sr_2CuWO_6 and Sr_2CuTeO_6, have the tetragonal structure, in which CuO_6 and MO_6 octahedra are arranged alternately in the ab plane, sharing their corners. CuO_6 octahedra are elongated approximately parallel to the c-axis owing to the Jahn–Teller effect. Consequently, the hole orbitals $d_{x^2-y^2}$ of Cu^{2+} ions with spin-1/2 lie in the ab-plane, which leads to good two-dimensionality. Consequently, Sr_2CuWO_6 and Sr_2CuTeO_6 are described as quasi-2D $S = 1/2$ $J_1 - J_2$ SLHAFs. On the other hand, the magnitude of J_1 and J_2 depends on nonmagnetic hexavalent ions W^{6+} and Te^{6+}. In Sr_2CuTeO_6, J_1 is dominant, while J_2 is dominant in Sr_2CuWO_6. Thus, the random substitution of W^{6+} ions for Te^{6+} ions induces exchange randomness for J_1 and J_2 in the mixed system of $Sr_2CuTe_{1-x}W_xO_6$. Thus, $Sr_2CuTe_{1-x}W_xO_6$ is magnetically described as $S = 1/2$ random $J_1 - J_2$ SLHAF.

Thermodynamic properties

Figure 4.5 shows temperature dependence of magnetic susceptibility $\chi(T)$ of $Sr_2CuTe_{1-x}W_xO_6$ measured at $\mu_0 H = 0.1\,\mathrm{T}$ with $0 \leq x \leq 0.5$, $x = 1$. The Curie–Weiss-like upturn at low temperatures is is observed, which is consistent with theoretical studies using exact diagonalization calculations [48] and QMC calculations [63, 64]. The low-temperature magnetic susceptibility $\chi(T)$ follows a power law expressed by $\chi = \chi_0 + cT^{-\alpha}$ with $\alpha < 1$, which was predicted to appear in the 2D RS state by Liu *et al.* [64]. Moreover, it was predicted that if $\chi(T)$ follows such a power law, the temperature dependence of the specific heat is represented by $C(T) \propto T^{-\alpha+1}$ with the same α by quantum critical scaling law. However, the exact diagonalization calculations of the $S = 1/2$ random $J_1 - J_2$ SLHAF showed that the specific heat is proportional to the temperature as $C(T) \propto T$ [48].

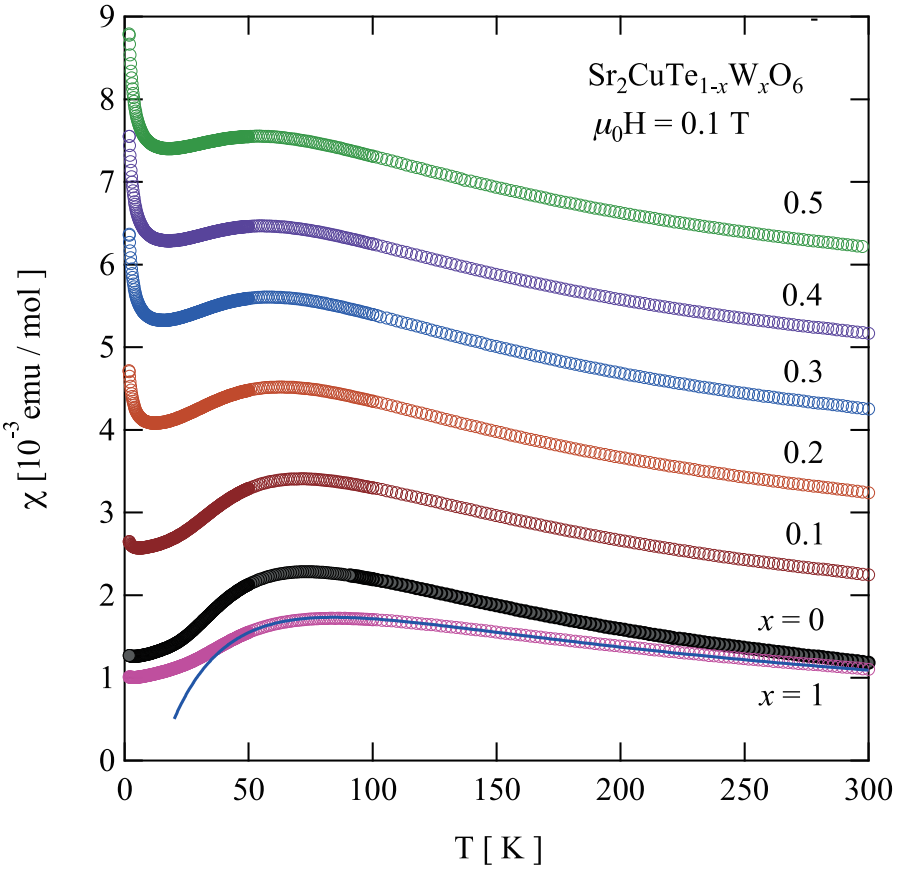

Figure 4.5: Temperature dependence of magnetic susceptibility of $Sr_2CuTe_{1-x}W_xO_6$ measured at $\mu_0 H = 0.1\,\mathrm{T}$ for various x. The susceptibility data for $0.1 \leq x \leq 0.5$ are shifted upward by multiples of 1×10^{-3} emu/mol. Adopted from Ref. [109].

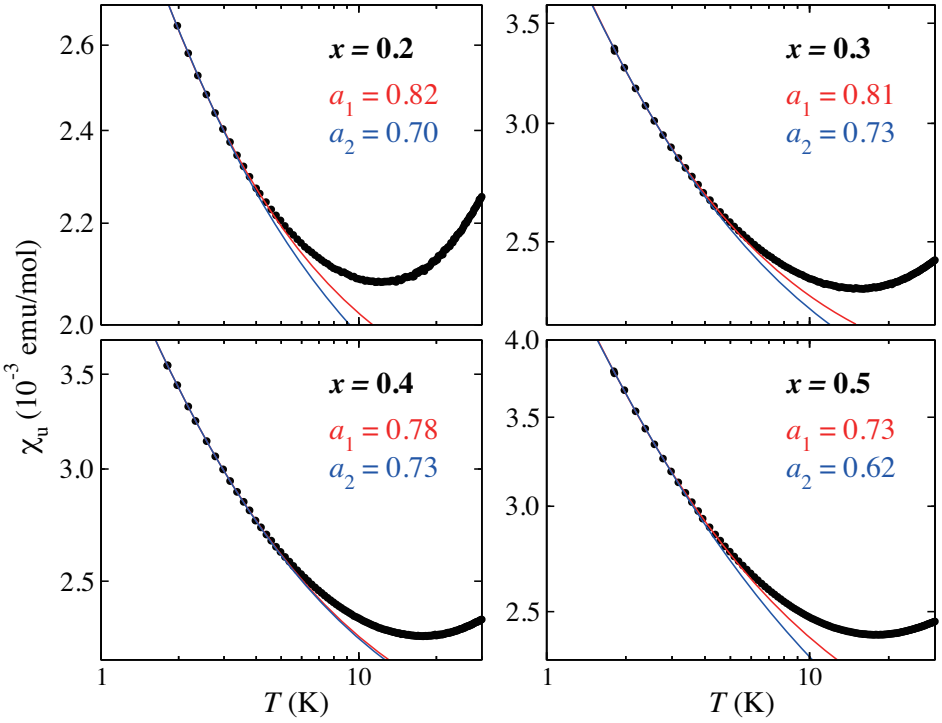

Figure 4.6: Low-temperature magnetic susceptibility of $Sr_2CuTe_{1-x}W_xO_6$. The red and blue solid curves are fits by $\chi = \chi_0 + cT^{-\alpha}$ below 4 K and 3 K, respectively. The temperature exponents (a_1 for $T < 4\,\mathrm{K}$ and a_2 for $T < 3\,\mathrm{K}$) obtained from the fits are also shown in the panels. Adopted from Ref. [64].

Figure 4.7 (a) shows temperature dependence of specific heat divided by temperature C/T of $Sr_2CuTe_{1-x}W_xO_6$ with $x = 0, 0.1, 0.2, 0.5$ and 1 measured at zero magnetic fields. For $x \neq 0$ and 1, magnetic ordering is absent. The bond randomness suppressed the magnetic ordering. The low-temperature specific heat is enhanced due to the low-energy excitations caused by the exchange randomness. In particular, it was seen that for $0.1 \leq x \leq 0.5$, a component of the specific heat proportional to temperature was observed above 1.5 K, but below 1.5 K, the contribution of the T-linear specific heat decreases. This behavior is reminiscent of a singlet gap [109] while such a singlet gap is not theoretically expected for the RS state [48].

It was reported that the magnetic field dependence of C/T became more pronounced with increasing x as shown in Fig. 4.7 (b). This magnetic field dependence of C/T was explained by the Schottky specific heat due to the weakly coupled spin dimers. Remarkably, the magnitude of the intra-dimer coupling constant is sufficiently small compared to the average interaction in $Sr_2CuTe_{1-x}W_xO_6$; thus, it is not clear what energy scale it corresponds to. It is also unclear whether these low-temperature properties are characteristic of

the RS state or only for this compound [109].

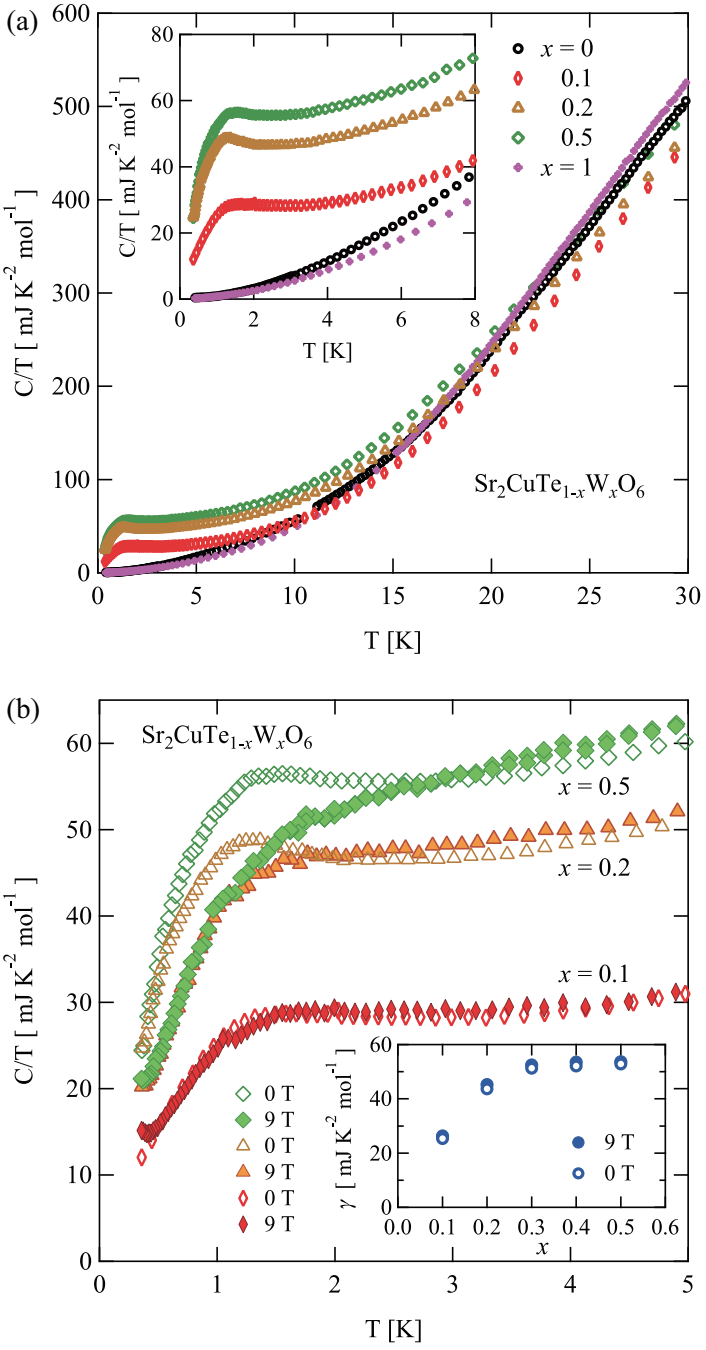

Figure 4.7: Temperature dependence of C/T of $Sr_2CuTe_{1-x}W_xO_6$ for $x = 0, 0.1, 0.2, 0.5$ and 1. The inset shows an enlargement of the data below 8 K (b) C/T for x 0.1, 0.2, and 0.5 measured at zero magnetic field (open symbols) and 9 T (closed symbols). The inset shows x dependence of the coefficient γ for the $C(T) = \gamma T$. Adopted from Ref. [109].

Sungwon Yoon *et al.* [124] performed specific heat measurements on $Sr_2CuTe_{1-x}W_xO_6$ with $x = 0.05$ and 0.1, and found that the low-temperature specific heat fol-

lows a power law, as shown in Fig. 4.8 (a). They argued that a power law gives a good description of low-temperature specific heat $C(T)$. The temperature dependence of the magnetic specific heat C_{mag} was found to be $C_{\mathrm{mag}}/T \propto T^{\gamma}$ with $\gamma = 1.2$ below 0.9 K, but $\gamma = 0.09$ between 0.9 and 4.5 K, indicating a change in the temperature exponent [124]. The magnitude of the exponent γ at low temperatures deviated from the prediction by Liu *et al* [63, 64]. The temperature dependence of the specific heat of $Sr_2CuTe_{1-x}W_xO_6$ reported so far is inconsistent with theoretical predictions for the 2D RS state based on exact diagonalization [48] and QMC calculations [63, 64].

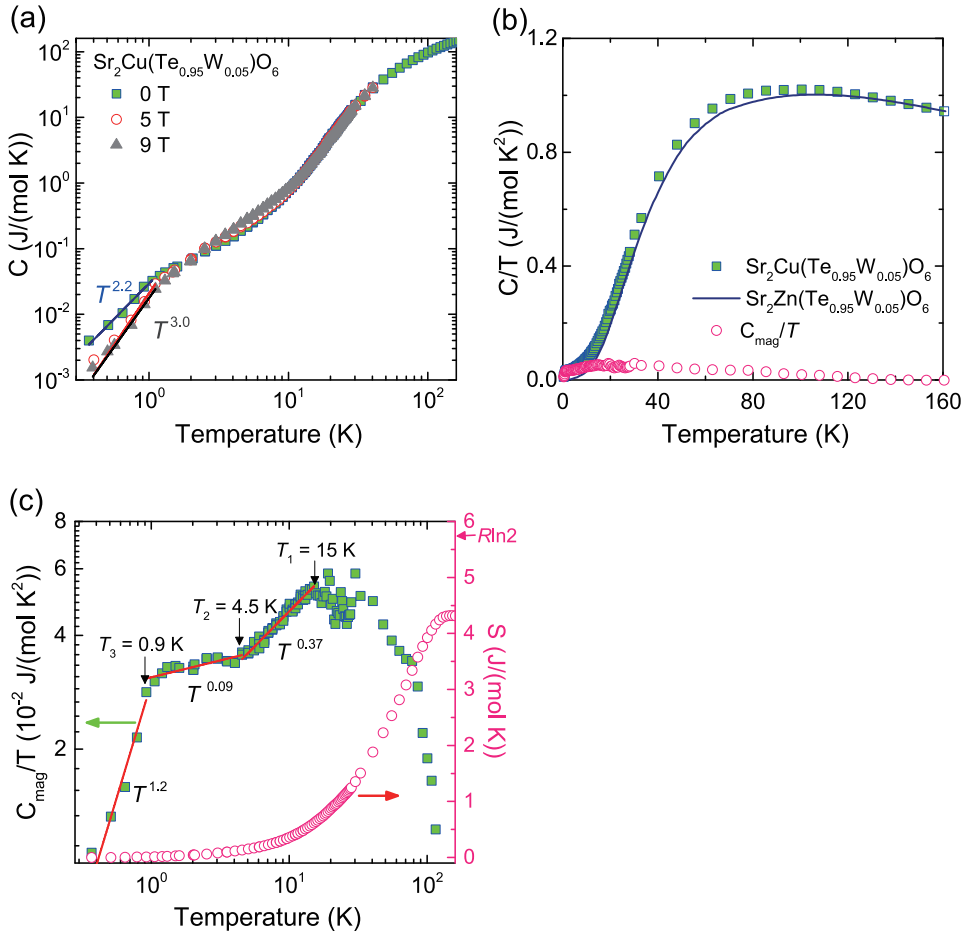

Figure 4.8: (a) Low-temperature specific heat $C(T)$ of $Sr_2CuTe_{1-x}W_xO_6$ with $x = 0.05$ measured at $\mu_0 H = 0, 5$, and 9 T in a double logarithmic scale. (b) C/T of $Sr_2CuTe_{0.95}W_{0.05}O_6$ and the non-magnetic counterpart $Sr_2ZnTe_{0.95}W_{0.05}O_6$. Magnetic contribution C_{mag}/T were obtained by subtracting the non-magnetic contribution from the raw data. (c) C_{mag}/T as a function of T in double logarithmic scale. The right axis represents the entropy. Adopted from Ref. [124].

μSR measurements

The first μSR measurements on $Sr_2CuTe_{0.5}W_{0.5}O_6$ were conducted by O. Mustonen *et al.* at the Paul Scherrer Institute, Switzerland [119]. Figures 4.9 (a) and (b) show representative μSR spectra measured at zero field (ZF) and weak transverse fields (wTF), respectively. Neither spin freezing nor magnetic ordering was observed at all down to 19 mK. The ZF μSR spectrum showed only a slow relaxation toward zero without any rotational signal. The temperature dependence of the relaxation rate obtained by fitting the ZF μSR spectra with $G_z(t) = \exp(-(\lambda t)^{\beta})$ is shown in Fig. 4.9 (c). The relaxation rate converges to a constant value at low temperatures, suggesting that the spins fluctuate even at absolute zero. Such behavior has been observed in promising candidates for QSLs such as $YbMgGaO_4$ [25] and $ZnCu_3(OH)_6Cl_2$ [21]. Figure 4.9 (d) shows the results of μSR measurements in a longitudinal field (LF) at 19 mK. The relaxation rate decreases with increasing LF. This is a typical observation of decoupling from an internal dynamical field, indicating that the spins in $Sr_2CuTe_{0.5}W_{0.5}O_6$ are dynamically fluctuating at least at 19 mK. However, a quantitative description of the LF muon spin relaxation has not been given.

Figures 4.10 show the results of μSR measurements of $Sr_2CuTe_{1-x}W_xO_6$ with $x = 0.05$ and 0.1 performed by Yoon *et al.* at RIKEN-RAL Muon facility, UK [124]. No sign of magnetic ordering was observed for $x = 0.05$. The ZF and LF μSR spectra were well reproduced by the stretched exponential decay $P(t) = P_{\rm bg} + P_1 \exp\left[-(\lambda t)^{\beta}\right]$. Figures 4.11 (a) and (b) show the temperature dependence of the relaxation rate and shape factor β extracted by the fit. The longitudinal field dependence of the relaxation rate $\lambda(H)$ is shown in Fig. 4.11 (c), which is not reproduced by the conventional Redfield law corresponding to an exponential autocorrelation function $S(t) \sim \exp(-\nu t)$. This result suggests that the spin dynamic autocorrelation function $S(t)$ should take a general form $S(t) \sim (\tau/t)^r \exp(-\nu t)$, where τ and $1/\nu$ are the early and late time cutoffs [134, 135]. Solid curves in Fig. 4.11 (c) are fits using $S(t) \sim (\tau/t)^r \exp(-\nu t)$. Yoon *et al.* [124] argued that electron spins in $Sr_2CuTe_{1-x}W_xO_6$ are entangled spatially and temporally. These LF μSR characteristics were also found in the QSL candidate $YbMgGaO_4$ [25]. However, the origin has not been clarified yet.

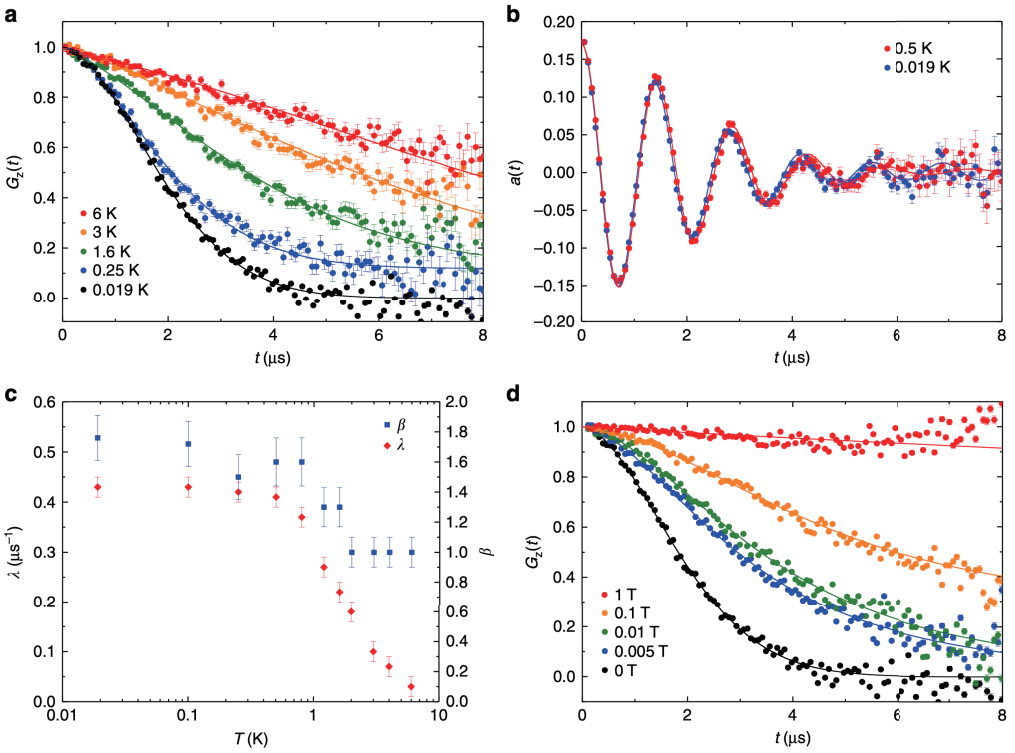

Figure 4.9: (a) ZF-μSR spectra measured at various temperatures. (b) TF-μSR spectra measured at 0.5 K and 0.019 K with 5 mT. (c) Muon spin relaxation rate λ and shape factor β as a function of temperature T. (d) LF-μSR spectra measured at 19 mK. Adopted from Ref. [119].

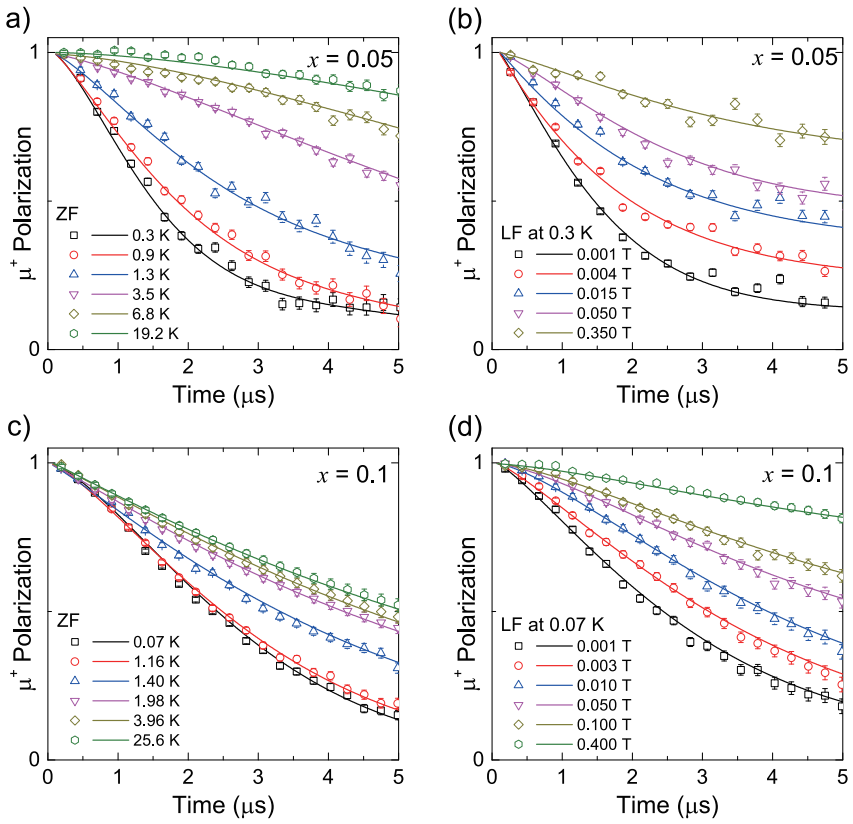

Figure 4.10: μSR spectra of $Sr_2CuTe_{1-x}W_xO_6$ for $x = 0.05$ (a) at zero field and (b) at longitudinal fields, and for $x = 0.1$ (c) at zero field and (b) at longitudinal fields. The solid curves are fits by the stretched exponential decay $P(t) = P_{\rm bg} + P_1 \exp\left[-(\lambda t)^{\beta}\right]$ Adopted from [124]

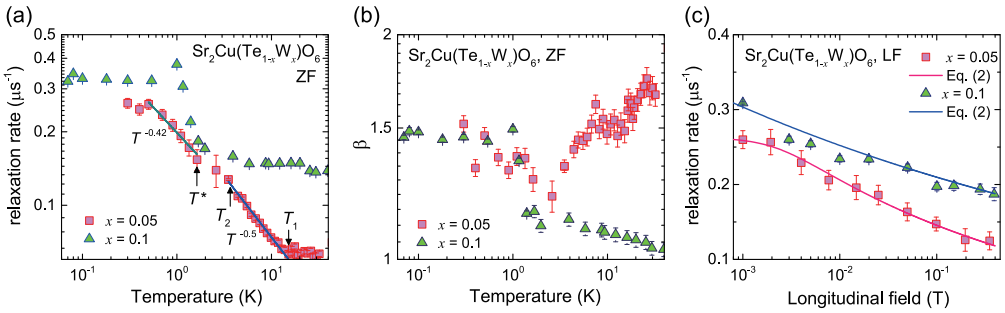

Figure 4.11: (a) Temperature dependence of muon spin relaxation rate estimated from ZF μSR meausrements for $Sr_2CuTe_{1-x}W_xO_6$ ($x = 0.05$ and 0.1) in a double logarithmic plot. (b) Shape factor β as a function of temperatures in a double logarithmic plots. (c) Longitudinal field dependence of the muon spin relaxation rate at $T = 0.3$ and 0.07 K for the case with $x = 0.05$ and 0.1, respectively. The solid curves are fits by a formula based on the general spin autocorrelation function $S(t) \sim (\tau/t)^r \exp(-\nu t)$. Adopted from Ref. [124].

4.2 Experimental results and discussion

4.2.1 X-ray diffraction and Rietveld analysis

Figure. 4.12 shows XRD patterns for the $SrLaCuSb_{1-x}Nb_xO_6$ with $0 \leq x \leq 0.5$ and $x = 1$ measured at room temperature. All the samples are found to be nearly single-phase B-site ordered double perovskites. A tiny amount of $Sr(Sb,Nb)_2O_6$ was observed. No superlattice reflection was observed, which indicates that Sb ions and Nb ions are randomly distributed on B'' (Sb^{5+}/Nb^{5+}) site, although B' (Cu^{2+}) and B'' (Sb^{5+}/Nb^{5+}) are ordered.

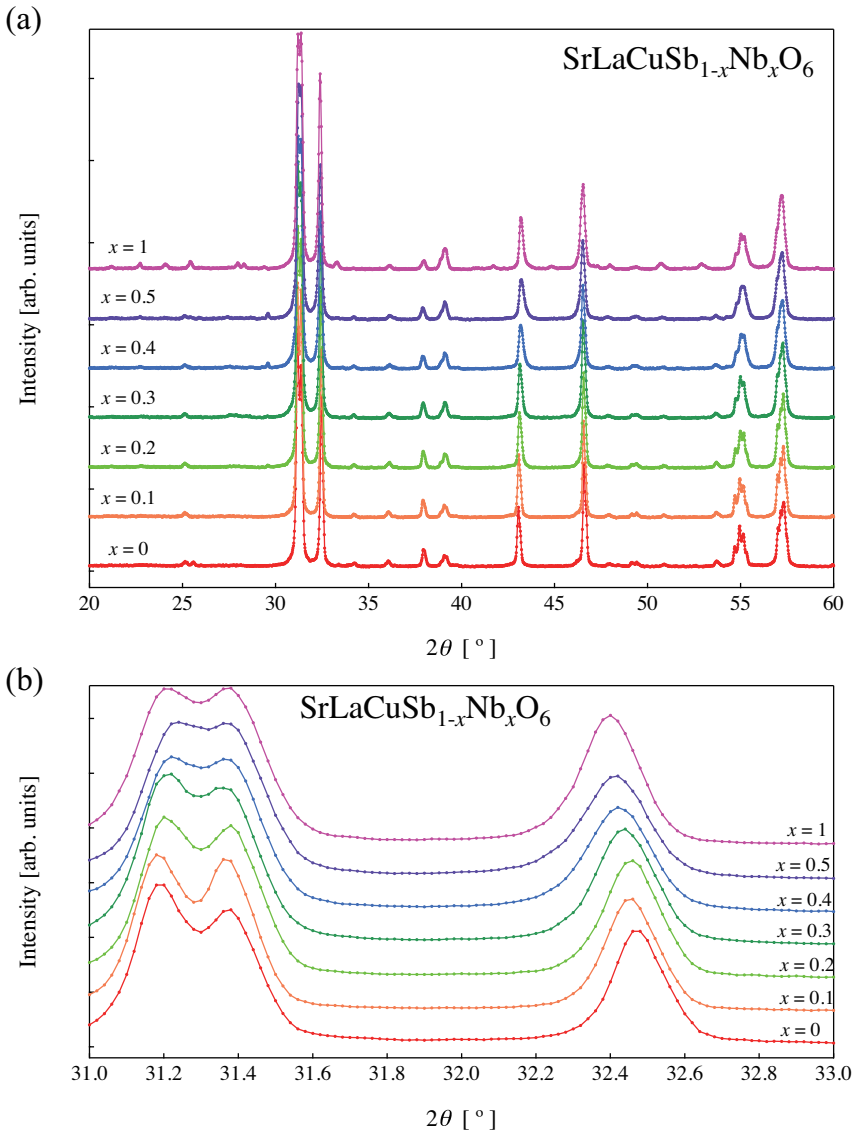

Figure 4.12: (a)X-ray diffraction (XRD) patterns for $SrLaCuSb_{1-x}Nb_xO_6$ with $0 \leq x \leq 0.5$ and $x = 1$. (b) Enlargement of the XRD data between 31.0° and 33.0°.

Rietveld analysis was performed for $SrLaCuSb_{1-x}Nb_xO_6$ with $0 \leq x \leq 0.5$ using RIETAN program [66]. Parent systems $SrLaCuSbO_6$ and $SrLaCuNbO_6$ have $P2_1/n$ and $P\bar{1}$ structures, respectively, as shown in Chap. 3. The present analysis is based on the structural model with space group $P2_1/n$, because the observed XRD patterns for $0 \leq x \leq 0.5$ were successfully reproduced. The obtained structural parameters for $0 \leq x \leq 0.5$ are listed in Table 4.1.

All the CuO_6 octahedra were found to be tetragonally elongated along the c axis due to the Jahn–Teller effect, as observed in parent systems $SrLaCuSbO_6$ and $SrLaCuNbO_6$. Due to the tetragonal distortion of CuO_6 octahedra, the hole orbitals $d(x^2 - y^2)$ of Cu^{2+} ions with $S = 1/2$ are lying in the ab-plane. Hence, the exchange interactions in the ab-plane are expected to be much stronger than those between the ab-plane.

The variation of the lattice constants a, b, and c as a function of the Nb concentration x for $0 \leq x \leq 0.5$ are shown in Figs. 4.13 and 4.14. It is found that the lattice constant c decreases with increasing x in agreement with Vegard's law [136]. The XRD result indicates that Sb and Nb are randomly distributed on the same B''-site, which results in quenched disorder in the J_1 and J_2 interactions between the Cu^{2+} ions. Note that the $P2_1/n$ structure is found to be retained at least up to $x = 0.5$ by the present XRD measurements. Therefore, $SrLaCuSb_{1-x}Nb_xO_6$ is suitable for systematic investigation of the bond randomness effect in $S = 1/2$ $J_1 - J_2$ SLHAFs.

Table 4.1: Rietveld refinement results for $SrLaCuSb_{1-x}Nb_xO_6$.

x	0	0.1	0.2	0.3	0.4	0.5
a (Å)	5.516(4)	5.516(5)	5.519(6)	5.522(9)	5.52(1)	5.53(1)
b (Å)	5.5124(1)	5.5107(2)	5.5123(3)	5.5145(4)	5.5151(6)	5.5178(7)
c (Å)	8.404(2)	8.395(2)	8.390(3)	8.386(4)	8.375(6)	8.370(7)
$c/a\sqrt{2}$	1.0773	1.0762	1.0749	1.0739	1.0722	1.0709
β [°]	90.49(3)	90.48(3)	90.47(4)	90.45(6)	90.44(9)	90.42(3)
V (Å^3)	255.520	255.169	255.226	255.346	255.100	255.223
Sr/La(x,y,z)						
x	0.0075(4)	0.0088(3)	0.0082(4)	0.0070(4)	0.0066(5)	0.0048(5)
y	0.0215(2)	0.0206(2)	0.0203(2)	0.0199(2)	0.00191(3)	0.1778(3)
z	0.2483(6)	02491(6)	0.2482(5)	0.2490(6)	0.2488(7)	0.2491(9)
O(1)(x,y,z)						
x	0.267(3)	0.271(3)	0.273(3)	0.267(3)	0.267(3)	0.264(4)
y	0.280(3)	0.290(2)	0.290(3)	0.282(3)	0.281(3)	0.286(4)
z	0.052(4)	0.035(5)	0.040(5)	0.051(5)	0.053(5)	0.046(6)
O(2)(x,y,z)						
x	0.228(3)	0.227(3)	0.226(3)	0.223(3)	0.215(3)	0.224(4)
y	-0.231(3)	-0.225(3)	-0.227(3)	-0.227(3)	-0.225(3)	-0.227(4)
z	0.000(5)	0.040(4)	0.036(4)	0.031(4)	0.0027(5)	0.033(6)
O(3)(x,y,z)						
x	-0.068(1)	-0.081(1)	-0.079(1)	-0.078(1)	-0.075(2)	-0.079(2)
y	0.487(2)	0.483(2)	0.486(2)	0.487(2)	0.488(2)	0.488(2)
z	0.266(2)	0.266(2)	0.270(2)	0.269(2)	0.269(2)	0.270(3)
$SrSb_2O_6$ (%)	1	0	0	0	0	0.1
$SrNb_2O_6$ (%)	0	0	0	0.1	0.3	0.3
R_{wp} (%)	6.567	6.277	6.090	5.961	6.279	6.574
R_e (%)	5.663	5.777	5.638	5.392	5.444	5.391
$S = R_{wp}/R_e$	1.160	1.087	1.080	1.105	1.153	1.219
R_p (%)	5.186	4.940	4.671	4.456	4.665	4.822

Note that Sr/La is at the (x, y, z), Cu at $(0.5, 0, 0.5)$, Sb/Nb at $(0.5, 0, 0)$, O(1) at (x, y, z), O(2) at (x, y, z), and O(3) at (x, y, z). Isothermal atomic thermal factors (B_{iso}) for the Sr/La, Cu, Sb/Nb, O(1), O(2) and O(3) sites were fixed to 0.69, 0.61, 0.21, 1.0, 0.87, and 0.96, respectively, as obtained by M. P. Attfield *et al.* [114].

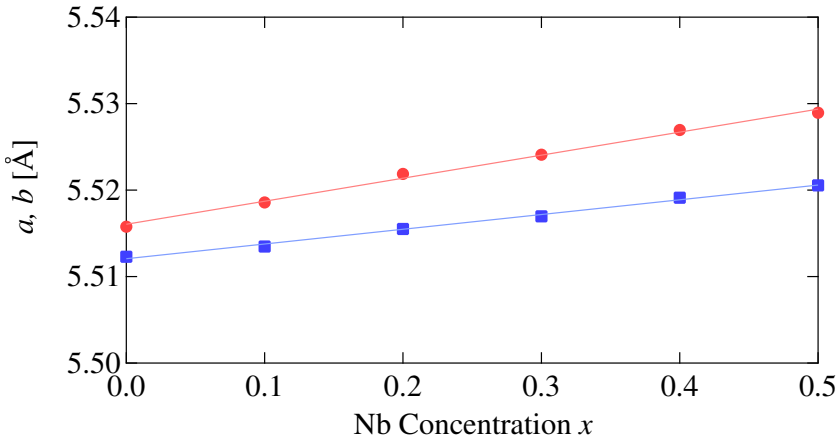

Figure 4.13: Lattice constants a and b for $SrLaCuSb_{1-x}Nb_xO_6$ as a function of the Nb concentration x.

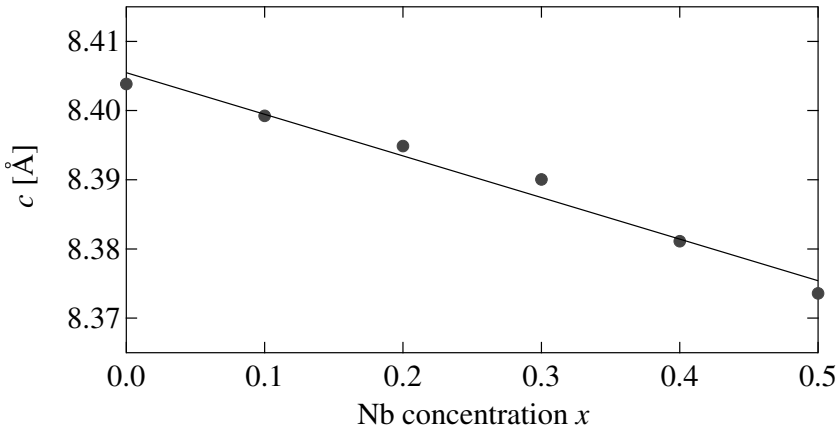

Figure 4.14: Lattice constant c for $SrLaCuSb_{1-x}Nb_xO_6$ as a function of the Nb concentration x.

4.2.2 Magnetic susceptibility

Figure 4.15 (a) shows the temperature variation of the magnetic susceptibilities for $0 \leq x \leq 0.5$ and $x = 1$ measured at $\mu_0 H = 0.1$ T. With decreasing temperature, the susceptibilities display broad maxima at approximately $T_{max} = 40-80$ K as in the cases of parent systems. With further decreasing temperature, the magnetic susceptibilities for the solid solutions ($x \neq 0$ and 1) exhibit a paramagnetic upturn. As the niobium concentration x increases, the upturn is more enhanced, and T_{max} shifts toward the low-temperature side. It is considered

that his upturn of the magnetic susceptibility originates from almost free or weakly coupled spins, which are induced by exchange randomness. Such behavior is a characteristic of the RS state predicted by theoretical calculations [48, 63, 64].

Figure 4.15 (b) shows the field-cooled (FC) and zero-field-cooled (ZFC) magnetic susceptibilities of $x = 0.3$ as a function of temperature below 100 K. Because no significant difference was found between FC and ZFC data, the possibility of a spin-glass ground state is ruled out. Similar behavior was found in other systems with different x except parent compounds with $x = 0$ and 1.

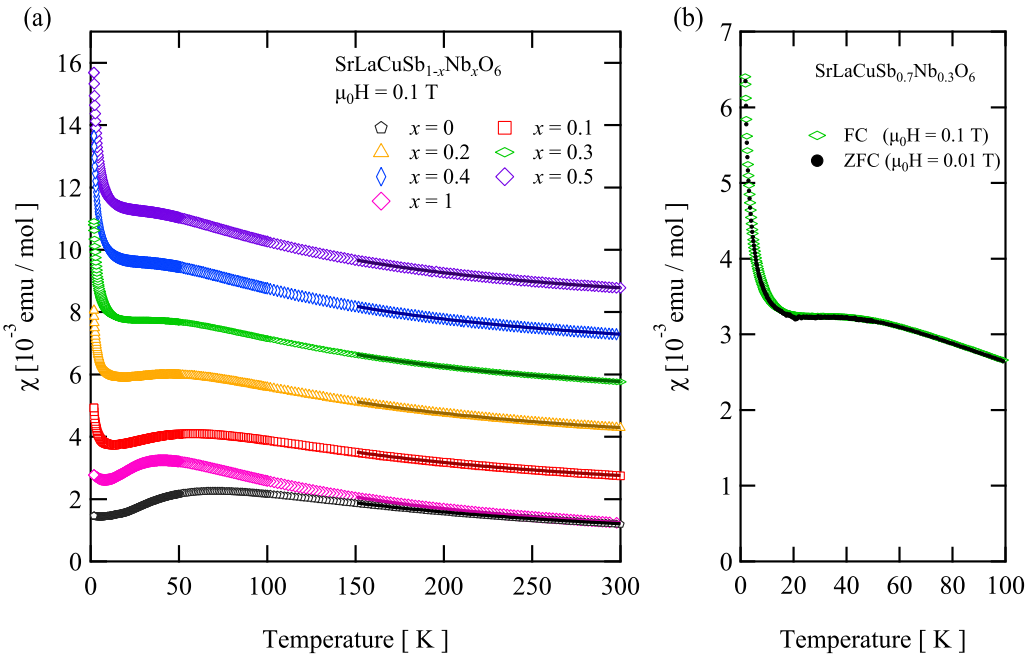

Figure 4.15: (a) Temperature dependence of magnetic susceptibilities of $SrLaCuSb_{1-x}Nb_xO_6$ measured at $\mu_0 H = 0.1$ T for various x. The susceptibility data for $0 \leq x \leq 0.5$ are shifted upward by multiples of 1.5×10^{-3} emu/mol. The solid curves superimposed on the data shows the best fits by the Curie–Weiss law. (b)Temperature dependence of the FC (open symbols) and ZFC (closed symbols) magnetic susceptibilities for the sample with $x = 0.3$.

By analogy with spin-1/2 Heisenberg antiferromagnetic chain and QMC calculations of the spin-1/2 random $J - Q$ model on a square lattice, it has been theoretically predicted that the low-temperature magnetic susceptibility follows a power law $\chi(T) = AT^{-\gamma}$ with $\gamma < 1$ rather than a Curie–Weiss law in the 2D RS state [63, 64]. The low-temperature magnetic susceptibility of $Sr_2CuTe_{1-x}W_xO_6$, which is a promising candidate of spin-1/2 random $J_1 - J_2$

SLHAF, is better fitted by a power law $\chi(T) = AT^{-\gamma}$ with $\gamma \sim 0.7$ rather than the Curie–Weiss law predicted by theoretical studies based on exact diagonalization calculations [48]. As shown in Fig. 4.16 (a), the low-temperature susceptibilities of $SrLaCuSb_{1-x}Nb_xO_6$ with $0.1 < x < 0.5$ were also well reproduced by the power law rather than the Curie–Wiess law. Power law fitting was performed for data in the temperature range between 1.8 K and 3.0 K. As in the case of $Sr_2CuTe_{1-x}W_xO_6$, γ is slightly dependent on x, but the obtained exponent γ is all smaller than 1 regardless of x, as expected for the RS state. γ decreases gradually with increasing x and converges to $\gamma = 0.66$ at $x \sim 0.3$.

In order to investigate how the total of exchange interactions changes by substituting Nb^{5+} for Sb^{5+} in $SrLaCuSb_{1-x}Nb_xO_6$, Curie–Weiss fit was performed in the temperature range $150 - 300$ K. The Curie constant C and the Weiss temperature Θ obtained by fitting the magnetic susceptibilities to the Curie–Weiss law $\chi(T) = C/(T - \Theta)$ are summarized in Figs.4.16 (c) and (d). With increasing x, the Curie constant C decreases continuously and reaches $C \simeq 0.47\,\mathrm{emu\,K\,mol^{-1}}$ at $x \sim 0.3$. Similarly, as x was increased, $|\Theta|$ becomes smaller, so that the total antiferromagnetic interaction becomes weaker. Similarly to x dependence of γ, both C and Θ converge to $C \simeq 0.47\,\mathrm{emu\,K\,mol^{-1}}$ and $\Theta \simeq -68$ K at $x \sim 0.3$, which are close to those for the parent material $SrLaCuNbO_6$.

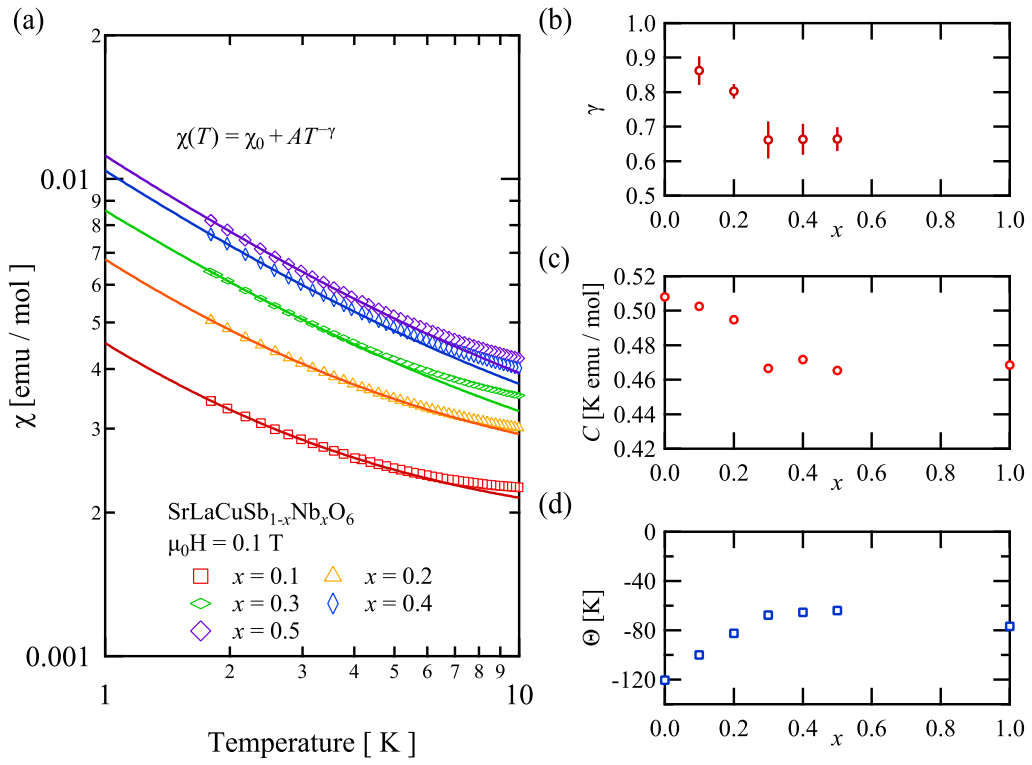

Figure 4.16: (a) Low-temperature magnetic susceptibilities of $SrLaCuSb_{1-x}Nb_xO_6$ with $0.1 \leq x \leq 0.5$ measured at $\mu_0 H = 0.1$ T. The solid curves are the fits by the power-law $\chi(T) = \chi_0 + AT^{-\gamma}$ below 3 K. (b) γ obtained by the fits. (c) and (d) The Curie constant C and the Weiss constant Θ, respectively, obtained by the Curie–Weiss fits for magnetic susceptibilities in the temperature range $150 - 300$ K.

4.2.3 Magnetization process

Figure 4.17 shows field dependence of magnetization M of polycrystalline $SrLaCuSb_{1-x}Nb_xO_6$ with $0 \leq x \leq 0.5$ and $x = 1$ measured at $T = 1.8$ K. For the $x \neq 0$ and 1, the anomaly due to the spin-flop transition observed at $H_s = 1.4$ T for $x = 0$ is suppressed. In the low magnetic field region, the magnetization process has a curvature similar to a Brillouin-function, indicative of a paramagnetic component. This is consistent with the low-temperature susceptibility $\chi(T)$ shown in Fig. 4.15 (a). In high magnetic field region, magnetization is nearly proportional to the field H. These observations for $SrLaCuSb_{1-x}Nb_xO_6$ with $x \neq 0$ and 1 are consistent with the low-temperature properties related to the RS state for the $S = 1/2$ random $J_1 - J_2$ SLHAF [48]. These magnetic properties are quite similar to those observed in $Sr_2CuTe_{1-x}W_xO_6$ [109, 137].

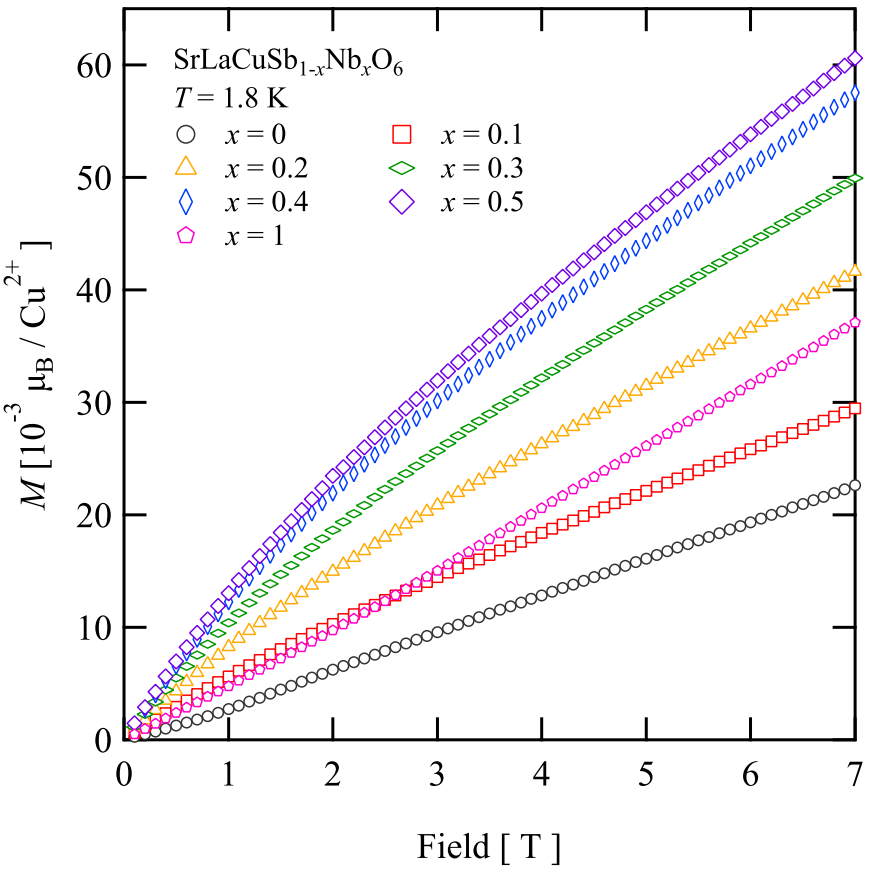

Figure 4.17: Magnetic field dependence of Magnetization of $SrLaCuSb_{1-x}Nb_xO_6$ measured at $T = 1.8$ K for various x.

4.2.4 Specific heat

Figure 4.18 shows the temperature dependence of the specific heat $C(T)$ divided by temperature T for $0 \leq x \leq 0.5$, and 1 measured at zero magnetic field for $T < 10\,\mathrm{K}$. The partial substitution of Nb^{5+} for Sb^{5+} produces a significant change in the low-temperature specific heat. In the parent compounds, which are in the magnetically ordered state for $T < 10\,\mathrm{K}$, the low-temperature specific heat decreases obeying $C(T)/T \sim T$ toward zero. A small increase in $C(T)/T$ below 0.5 K is ascribed to the nuclear specific heat $C_\mathrm{n}(T)$. In contrast to the specific heat of the parent compounds, the low-temperature specific heat for $x \neq 0$ and 1 is much larger than those of the parent compounds, suggesting that the density of the low-energy state is increasing due to bond randomness. The $C(T)/T$ above 2 K tend to reach a constant indicative of the T-linear term in specific heat predicted by Uematsu and Kawamura [48]. However, as the temperature is further decreased from 2 K, the $C(T)/T$ begins to decrease, resulting in a shoulder anomaly in $C(T)/T$ accompanied with a broad maximum at $T^* = 0.55\,\mathrm{K}$. This behavior is not in agreement with the theory by Uematsu and Kawamura [48]. It is also worth noting that T^* is almost independent of x, although the magnitude of the mean antiferromagnetic interaction decreases with increasing x.

To clarify the nature of the broad peak at T^*, specific heat measurements were performed in magnetic fields H up to 9 T. Figure 4.19 (a) and (d) show representative plots of $C(H,T)/T$ for $x = 0.1$ and 0.5, respectively (See Figure 4.21 for all data).

The broad maximum in C/T observed at zero magnetic field is partly suppressed in applied magnetic fields. The broad peak completely disappears in magnetic fields above 6 T, and C/T is almost independent of the magnetic field above 6 T except for the nuclear specific heat C_n below 0.5 K. Thus, it is natural to deduce that the difference between the values of C/T at $\mu_0 H = 0$ and 9 T below 10 K originates from the Schottky specific heat $C_\mathrm{dimer}(T,H)$ due to the Zeeman splitting of loosely coupled spin pairs and the nuclear specific heat $C_\mathrm{n}(T,H)$. Hence, the total specific heat $C(T,H)$ composed of four contributions; (a) field-independent lattice contribution $C_\mathrm{L}(T)$, (b) field-independent magnetic contribution $C_\mathrm{mag}(T)$, (c) field-dependent magnetic contribution $C_\mathrm{dimer}(T,H)$, and (d) field-dependent nuclear spin contribution $C_\mathrm{n}(T,H)$.

Figures 4.19 (b) and (e) show difference $\Delta C(T,H)/T$ between $C(T,0\,\mathrm{T})/T$ and $C(T,H)/T$ with $H = 3$, 6, and 9 T for $x = 0.2$ and $x = 0.5$, respectively.

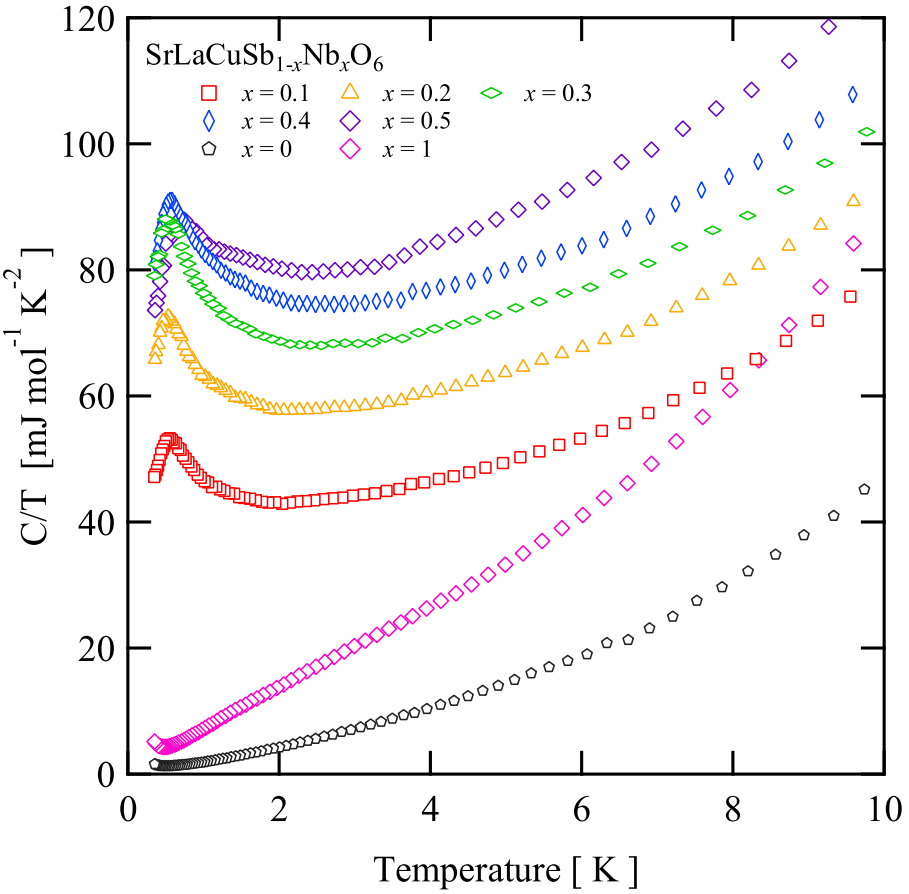

Figure 4.18: Temperature dependence of the specific heat divided by the temperature C/T for $SrLaCuSb_{1-x}Nb_xO_6$ powders measured at zero field for $0 \leq x \leq 0.5$, and $x = 1$.

With increasing temperature from 0.35 K, $\Delta C(T,H)/T$ exhibited a rounded maximum at $0.5 - 0.7$ K and then decreases to be negative. This is a typical characteristic of Schottky specific heat due to the Zeeman splitting. Specific heat of spin pairs coupled via exchange interaction J in magnetic field is expressed as

$$C'_{\mathrm{dimer}}(T,H,J) = \frac{nN_{\mathrm{A}}\beta}{2T}\frac{2\left\{\left(J^2+(g\mu_{\mathrm{B}}H)^2\right)e^{\beta J}+(g\mu_{\mathrm{B}}H)^2\right\}\cosh\left(\beta g\mu_{\mathrm{B}}H\right)-4Jg\mu_{\mathrm{B}}He^{\beta J}\sinh\left(\beta g\mu_{\mathrm{B}}H\right)+4(g\mu_{\mathrm{B}}H)^2+J^2e^{\beta J}}{\left(1+e^{\beta J}+2\cosh(\beta g\mu_{\mathrm{B}}H)\right)^2}, \tag{4.5}$$

where N_{A} is the Avogadro's number and n is the fraction of the spins that are loosely coupled to form spin pairs. If the exchange interaction J is rectangularly distributed from $J - \Delta J$ to $J + \Delta J$, the specific heat of the loosely

coupled spins in a magnetic field is expressed as

$$C_{\mathrm{dimer}}(T,H,J,\Delta J)=\int_{J-\Delta J}^{J+\Delta J}\frac{C'_{\mathrm{dimer}}(T,H,J)\Theta(J-\Delta J)\cdot\Theta(J+\Delta J)}{2\Delta J}dJ, \tag{4.6}$$

where Θ is a step function.

To estimate the amount of weakly coupled spins n and coupling constants J, and the half-width ΔJ of the distribution of J, $\Delta C(T,H)/T$ at $H=3$, 6,and 9 T were fitted simultaneously by

$$\frac{\Delta C(T,H)}{T}=\frac{C_{\mathrm{dimer}}(T,H=0\,\mathrm{T},J,\Delta J)}{T}-\frac{C_{\mathrm{dimer}}(T,H,J,\Delta J)}{T}-\frac{A_{\mathrm{n}}H^2}{T^3}, \tag{4.7}$$

where the last term with coefficient A_{n} represents nuclear specific heat in magnetic fields H. g-factor was fixed to be $g=2.2$. The solid lines in Fig. 4.19 (b) and (e) are calculated results using Eq. (4.7) with parameters listed in Table. 4.2. Experimental results of $\Delta C/T$ are well described in terms of the Schottky specific heat due to the Zeeman splitting of loosely coupled spin pairs and nuclear specific heat. Calculated $C_{\mathrm{dimer}}(T,H)/T$ with parameters given by the best fit are also displayed in Fig. 4.19 (a) and (d), which described well the change of the broad peak position with increasing magnetic fields. For all x, the fitting was reasonably performed, and the results of the fitting are shown in Fig. 4.22.

The specific heat of $SrLaCuSb_{1-x}Nb_xO_6$ with $0.1 \leq x \leq 0.5$ exhibits no significant sign of magnetic ordering, suggesting that quantum disordered ground state (QDGS) is realized in these mixed systems. However, the nature of the QDGS is unclear. Next, we discuss the nature of the QDGS observed in $SrLaCuSb_{1-x}Nb_xO_6$ on the basis of the analysis of the field-independent contribution of specific heat $C_{\mathrm{mag}}(T)$.

In the theoretical analysis of $S=1/2$ random J_1-J_2 SLHAF using exact diagonalization, T-linear specific heat was observed for the QDGS, which is considered to be the RS state [48]. On the other hand, the analysis of the $S=1/2$ random $J-Q$ model on a square lattice suggested that magnetic susceptibility $\chi(T)$ and specific heat divided by temperature $C(T)/T$ follow a power law $\chi(T)\propto T^{-\gamma}$ and $C(T)/T\propto T^{-\gamma}$ with the same exponent $\gamma<1$, respectively [63, 64]. In the previous experiment, the low-temperature magnetic susceptibility of $Sr_2CuTe_{1-x}W_xO_6$, which is a promising candidate for the RS

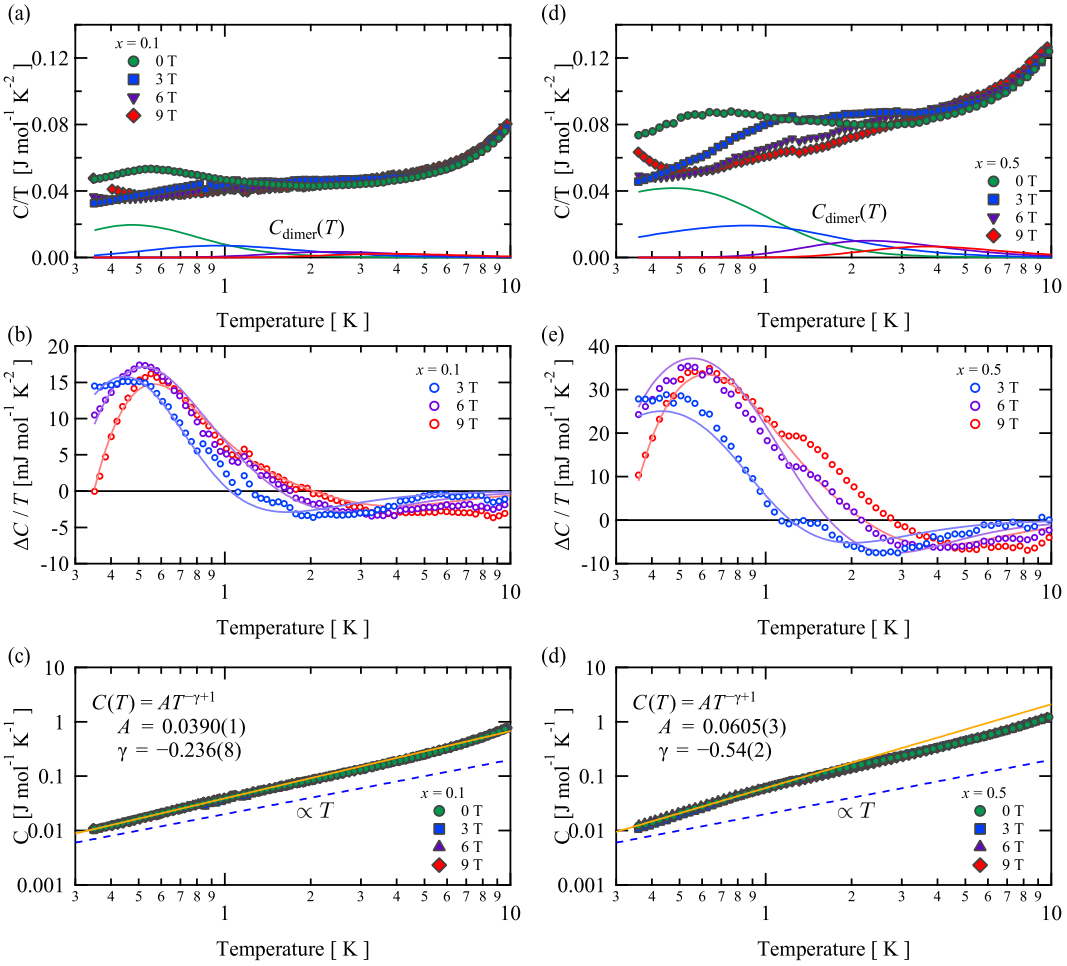

Figure 4.19: (a) and (d) C/T for $x = 0.1$ and 0.5 as a function of temperature measured in 0, 3, 6, and 9 T. The solid curves are the $C_{\rm dimer}/T$ calculated using the parameters listed in Table 4.2. (b) and (d) $\Delta C/T$ for $x = 0.1$ and 0.5 as a function of temperature in 3, 6, and 9 T. The solid curves are fits by Eq. 4.7. (c) and (f) Corrected specific heat $C'(T) = C(T) - (C_{\rm dimer} + C_{\rm n})$ at $H = 0$, 3, 6, and 9 T for $x = 0.1$ and 0.5, respectively. The solid lines are results of a power law $C'(T) = AT^{-\gamma+1}$.

state, could be fitted by the power law with $\gamma \approx 0.7$ [64]. However, the specific heat was not reproduced by a power law with γ obtained from the fit of the magnetic susceptibility. The analysis of the $C(T)$ of $Sr_2CuTe_{1-x}W_xO_6$ resulted in $\gamma < 0$, which is inconsistent with the theoretical result [48, 63, 64].

Figures 4.19 (c) and (f) show corrected specific heat $C'(T)$ defined by $C'(T) = C(T) - (C_{\rm dimer} + C_{\rm n})$ at $H = 0$, 3, 6, and 9 T for $x = 0.1$ and 0.5, respectively. $C'(T)$ for all magnetic fields coincides each other. In the log-log plot, $C'(T)$ shows a linear behavior insensitive to applied magnetic fields, suggesting that the low-energy excitation from the QDGS in $SrLaCuSb_{1-x}Nb_xO_6$ is gapless. In the low-temperature range below 1 K, the lattice contribution to

total specific heat is almost negligible, resulting in $C'(T) \simeq C_{\rm mag}(T)$. Therefore, collected $C'(T)$ data was fitted by a power law $C'(T) = AT^{-\gamma+1}$ in the temperature range below 1 K. The solid lines in Figs. 4.19 (c) and (f) represent calculated results based on $C'(T) = AT^{-\gamma+1}$ with the best fit parameters. Remarkably, for $0.1 \leq x \leq 0.3$, the fits are in agreement with the experimental results up to higher temperatures than the temperature range for the fit.

Figures 4.20 (a) and (b) show A and γ as a function of x. $\gamma(x) < 0$ was obtained, irrespective of x, which is inconsistent with the theoretical prediction for the RS state, as in the case of $Sr_2CuTe_{1-x}W_xO_6$. The $\gamma(x)$ is almost constant for $0.1 \leq x \leq 0.3$, whereas for $x > 0.3$, the magnitude of $\gamma(x)$ is enhanced with increasing x. The results of the $C'(T)$ analysis for all x are shown in Figure 4.23.

Table 4.2: The parameters obtained from the analysis of $\Delta C/T$ for $SrLaCuSb_{1-x}Nb_xO_6$ with $0.1 < x < 0.5$. The g-factor is fixed to $g = 2.2$.

x	0.1	0.2	0.3	0.4	0.5
$n \times 10^3$	2.75(7)	4.5(1)	6.4(2)	7.9(3)	8.1(4)
$J/k_{\rm B}$ [K]	1.78(2)	1.84(2)	1.95(2)	2.02(3)	2.11(3)
$\Delta J/k_{\rm B}$ [K]	0.58(8)	0.90(7)	1.01(8)	1.19(7)	1.27(9)
$A_n \times 10^3$	8.5(5)	9.4(8)	10.7(1)	14.4(1)	17.4(2)

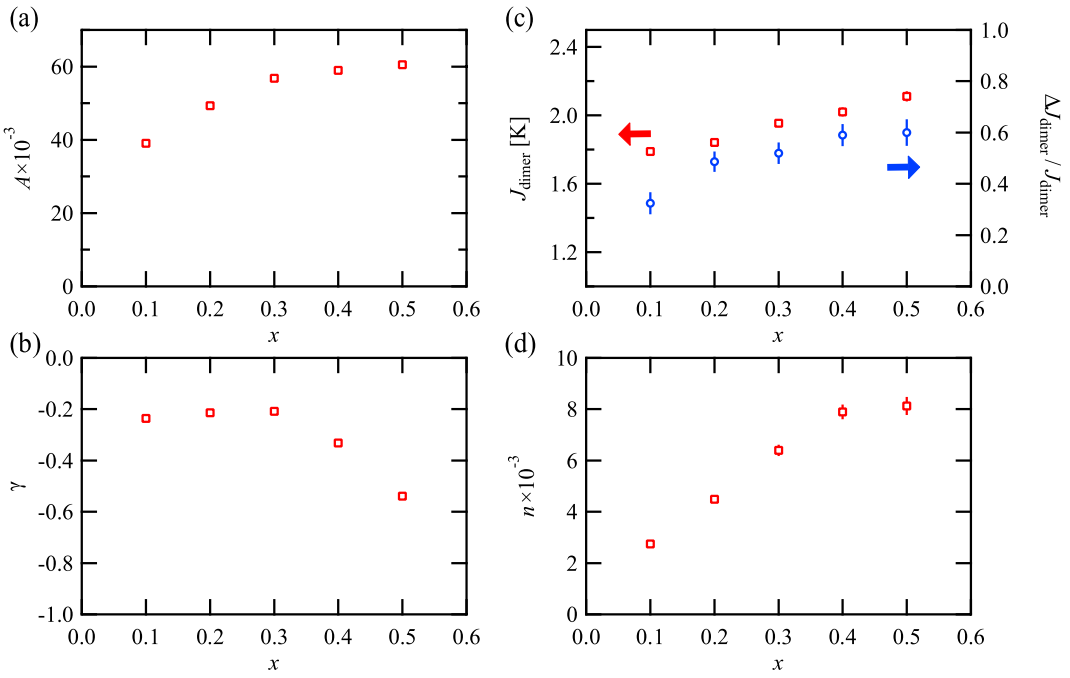

Figure 4.20: Summary of the x dependence of parameters obtained by fits of the specific heat in $SrLaCuSb_{1-x}Nb_xO_6$. (a) the coefficients A, (b) the exponent γ, (c) the exchange interaction of weakly coupled spin pairs $J_{\rm dimer}$ and the fraction of half-width ΔJ to $J_{\rm dimer}$, and (d) the number of spins displaying Schottky specific heat $C_{\rm dimer}$.

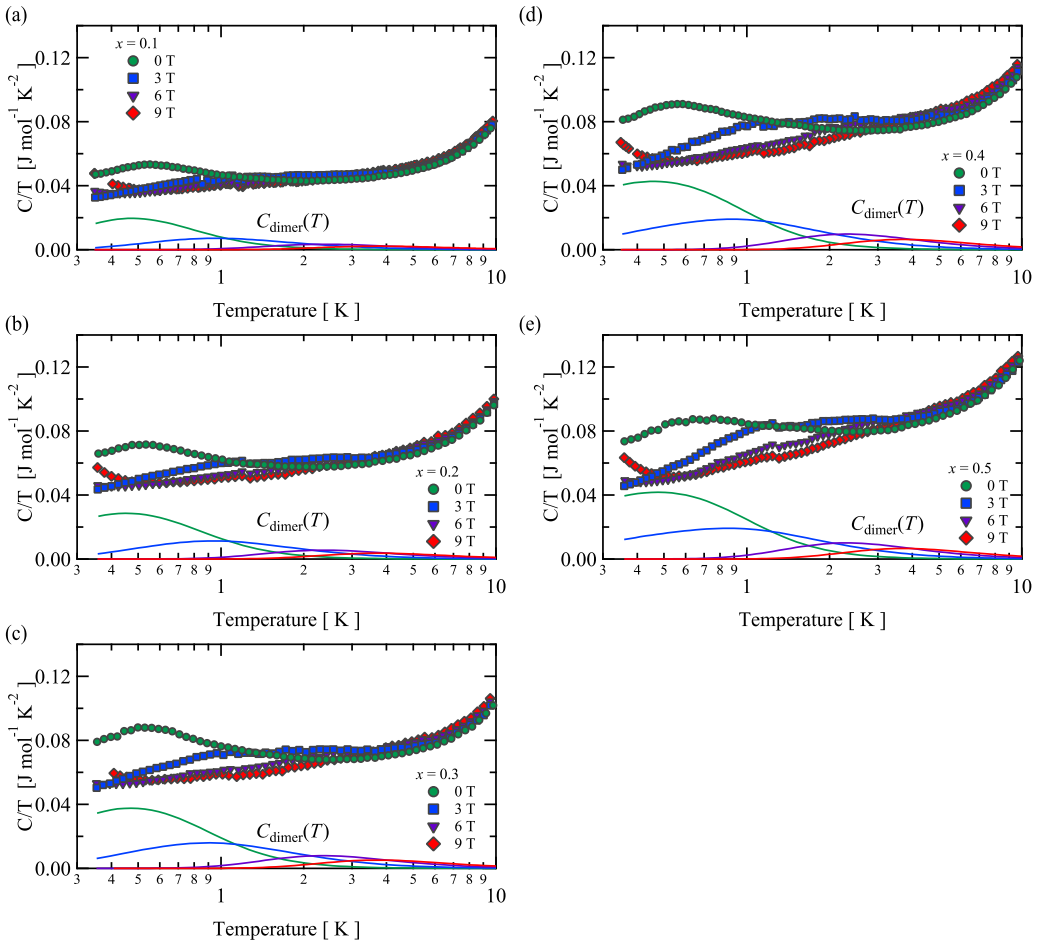

Figure 4.21: (a)-(e) C/T for $x = 0.1$, 0.2, 0.3, 0.4 and 0.5 as a function of temperature measured in 0, 3, 6, and 9 T. The solid curves are the $C_{\rm dimer}/T$ calculated using the parameters listed in Table 4.2.

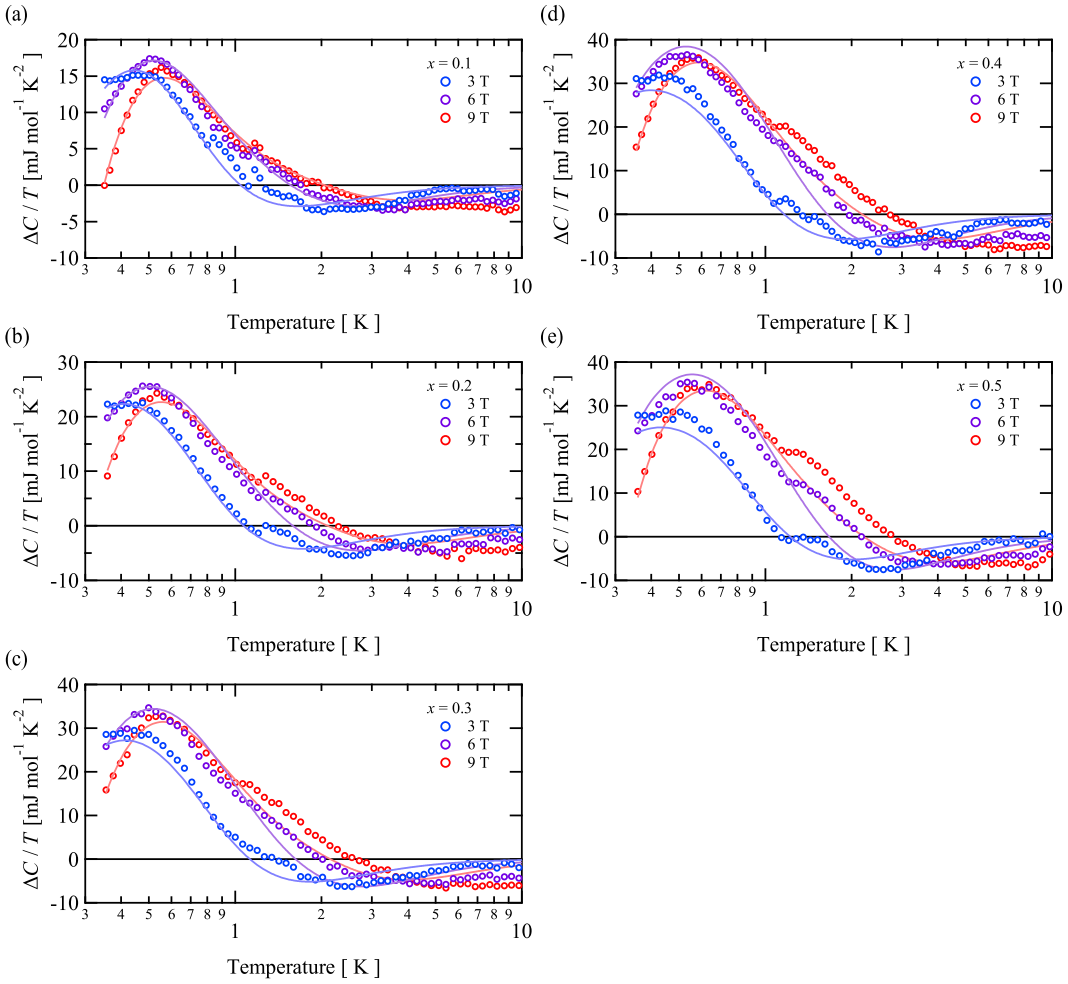

Figure 4.22: (a)-(e) $\Delta C/T$ for $x = 0.1$, 0.2, 0.3, 0.4 and 0.5 as a function of temperature in 3, 6, and 9 T. The solid curves are fits by Eq. 4.7.

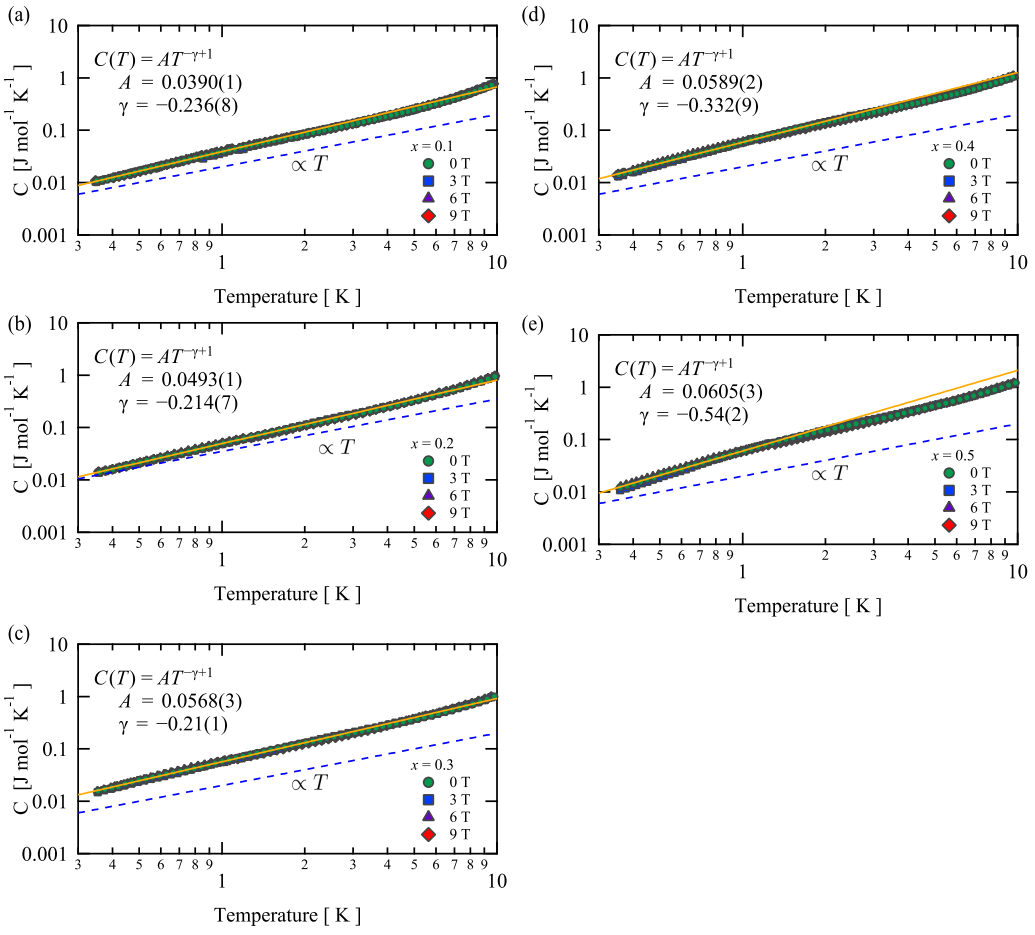

Figure 4.23: (a)-(e) Corrected specific heat $C'(T) = C(T) - (C_{\rm dimer} + C_{\rm n})$ at $H = 0$, 3, 6, and 9 T for $x = 0.1$, 0.2, 0.3, 0.4, and 0.5, respectively. The solid lines are results of a power law $C'(T) = AT^{-\gamma+1}$. The dashed lines show $C'(T) \propto T$.

4.2.5 Muon spin rotation and relaxation

No sign of magnetic ordering was observed in the specific heat measurements of $SrLaCuSb_{1-x}Nb_xO_6$. Furthermore, the magnetic specific heat at low temperatures follows a power law, suggesting that the ground state is a gapless QDGS. On the other hand, the temperature dependence of the total specific heat divided by temperature, $C(T)/T$, showed a broad peak at $T^* = 0.55\,\mathrm{K}$ at zero magnetic field. From the specific heat measurements in magnetic fields of up to 9 T, it was suggested that the peak at $T^* = 0.55\,\mathrm{K}$ is originated from the Schottky specific heat due to a loosely coupled spin pairs. However, the existence of magnetic order cannot be completely ruled out by bulk measurements only. Therefore, I measured μSR at MLF, J-PARC, which is highly sensitive to the local magnetic field. The μSR experiments were performed on a sample $SrLaCuSb_{0.8}Nb_{0.2}O_6$ in the temperature range from 30 K to 0.035 K using a dilution refrigerator.

TF-μSR

Figure 4.24 show the μSR time spectra of $SrLaCuSb_{0.8}Nb_{0.2}O_6$ measured at 30 K, 4 K, and 0.035 K by applying a transverse field of 2 mT. No loss of initial asymmetry $A_{\mathrm{tot}}(t = 0)$ and no upward shift of rotational signals were found down to 0.035 K. This results rule out a presence of static internal fields due to magnetic ordering and or spin-freezing in $SrLaCuSb_{0.8}Nb_{0.2}O_6$. If magnetic ordering occurs, as observed in the TF μSR measurements of $SrLaCuSbO_6$ and $SrLaCuNbO_6$, the 2/3 component of the muon spin polarization perpendicular to the internal magnetic field will be lost, while the residual 1/3 component will be observed as the upward shift.

Relaxational and rotational signals were found even at the lowest temperature $T = 0.035\,\mathrm{K}$. It is considered that this muon spin relaxation is attributed to the very slow fluctuating spins. These TF-μSR spectra are similar to those observed in $Sr_2CuTe_{1-x}W_xO_6$[119], which is promising candidate for $S = 1/2$ random J_1-J_2 SLHAF, and QSL candidate materials.

A_{tot} was determined by fitting the data measured at 30 K, which is sufficiently higher than T^*, with the following equation

$$A(t) = A_{\mathrm{tot}} \exp\left(-(\lambda t)^{\beta}\right) \cos(2\pi\nu t + \phi). \tag{4.8}$$

The TF-μSR spectrum at the lowest temperature shows a rotating signal with a constant amplitude in the range over 10 μs. This is originated from the muon

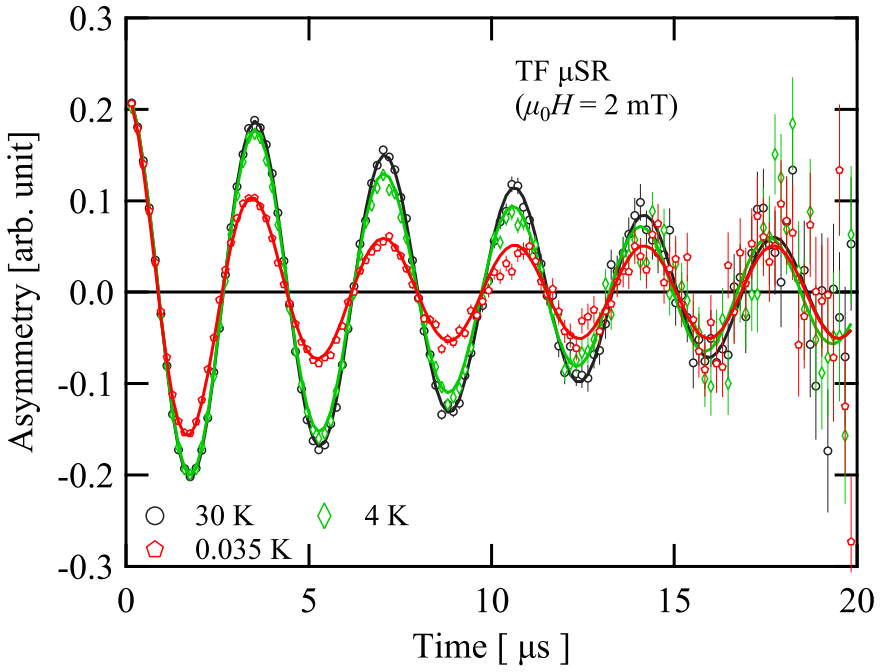

Figure 4.24: TF μSR spectra of $SrLaCuSb_{0.8}Nb_{0.2}O_6$ measured with a 2 mT transverse field at 30 K, 4 K, and 0.035 K. The black solid curve was the result of fitting the TF-muSR spectrum measured at 30 K with Eq. 4.8. The green and red solid curves were the result of fitting the TF-muSR spectrum measured at 4 K and 0.035 K with Eq. 4.9, respectively.

implanted in the silver sample holder. Since silver has a very small nuclear moment, the muon implanted in the silver is affected only by the applied transverse field. Hence, the background $A_{\rm BG}$ was estimated by evaluating the fraction of the rotational component with a constant amplitude. As shown in Fig. 4.24, the TF spectrum at the lowest temperature was reproduced by the following equation;

$$A(t) = A_{\rm BG}\cos\left(\omega_1 t + \phi\right) + A_{\rm c}\exp\left(-(\lambda t)^{\beta}\right)\cos\left(\omega_1 t + \phi\right) \qquad (4.9)$$

$A_{\rm BG}/A_{\rm tot} = 0.235$ was obtained by fitting the TF-spectrum at 0.035 K using Eq. 4.9. This value is consistent with the experimental results using the same instrument [138].

ZF-μSR

Figure 4.25 show representative spectra measured in a zero magnetic field for $SrLaCuSb_{0.8}Nb_{0.2}O_6$. The temperature range of the measurement is from 0.035 K to 30 K. Even at 0.035 K, no sign for the magnetically ordered state was found in ZF-μSR spectra of $SrLaCuSb_{0.8}Nb_{0.2}O_6$ in contrast to its parent compounds. In the ZF-μSR measurement of the parent material with very weak bond randomness, it was found that the initial asymmetry was lost and the 1/3-tail was recovered. However, for $SrLaCuSb_{0.8}Nb_{0.2}O_6$, the initial asymmetry was preserved down to the lowest temperature 0.035 K, the relaxation went toward the background line, and the 1/3 tail was not recovered. These results completely rule out both magnetic ordering and spin freezing in $SrLaCuSb_{0.8}Nb_{0.2}O_6$.

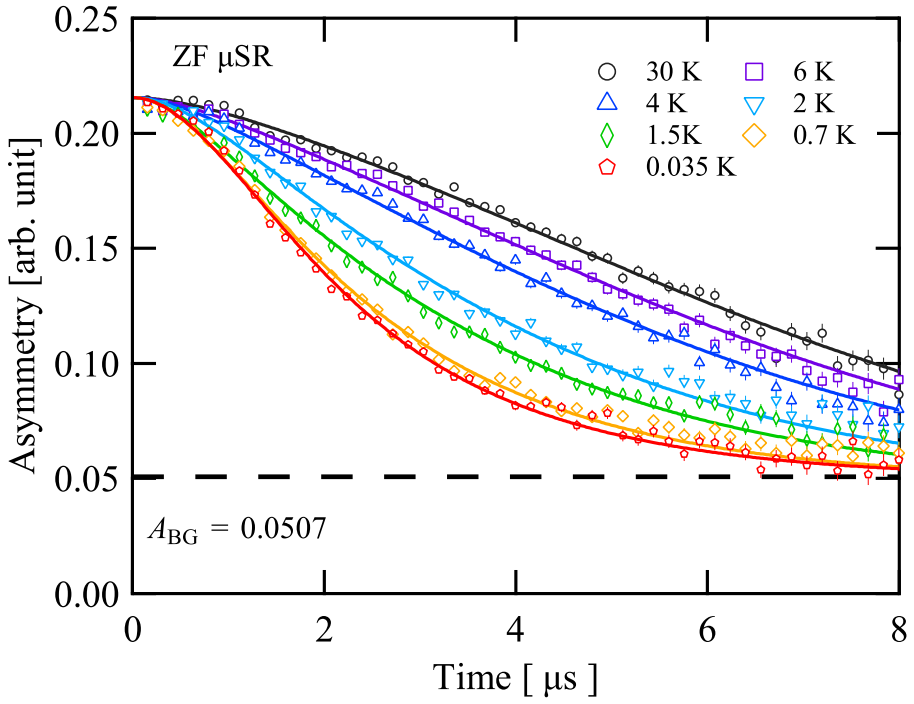

Figure 4.25: ZF-μSR spectra of $SrLaCuSb_{0.8}Nb_{0.2}O_6$ measured at various temperatures. Solid curves are results of fitting ZF-μSR spectra by Eq. 4.14.

Focusing on the $0-2$ μs range in ZF-μSR spectra, relaxation curves seemed to be Gaussian rather than Lorentzian. Thus, to obtain a quantitative description of the ZF-μSR spectra, the dynamical Gaussian Kubo–Toyabe function $G_{\mathrm{dKT}}(t;\Delta,\nu,H_{\mathrm{LF}})$ was used to analyze the spectra. The dynamical Gaussian Kubo–Toyabe function $G_{\mathrm{dKT}}(t;\Delta,\nu,H_{\mathrm{LF}})$ accounts for a spin relaxation in zero field and longitudinal field H_{LF} due to a Gaussian distribution of internal fields

of width Δ fluctuating at the rate ν [139–141]. $G_{\rm dKT}(t;\nu,\Delta)$ is described as

$$G_{dKT}(t;\Delta,\nu,H_{\rm LF}) = \frac{1}{2\pi i}\int_{\gamma+i\infty}^{\gamma-i\infty} \frac{f_{\rm G}(s+\nu)}{1-\nu f_{\rm G}(s+\nu)}\exp(st)ds, \tag{4.10}$$

$$f_{\rm G}(s) = \int_0^\infty G_{\rm G}^{\rm LF}(t)\exp(-st)dt, \tag{4.11}$$

$$\tag{4.12}$$

where $G_{\rm G}^{\rm LF}(t)$ is the static Gaussian Kubo–Toyabe function for the presence of longitudinal fields;

$$\begin{aligned} G_{\rm G}^{\rm LF}(t) = 1 - \frac{2\sigma^2}{(2\pi\Gamma)^2}\left[1-\exp\left(-\frac{1}{2}\sigma^2t^2\right)\cos(2\pi\Gamma t)\right] \\ +\frac{2\sigma^4}{(2\pi\Gamma)^3}\int_0^t \exp\left(-\frac{1}{2}\sigma^2\tau^2\right)\sigma(2\pi\Gamma\tau)d\tau, \end{aligned} \tag{4.13}$$

where $\sigma = \frac{\gamma_\mu}{2\pi}\Delta$ is a relaxation rate due to a Gaussian distribution of internal fields of width Δ and $\Gamma = \frac{\gamma_\mu}{2\pi}H_{\rm LF}$ is a frequency corresponding to applied longitudinal fields $H_{\rm LF}$.

The ZF spectra measured at all temperatures below 30 K can be fitted with the following equation, systematically;

$$A_{\rm tot}(t) = A_0 G_{\rm KT}(t;\Delta_{\rm n})G_{\rm dKT}(t;\Delta,\nu) + A_{\rm BG}, \tag{4.14}$$

where $G_{\rm KT}$ is zero field static Kubo–Toyabe function describing a Gaussian distribution of internal fields of width $\Delta_{\rm n}$ induced by nuclear spins. Throughout all analyses on the ZF spectra, $A_{\rm BG}$ was fixed to the value estimated in the TF-μSR experiment, and $\Delta_{\rm n}$ is also fixed to the value estimated from the ZF-muSR spectra at 30 K. The temperature dependence of Δ and ν obtained by the fit are shown in Figs. 4.26 and 4.27 as a function of temperatures, respectively. The solid curves in Fig. 4.25 were the results calculated with the best-fit parameters.

In the previous μSR experiments on $Sr_2CuTe_{1-x}W_xO_6$[119], the phenomenological stretched exponential decay $A(t) = A_0\exp(-(\lambda t)^\beta)$ was used to analyze ZF/LF-μSR spectra. λ in stretched exponential decay is associated with the width Δ of the internal magnetic fields as $\lambda \sim \frac{\gamma_\mu}{2\pi}\Delta$. As shown in Fig. 4.26, Δ saturated to a constant value with decreasing temperature, which indicates that spins are slowly fluctuating even at the lowest temperature 0.035 K. This behavior is characteristic of QDGSs such as QSLs. The fluctuating rate of internal magnetic fields, ν, also decreases to a constant value with decreasing

temperature. There are several possible scenarios for the fluctuation of the internal magnetic field. The most typical case is that the muons themselves are hopping or diffusing in the sample, as observed in high-purity copper [142, 143]. Since the mass of a muon is about 1/9 times that of a proton, hopping due to thermal fluctuations or quantum diffusion due to tunneling effects are possible to occur. However, in the μSR experiments of the parent materials $SrLaCuSbO_6$ and $SrLaCuSbO_6$, no dynamic internal magnetic field suggestive of the muon hopping and diffusing was observed. On the other hand, the most exotic case is that itinerant quasiparticles such as deconfined spinons run through a sea of singlets and pass by the muon, resulting in fluctuations of internal magnetic fields. Inelastic neutron scattering experiments on single crystals of $SrLaCuSb_{0.8}Nb_{0.2}O_6$ are needed to conclude whether or not exotic quasiparticle excitations such as spinons exist.

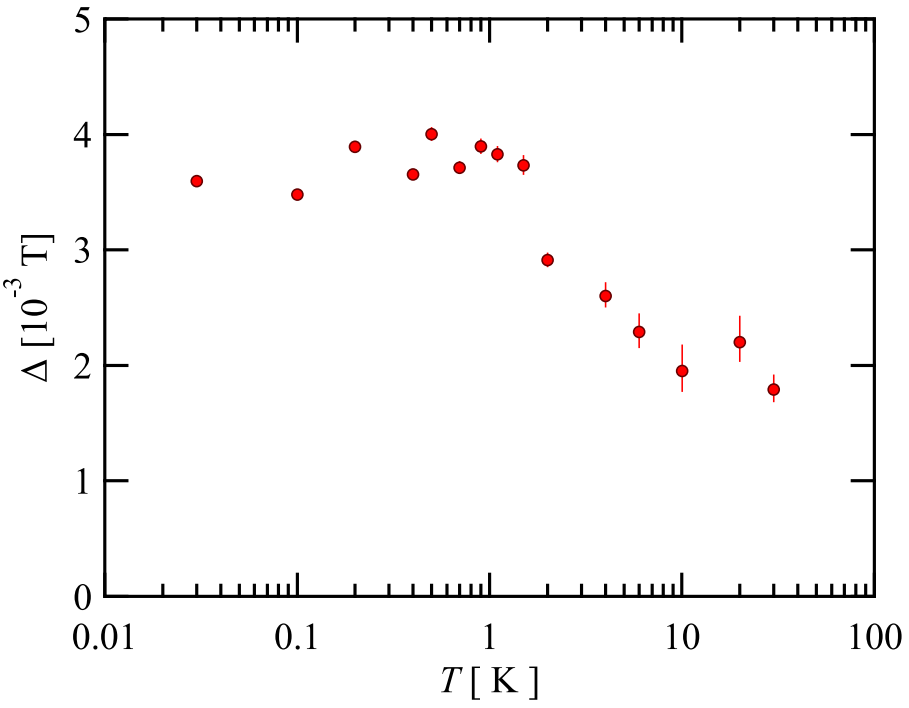

Figure 4.26: Temperature dependence of the internal field distribution width Δ.

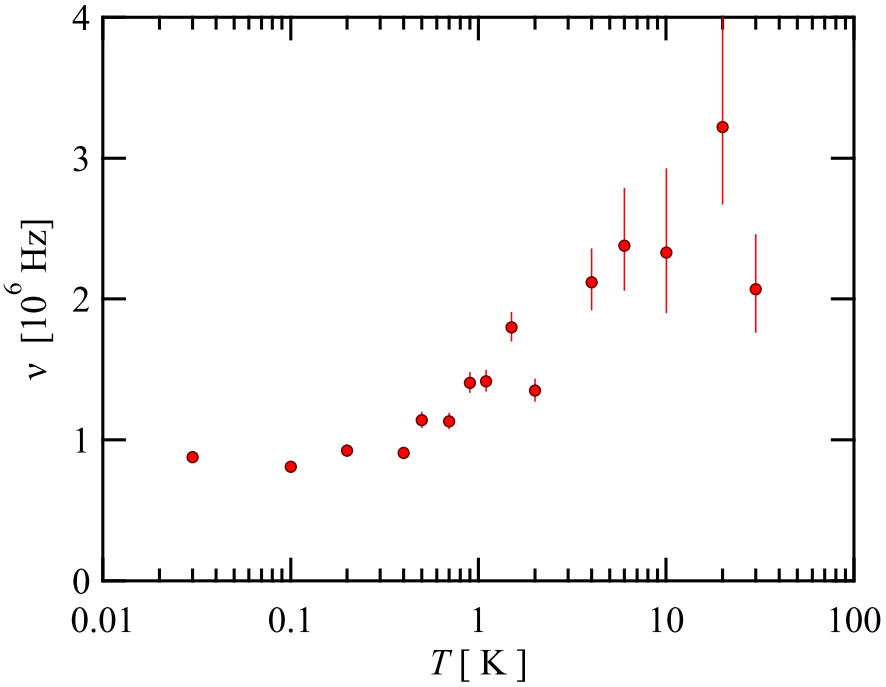

Figure 4.27: Fluctuating rate $\nu(T)$ as a function of temperature.

LF-μSR

To further investigate the dynamic nature of the internal magnetic field, LF-μSR measurements were carried out at the lowest temperature 0.035 K. From the value of $\Delta(T)$ estimated from ZF-μSR at the lowest temperature, the muon spin will be decoupled from the internal magnetic field by applying a longitudinal field of $5\Delta \sim 20$ mT, if the internal magnetic field is entirely static. However, as shown in Fig. 4.28, even 300 mT is not enough to decouple the muon spin completely from the internal magnetic fields, which indicate that the muon spin relaxation at the lowest temperature is due to the dynamic internal magnetic field. The spectrum below 10 mT is slightly oscillatory, which could reflect the characteristics of the dynamical Gaussian Kubo–Toyabe function $G_{\rm dKT}(t;\Delta,\nu,H_{\rm LF})$. However, not all the field dependence can be reproduced by $G_{\rm dKT}(t;\Delta,\nu,H_{\rm LF})$ only.

All LF-μSR spectra can be fitted simultaneously with the following equation;

$$A_{\rm tot}(t) = A_0 G_{\rm KT}^{\rm LF}(t;\Delta_n,H_{\rm LF}) G_{\rm dKT}(t;\Delta,\nu,H_{\rm LF}) \exp(-(\lambda_{\rm LF}t)^{\beta}) + A_{\rm BG}^{\rm LF}, \quad (4.15)$$

where $G_{\rm KT}^{\rm LF}(t;\Delta_n,H_{\rm LF})$ represents static LF Gaussian Kubo–Toyabe function describing nuclear spin contribution and $A_{\rm BG}^{\rm LF}$ is the background in the setup of the longitudinal field measurement. This means that the muon spin feels the convolution of two internal magnetic fields, one corresponding to the relaxation described by the dynamical Gaussian Kubo-Toriyabe function $G_{\rm dKT}(t;\Delta_n,H_{\rm LF})$ and the other to the relaxation described by the stretched exponential function $\exp(-(\lambda^{\rm LF}t)^{\beta})$. By applying a longitudinal magnetic field, it is possible to distinguish these two components. The solid curves in Figure 4.28 are the calculated results with the best-fit parameters.

Figure 4.29 shows $\lambda^{\rm LF}(H)$ measured at $T = 0.035$ K. The simple exponential correlation function $S(t) = \langle \boldsymbol{S}_i(0) \cdot \boldsymbol{S}_i(t) \rangle \sim \exp(-ft)$ is not enough to describe $\lambda^{\rm LF}(H)$ at the lowest temperature. The spin dynamic correlation function should take the following general form

$$S(t) \sim (\tau/t)^x \exp(-ft). \quad (4.16)$$

$\lambda^{\rm LF}(H)$ measured at $T = 0.035$ K can be fitted by the following equation

$$\lambda^{\rm LF}(H) = 2\Delta^2\tau^x \int_0^{\infty} \exp(-ft)\cos(2\pi\gamma_\mu H_{\rm LF}t)dt, \quad (4.17)$$

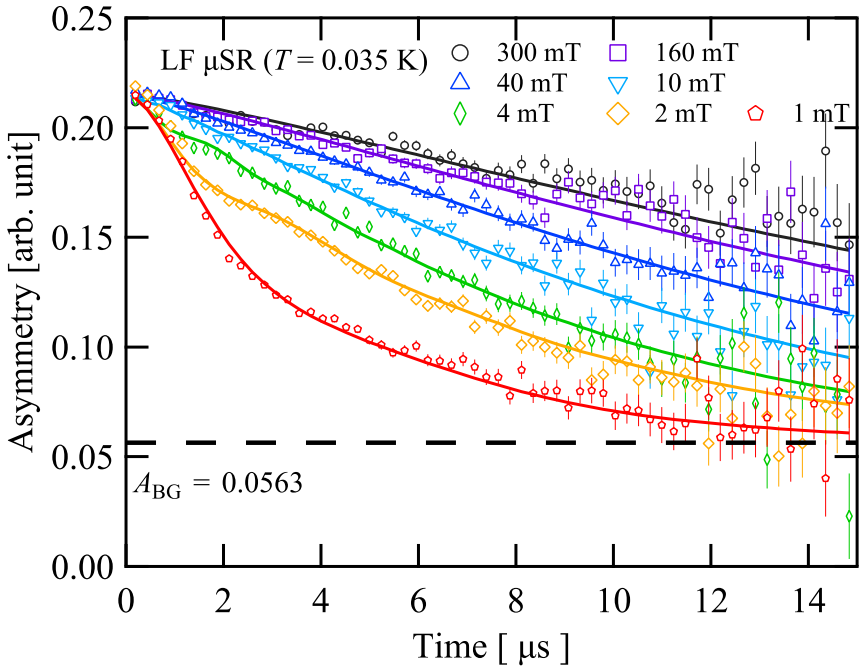

Figure 4.28: LF μSR spectra of $SrLaCuSb_{0.8}Nb_{0.2}O_6$ measured at 0.035 K. Solid curves are results of fitting by Eq. 4.15.

where τ and $1/f$ are the early and late time cutoffs, respextively, and x can be defined as a critical exponent [25, 134, 144, 145]. In Eq. 4.16, $x = 0$ means an exponential correlation function with a single correlation time, which leads to well-known Redfield formula

$$\lambda^{\mathrm{LF}}(H) = \frac{2\Delta^2 f}{f^2 + (\gamma_\mu H_{\mathrm{LF}})^2}. \tag{4.18}$$

The solid and dashed lines in Fig. 4.29 show the best fit for the case where x is fixed to 0 and x is a free parameter in the fitting using Eq. 4.17, respectively. $x = 0.779(6)$ and $f = 5.8(8)$ MHz give a good description of $\lambda^{\mathrm{LF}}(H)$. This result indicates that the spins fluctuating at 5.8(8) MHz in $SrLaCuSb_{0.8}Nb_{0.2}O_6$ are entangled not only in space but also in time. Such a result was also reported for $S = 1/2$ random J_1–J_2 SLHAF $Sr_2CuTe_{1-x}W_xO_6$ [124]. Such spatio-temporal entanglement may be a feature of a QDGS induced by bond randomness effect. In addition, such $\lambda^{\mathrm{LF}}(H)$ in LF-μSR was also found in $YbMgGaO_6$ [25], which is a promising candidate of QSLs, although bond randomness has been pointed out to exist there [26].

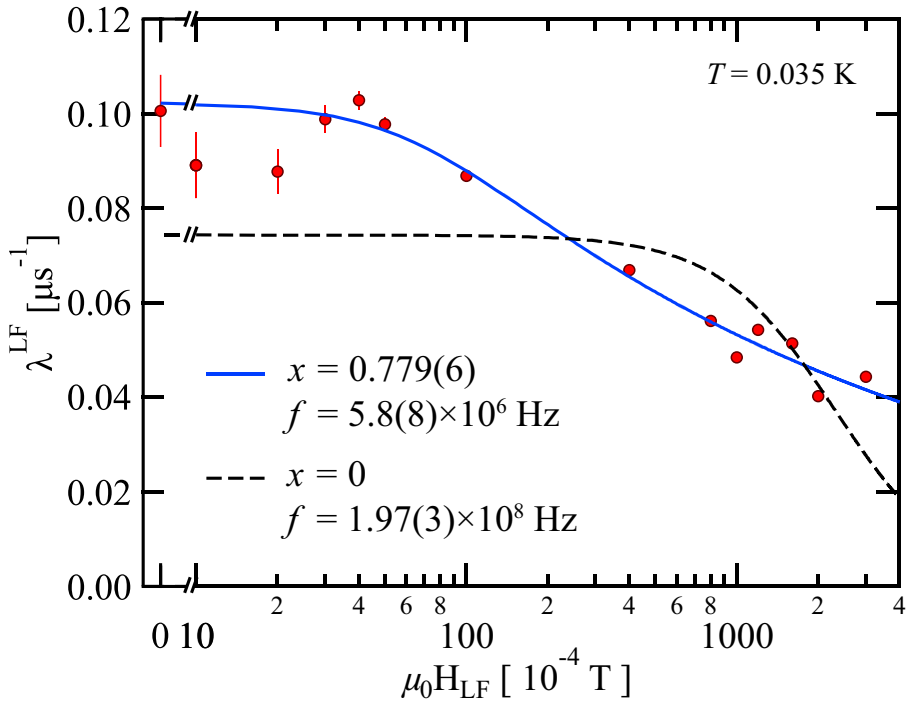

Figure 4.29: LF dependence of the muon spin relaxation rate, $\lambda^{\mathrm{LF}}(H)$, at 0.035 K. The solid line is the fits to $\lambda^{\mathrm{LF}}(H)$ using Eq. 4.17 with $x = 0.779(6)$ and $f = 5.8(8)$ MHz. The dashed line is the fit to $\lambda^{\mathrm{LF}}(H)$ using Eq. 4.17 with $x = 0$ fixed.

4.3 Summary

In the $SrLaCuSb_{1-x}Nb_xO_6$ systems, substitution of Nb for Sb naively produces new local exchange interactions $J_1^{(Sb,Nb)}$, $J_1^{(Nb,Nb)}$, $J_2^{(Nb,Nb)}$ via SbO_6 and NbO_6 octahedra, as shown in Fig. 4.30, due to the difference in the electronic states of Nb and Sb in the midst of the super-exchange path. Since Nb and Sb ions are disordered in $SrLaCuSb_{1-x}Nb_xO_6$, bond randomness is induced. From the specific heat measurements for $0.1 \leq x \leq 0.5$, it was found that the magnetic ordering observed for $x = 0$ and 1 was suppressed by bond randomness. At least for $x = 0.2$, μSR measurements show that neither long-range magnetic ordering nor spin freezing occurs. The magnetic susceptibility, specific heat, and μSR

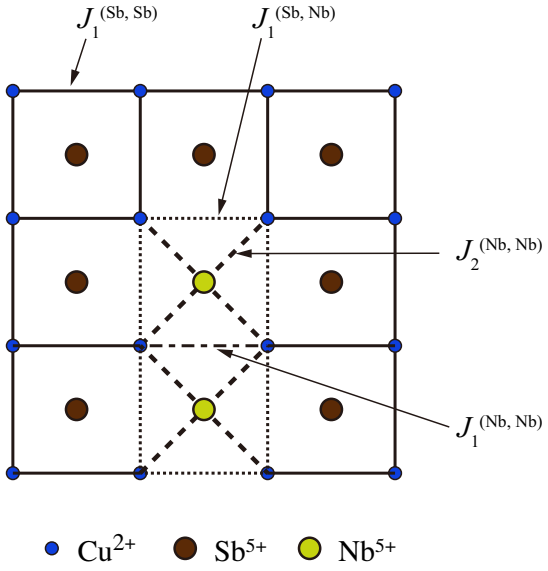

Figure 4.30: Exchange interactions $J_1^{Sb,Sb}$, $J_1^{Nb,Nb}$, $J_1^{Sb,Nb}$, and $J_2^{Nb,Nb}$ caused by the local configurations of Sb^{5+} and Nb^{5+} ions.

Table 4.3: Local exchange interactions $J_1^{(Sb,Sb)}$, $J_1^{(Nb,Nb)}$, $J_1^{(Sb,Nb)}$, and $J_2^{(Nb,Nb)}$ in $SrLaCuSb_{1-x}Nb_xO_6$ estimated from the J_1 and J_2 in the parent systems.

	$J_1^{(Sb,Sb)}/k_B$	$J_1^{(Sb,Nb)}/k_B$	$J_1^{(Nb,Nb)}/k_B$	$J_2^{(Nb,Nb)}/k_B$
$SrLaCuSb_{1-x}Nb_xO_6$	74.7 K	46.6 K	18.5 K	44.3 K

measurements indicate that a gapless QDGS is realized in $SrLaCuSb_{1-x}Nb_xO_6$. The QDGS induced by randomness is naively expected to be the random singlet state. The temperature dependence of the magnetic specific heat at low temperatures was reproduced by a summation of the Schottky specific

heat component due to weakly coupled spin pairs and the field-independent specific heat component described by the power law $C'(T) = AT^{\alpha}$. In fact, theoretical studies by exact diagonalization [46] and DMRG [61] predicted that the QDGS appearing in $S = 1/2$ random J_1–J_2 SLHAF is composed of three components: isolated singlet-dimers, resonating singlet-dimers clusters, and orphan spins, which is consistent with present experimental results.

Theoretical predictions of the temperature dependence of thermodynamic quantities are in conflict [48, 63, 64]. The exact diagonalization calculation of $S = 1/2$ J_1–J_2 SLHAF, which takes into account the magnetic frustration effect despite the small number of spins, has predicted $\chi(T) \propto T^{-1}$ and $C(T) \propto T$ in the low-temperature region [48]. On the other hand, QMC calculation of $S = 1/2$ J–Q model on square lattice, which can deal with a large number of spins but without magnetic frustration, has predicted $\chi(T) \propto T^{-\gamma}$ and $C(T) \propto T^{-\gamma+1}$ with $0 < \gamma < 1$ in the low-temperature range [63, 64]. The present magnetic susceptibility measurement of $SrLaCuSb_{1-x}Nb_xO_6$ gives a power law description as $\chi(T) = AT^{-1} + \chi_0$ with $0 < \gamma < 1$ for $0.1 < x < 0.5$ below 3 K. However, γ obtained from the magnetic specific heat analysis did not agree with γ obtained from the magnetic susceptibility analysis.

The characteristic properties observed in the specific heat, magnetization, and μSR measurements of $SrLaCuSb_{1-x}Nb_xO_6$ were also observed in $Sr_2CuTe_{1-x}W_xO_6$, which is magnetically described by a similar model. Therefore, the magnetic properties presented in $SrLaCuSb_{1-x}Nb_xO_6$ are deduced to be intrinsic to the low-energy state of the $S = 1/2$ random J_1–J_2 SLHAFs. Further experimental and theoretical approaches are required to elucidate the nature of the QDGS and related low-temperature magnetic properties observed in $SrLaCuSb_{1-x}Nb_xO_6$ and $Sr_2CuTe_{1-x}W_xO_6$.

Chapter 5

Summary and outlook

The quest for an experimental realization of a quantum disordered ground state (QDGS) is a frontier of condensed matter physics. In particular, quantum spin liquid (QSL) state, which does not exhibit any spontaneous symmetry breaking even at zero temperature, has attracted great attention. In low-dimensional spin-1/2 magnets with competing exchange interactions, strong quantum fluctuations suppress magnetic ordering and lead to QDGSs. Several promising candidates for QSLs have been found in low-dimensional antiferromagnets with spin-1/2. For example, herbertsmthite $ZnCu_3(OH)_6Cl_2$ is a well-studied spin-1/2 kagome Heisenberg antiferromagnet, which displays a number of QSL-like behavior [43, 45, 146]. μSR study shows that herbertsmithite does not order down to 50 mK in spite of a relatively large Weiss temperature $\Theta = -300\,\mathrm{K}$ [21]. However, the true origin of this QSL-like behavior is not clear, because there is a structural disorder such that Cu^{2+} ions substitute for 15% of Zn^{2+} ions on the inter-kagome-site yielding exchange randomness on the kagome layer.

Recently, some theoretical studies demonstrated that the randomness in the magnitude of exchange interaction suppresses the magnetic ordering and induces a QSL-like ground state. This QSL-mimicry is considered to be the random singlet (RS) state composed of randomly frozen singlets. In real materials, there exist almost unavoidable structural disorders such as defects, dislocations, and site disorder of ions, which give rise to bond randomness. The effect of bond randomness in frustrated quantum magnets has been attracting much attention from the viewpoint of realistic routes to QDGSs [46]. The thermodynamic properties of this RS state are theoretically predicted to be similar to those of QSL. In order to realize the true QSL state experimentally, it is essential to understand the RS state induced by bond randomness.

To understand QSL, it is necessary to know about QSL-mimicry in detail.

The spin-1/2 square lattice Heisenberg antiferromagnet (SLHAF) with the nearest-neighbor (NN) J_1 and next-nearest-neighbor (NNN) J_2 exchange interactions, referred to as the $S=1/2$ J_1–J_2 SLHAF, is a prototypical frustrated quantum magnet, whose ground state depends on the value of $\alpha = J_1/J_2$. In this system, the strength of the magnetic frustration can be tuned by changing the ratio of J_1 and J_2. QSL state is expected to emerge, if J_1 and J_2 compete, although the parameter region of J_1 and J_2 for QSL is narrow. In the presence of bond randomness in $S=1/2$ J_1–J_2 SLHAF, it was theoretically predicted that the RS state, which is the QSL-mimicry, appears in a relatively wide parameter range [48].

In this dissertation, I investigated the low-temperature magnetic properties of $S=1/2$ J_1–J_2 SLHAFs $SrLaCuSbO_6$ (SLCSO), $SrLaCuNbO_6$ (SLCNO), and their mixed compounds $SrLaCuSb_{1-x}Nb_xO_6$ (SLCSNO) to elucidate the effect of bond randomness on the frustrated quantum antiferromagnets. In SLCSO and SLCNO, weak bond randomness is expected to be induced by the disorder of Sr^{2+} and La^{3+} ions. Furthermore, much more significant bond randomness effects are expected in SLCSNO than their end-members because the non-magnetic ions Sb^{5+} and Nb^{5+} ions produce different structures of the NN and NNN exchange interactions.

I performed NPD, ESR, μSR, magnetization, and specific heat measurements on SLCSO and SLCNO powders. Magnetization and specific heat measurements show that the quasi-two-dimensional $S=1/2$ J_1–J_2 SLHAFs SLCSO and SLCNO undergo three-dimensional magnetic ordering at $T_N = 13.6$ and 15.7 K, respectively. The exchange parameters were estimated to be $J_1/k_B = 74.7$ K and $J_2/k_B = 1.62$ K for SLCSO, and $J_1/k_B = 18.5$ K and $J_2/k_B = 44.3$ K for SLCNO. From NPD measurements, the magnetic structures in 2D layers of SLCSO and SLCNO were determined to be of the Néel antiferromagnetic (NAF) type characterized by the propagation vector $\boldsymbol{k} = (1/2, 1/2, 0)$ on the body-centered structure and of the columnar antiferromagnetic (CAF) type described by the propagation vector $\boldsymbol{k} = (-1/2, 1/2, 1/2)$ on the face-centered structure, respectively. The magnitudes of the ordered moments of SLCSO and SLCNO were evaluated to be $m = 0.39(3)\,\mu_B$ and $0.37(1)\,\mu_B$ at 3.5 K, respectively, both of which are significantly smaller than those observed in the related systems Sr_2CuTeO_6 and Sr_2CuWO_6 without bond randomness. In the ZF-μSR measurement, extremely fast damping was observed. This result suggested a wide distribution of the internal fields, which should be due to the

bond randomness effect caused by the disorder of Sr^{2+} ions and La^{3+} ions. This is consistent with the reduction of ordered moment observed by NPD measurements. However, magnetic ordering is also observed in the μSR measurements. The bond randomness due to the disorder of Sr^{2+} ions and La^{3+} ions was not strong enough to destroy magnetic ordering.

I carried out magnetization and specific heat measurements on polycrystalline samples of $SrLaCuSb_{1-x}Nb_xO_6$ for $0.1 \leq x \leq 0.5$, and μSR measurement for $x = 0.2$. Compared with SLCSO and SLCNO, the bond randomness effect is more pronounced in $SrLaCuSb_{1-x}Nb_xO_6$ even for a small amount of Nb substitution. Neither long-range magnetic ordering nor spin freezing was observed in μSR measurements down to 0.035 K. LF-μSR measurements at 0.035 K shows that muon spin relaxation is still retained even at an applied longitudinal field of 0.3 T, suggesting that spin fluctuation are maintained even at 0.035 K. This is consistent with the emergence of the QDGS.

It was theoretically predicted that the low-temperature specific heat divided by temperature $C(T)/T$ and magnetic susceptibility $\chi(T)$ follow a same power law $\chi \propto T^{-\gamma}$ and $C(T)/T \propto T^{-\gamma}$ in the 2D RS state as well as the 1D RS state [63, 64]. Although temperature dependence of magnetic susceptibility and specific heat of $SrLaCuSb_{1-x}Nb_xO_6$ for $0.1 \leq x \leq 0.5$ follows a power law in the low-temperature region, the temperature exponents γ estimated from $C(T)/T$ and $\chi(T)$ do not agree with each other. In addition, the γ obtained from $C(T)/T$ was smaller than zero, although $0 < \gamma < 1$ was theoretically predicted for the RS state. Such a discrepancy is also observed in $S = 1/2$ random J_1-J_2 SLHAF $Sr_2CuTe_{1-x}W_xO_6$ with different parameters from those of $SrLaCuSb_{1-x}Nb_xO_6$. This behavior is considered to be an intrinsic properties of $S = 1/2$ random J_1-J_2 SLHAFs.

In the $SrLaCuSb_{1-x}Nb_xO_6$, the bond randomness suppresses the magnetic order, resulting in a QSL-like state, in which the spins are correlated both spatially and temporally. The QSL-like state induced by this randomness is naively considered to be the RS state. However, the observed properties of $SrLaCuSb_{1-x}Nb_xO_6$ were somewhat different from the theoretical prediction [48, 63, 64]. In order to characterize the QSL-like state realized in $SrLaCuSb_{1-x}Nb_xO_6$ in more detail, it is necessary to conduct experiments using a single crystal. For example, thermal transport measurements using single crystals can provide clues to distinguish the RS state from the QSL state. Unlike the QSL state, most of the singlets are localized in the RS state. The mean free path of the spinons responsible for heat transport will be much

different in the RS and QSL states.

It is also a future prospect to verify whether the bond randomness effect observed in $SrLaCuSb_{1-x}Nb_xO_6$ is similarly observed in other frustrated quantum antiferromagnets with other lattices such as triangular lattice. Theoretical studies using exact diagonalization have yielded similar thermodynamic properties regardless of the lattice model [46]. Further exploration of materials is needed to clarify the universal features caused by the bond randomness in frustrated quantum antiferromagnets.

Acknowledgments

First and foremost, I am extremely grateful to my supervisor, Prof. Hidekazu Tanaka for his invaluable advice, continuous support, and patience during my Ph.D. study. Prof. Tanaka led me into this exciting world of research. His immense knowledge and plentiful experience have encouraged me in my academic research and daily life. My deep gratitude also goes to Asst. Prof. Nobuyuki Kurita for providing technical help and valuable comments.

I would like to thank Prof. Wataru Higemoto of Tokyo Institute of Technology and Japan Atomic Energy Agency, Dr. Takashi U. Itoh of Japan Atomic Energy Agency, Mr. Jumpei Nakamura of High Energy Accelerator Research Organization, KEK, and Prof. Akihiro Koda of High Energy Accelerator Research Organization, KEK, for supporting μSR experiments at MLF, J-PARC. I would also like to thank Dr. Masato Hagihala of Japan Atomic Energy Agency for providing support for neutron diffraction experiments and magnetic structure analysis. I would like to express my gratitude to Prof. Takayuki Goto of Sophia university for his kind comments and support about NMR measurements. I am also thankful to Prof. Yu-ichiro Matsushita of Tokyo Institute of Technology for carefully guiding me on how to use the supercomputer TSUBAME and how to perform DFT calculations. I express my special thanks to Mr. Yuki Kojima and Mr. Mutsuki Saito for discussing various topics even before I joined Tanaka Lab. I owe my deepest gratitude to all the members of Tanaka group for their kindly supports and meaningful discussions.

The muon and neutron experiments at the Material and Life Science Experimental Facility of J-PARC were performed under the user programs (Proposal No. 2019A0272 and 2019B0257). The numerical calculations were carried out on the TSUBAME3.0 supercomputer at Tokyo Institute of Technology supported by the MEXT Project of the Tokyo Tech Academy for Convergence of Materials and Informatics (TAC-MI). This work was financially supported by Grants-in-Aid for JSPS Fellows (No. 20J12289) and Scientific Research (A) (No. 17H01142) and (C) (No. 19K03711).

Finally, I wish to thank my parents and sister for their love and encouragement, without whom I would never have enjoyed so many opportunities.

References

[1] C. Lacroix, P. Mendels, and F. Mila, *Introduction to frustrated magnetism: materials, experiments, theory* (Jan. 2011).

[2] L. Balents, Nature **464**, 199 (2010).

[3] N. D. Mermin and H. Wagner, Phys. Rev. Lett. **17**, 1133 (1966).

[4] N. D. Mermin and H. Wagner, Phys. Rev. Lett. **17**, 1307 (1966).

[5] T. Giamarchi, *Quantum physics in one dimension*, International Series of Monographs on Physics (Clarendon Press, 2003).

[6] Y. Endoh, G. Shirane, R. J. Birgeneau, P. M. Richards, and S. L. Holt, Phys. Rev. Lett. **32**, 170 (1974).

[7] S. E. Nagler, D. A. Tennant, R. A. Cowley, T. G. Perring, and S. K. Satija, Phys. Rev. B **44**, 12361 (1991).

[8] H. Bethe, Zeitschrift für Physik **71**, 205 (1931).

[9] I Affleck, J. Phys. Condens. Matter **1**, 3047 (1989).

[10] L. Savary and L. Balents, Rep. Prog. Phys. **80**, 016502 (2016).

[11] Y. Zhou, K. Kanoda, and T.-K. Ng, Rev. Mod. Phys. **89**, 025003 (2017).

[12] P. Anderson, Mater. Res. Bull. **8**, 153 (1973).

[13] V. Kalmeyer and R. B. Laughlin, Phys. Rev. Lett. **59**, 2095 (1987).

[14] Y. Ran, M. Hermele, P. A. Lee, and X. G. Wen, Phys. Rev. Lett. **98**, 117205 (2007).

[15] X. G. Wen, Phys. Rev. B **44**, 2664 (1991).

[16] A. Kitaev, Annals of Physics **321**, January Special Issue, 2 (2006).

[17] S. Depenbrock, I. P. McCulloch, and U. Schollwöck, Phys. Rev. Lett. **109**, 67201 (2012).

[18] D. E. Freedman, T. H. Han, A. Prodi, P. Müller, Q. Z. Huang, Y. S. Chen, S. M. Webb, Y. S. Lee, T. M. McQueen, and D. G. Nocera, J. Am. Chem. Soc. **132**, 16185 (2010).

[19] M. Fu, T. Imai, T. H. Han, and Y. S. Lee, Science **350**, 655 (2015).

[20] J. S. Helton, K. Matan, M. P. Shores, E. A. Nytko, B. M. Bartlett, Y. Yoshida, Y. Takano, A. Suslov, Y. Qiu, J. H. Chung, D. G. Nocera, and Y. S. Lee, Phys. Rev. Lett. **98**, 107204 (2007).

[21] P. Mendels, F. Bert, M. A. De Vries, A. Olariu, A. Harrison, F. Duc, J. C. Trombe, J. S. Lord, A. Amato, and C. Baines, Phys. Rev. Lett. **98**, 77204 (2007).

[22] M. P. Shores, E. A. Nytko, B. M. Bartlett, and D. G. Nocera, J. Am. Chem. Soc. **127**, 13462 (2005).

[23] S. Yan, D. A. Huse, and S. R. White, Science **332**, 1173 (2011).

[24] Y. Li, H. Liao, Z. Zhang, S. Li, F. Jin, L. Ling, L. Zhang, Y. Zou, L. Pi, Z. Yang, J. Wang, Z. Wu, and Q. Zhang, Sci. Rep. **5**, 16419 (2015).

[25] Y. Li, D. Adroja, P. K. Biswas, P. J. Baker, Q. Zhang, J. Liu, A. A. Tsirlin, P. Gegenwart, and Q. Zhang, Phys. Rev. Lett. **117**, 97201 (2016).

[26] Z. Zhu, P. A. Maksimov, S. R. White, and A. L. Chernyshev, Phys. Rev. Lett. **119**, 157201 (2017).

[27] P. Bourgeois-Hope, F. Laliberté, E. Lefrançois, G. Grissonnanche, S. R. De Cotret, R. Gordon, S. Kitou, H. Sawa, H. Cui, R. Kato, L. Taillefer, and N. Doiron-Leyraud, Phys. Rev. X **91**, 41051 (2019).

[28] T. Itou, A. Oyamada, S. Maegawa, M. Tamura, and R. Kato, Phys. Rev. B **77**, 104413 (2008).

[29] M. Abdel-Jawad, I. Terasaki, T. Sasaki, N. Yoneyama, N. Kobayashi, Y. Uesu, and C. Hotta, Phys. Rev. B **82**, 125119 (2010).

[30] J. M. Ni, B. L. Pan, B. Q. Song, Y. Y. Huang, J. Y. Zeng, Y. J. Yu, E. J. Cheng, L. S. Wang, D. Z. Dai, R. Kato, and S. Y. Li, Phys. Rev. Lett. **123**, 247204 (2019).

[31] Y. Shimizu, K. Miyagawa, K. Kanoda, M. Maesato, and G. Saito, Phys. Rev. Lett. **91**, 107001 (2003).

[32] T. Yamamoto, T. Fujimoto, T. Naito, Y. Nakazawa, M. Tamura, K. Yakushi, Y. Ikemoto, T. Moriwaki, and R. Kato, Sci. Rep. **7**, 12930 (2017).

[33] S. Yamashita, Y. Nakazawa, M. Oguni, Y. Oshima, H. Nojiri, Y. Shimizu, K. Miyagawa, and K. Kanoda, Nat. Phys. **4**, 459 (2008).

[34] M. Yamashita, N. Nakata, Y. Kasahara, T. Sasaki, N. Yoneyama, N. Kobayashi, S. Fujimoto, T. Shibauchi, and Y. Matsuda, Nat. Phys. **5**, 44 (2009).

[35] M. Yamashita, N. Nakata, Y. Senshu, M. Nagata, H. M. Yamamoto, R. Kato, T. Shibauchi, and Y. Matsuda, Science **328**, 1246 (2010).

[36] M. Yamashita, Y. Sato, T. Tominaga, Y. Kasahara, S. Kasahara, H. Cui, R. Kato, T. Shibauchi, and Y. Matsuda, Phys. Rev. B **101**, 140407 (2020).

[37] S. R. White and A. L. Chernyshev, Phys. Rev. Lett. **99**, 127004 (2007).

[38] K. Watanabe, H. Kawamura, H. Nakano, and T. Sakai, J. Phys. Soc. Japan **83**, 34714 (2014).

[39] Y. C. He, M. P. Zaletel, M. Oshikawa, and F. Pollmann, Phys. Rev. X **7**, 31020 (2017).

[40] Y. Iqbal, F. Becca, S. Sorella, and D. Poilblanc, Phys. Rev. B **87**, 60405 (2013).

[41] Y. Iqbal, D. Poilblanc, and F. Becca, Phys. Rev. B **89**, 20407 (2014).

[42] H. J. Liao, Z. Y. Xie, J. Chen, Z. Y. Liu, H. D. Xie, R. Z. Huang, B. Normand, and T. Xiang, Phys. Rev. Lett. **118**, 137202 (2017).

[43] M. R. Norman, Rev. Mod. Phys. **88**, 41002 (2016).

[44] W. Zhu, S. shu Gong, and D. N. Sheng, Proc. Natl. Acad. Sci. U. S. A. **116**, 5437 (2019).

[45] J. Wen, S. L. Yu, S. Li, W. Yu, and J. X. Li, npj Quantum Mater. **4**, 12 (2019).

[46] H. Kawamura and K. Uematsu, J. Phys. Condens. Matter **31** (2019).

[47] K. Uematsu and H. Kawamura, J. Phys. Soc. Japan **86**, 44704 (2017).

[48] K. Uematsu and H. Kawamura, Phys. Rev. B **98**, 134427 (2018).

[49] K. Uematsu and H. Kawamura, Phys. Rev. Lett. **123**, 87201 (2019).

[50] H. Kawamura, K. Watanabe, and T. Shimokawa, J. Phys. Soc. Japan **83**, 103704 (2014).

[51] T. Shimokawa, K. Watanabe, and H. Kawamura, Phys. Rev. B **92**, 134407 (2015).

[52] K. Uematsu, T. Hikihara, and H. Kawamura, J. Phys. Soc. Japan **90**, 124703 (2021).

[53] L. O. Manuel and H. A. Ceccatto, Phys. Rev. B **60**, 9489 (1999).

[54] R. V. Mishmash, J. R. Garrison, S. Bieri, and C. Xu, Phys. Rev. Lett. **111**, 157203 (2013).

[55] G. Misguich, C. Lhuillier, B. Bernu, and C. Waldtmann, Phys. Rev. B **60**, 1064 (1999).

[56] R. N. Bhatt and P. A. Lee, Phys. Rev. Lett. **48**, 344 (1982).

[57] C. Dasgupta and S. K. Ma, Phys. Rev. B **22**, 1305 (1980).

[58] D. S. Fisher, Phys. Rev. B **50**, 3799 (1994).

[59] M. Tarzia and G. Biroli, Epl **82**, 67008 (2008).

[60] R. R. Singh, Phys. Rev. Lett. **104**, 1 (2010).

[61] H.-D. Ren, T.-Y. Xiong, H.-Q. Wu, D. N. Sheng, and S.-S. Gong, *Characterizing random-singlet state in two-dimensional frustrated quantum magnets and implications for the double perovskite* $Sr_2CuTe_{1-x}W_xO_6$, 2021, arXiv:2004.02128 [cond-mat.str-el].

[62] R. B. Griffiths, Phys. Rev. Lett. **23**, 17 (1969).

[63] L. Liu, W. Guo, and A. W. Sandvik, Phys. Rev. B **102**, 54443 (2020).

[64] L. Liu, H. Shao, Y. C. Lin, W. Guo, and A. W. Sandvik, Phys. Rev. X **8**, 41040 (2018).

[65] Rigaku Corporation, *Manual of the Mini Flex II* (Rigaku Corporation).

[66] F. Izumi and K. Momma, in Applied crystallography xx, Vol. 130, Solid State Phenomena (Oct. 2007), pp. 15–20.

[67] J. Rodríguez-Carvajal, Physica B **192**, 55 (1993).

[68] F. Izumi and T. Ikeda, in Mater. sci. forum, Vol. 321-324 I, Materials Science Forum (2000), pp. 198–204.

[69] S. Lovesey, *Theory of neutron scattering from condensed matter*, International series of monographs on physics (Clarendon Press, 1984).

[70] S. Torii, M. Yonemura, T. Yulius Surya Panca Putra, J. Zhang, P. Miao, T. Muroya, R. Tomiyasu, T. Morishima, S. Sato, H. Sagehashi, Y. Noda, and T. Kamiyama, J. Phys. Soc. Jpn. **80**, SB020 (2011).

[71] S Torii, M Yonemura, Y Ishikawa, P Miao, R Tomiyasu, S Satoh, Y Noda, and T Kamiyama, J. Phys.: Conf. Ser. **502**, 012052 (2014).

[72] Quantum Design Inc, *Manual of the MPMS XL* (Quantum design, Inc).

[73] Quantum Design Inc, *Manual of the PPMS 6000* (Quantum design, Inc).

[74] H. Suzuki, A. Inaba, and C. Meingast, Cryogenics (Guildf). **50**, 693 (2010).

[75] A Yaouanc and P. D. de Réotier, *Muon Spin Rotation, Relaxation, and Resonance: Applications to Condensed Matter*, International Series of Monographs on Physics (OUP Oxford, 2011).

[76] W. Higemoto, R. Kadono, N. Kawamura, A. Koda, K. M. Kojima, S. Makimura, S. Matoba, Y. Miyake, K. Shimomura, and P. Strasser, Quantum Beam Science **1** (2017).

[77] L. Capriotti, F. Becca, A. Parola, and S. Sorella, Phys. Rev. Lett. **87**, 972011 (2001).

[78] L. Capriotti and S. Sorella, Phys. Rev. Lett. **84**, 3173 (2000).

[79] P. Chandra and B. Doucot, Phys. Rev. B **38**, 9335 (1988).

[80] E. Dagotto and A. Moreo, Phys. Rev. Lett. **63**, 2148 (1989).

[81] R. Darradi, O. Derzhko, R. Zinke, J. Schulenburg, S. E. Krüger, and J. Richter, Phys. Rev. B **78** (2008).

[82] T. Einarsson and H. J. Schulz, Phys. Rev. B **51**, 6151 (1995).

[83] F. Figueirido, A. Karlhede, S. Kivelson, S. Sondhi, M. Rocek, and D. S. Rokhsar, Phys. Rev. B **41**, 4619 (1990).

[84] S. S. Gong, W. Zhu, D. N. Sheng, O. I. Motrunich, and M. P. Fisher, Phys. Rev. Lett. **113**, 27201 (2014).

[85] J. ichi Igarashi, J. Phys. Soc. Japan **62**, 4449 (1993).

[86] H. C. Jiang, H. Yao, and L. Balents, Phys. Rev. B **86** (2012).

[87] M. Mambrini, A. Läuchli, D. Poilblanc, and F. Mila, English, Phys. Rev. B **74** (2006).

[88] F. Mezzacapo, English, Phys. Rev. B **86** (2012).

[89] N. Read and S. Sachdev, Phys. Rev. Lett. **66**, 1773 (1991).

[90] J. Richter, R. Darradi, J. Schulenburg, D. J. Farnell, and H. Rosner, Phys. Rev. B **81** (2010).

[91] N. Shannon, B. Schmidt, K. Penc, and P. Thalmeier, English, Eur. Phys. J. B **38**, 599 (2004).

[92] N. Shannon, T. Momoi, and P. Sindzingre, Phys. Rev. Lett. **96**, 27213 (2006).

[93] R. R. Singh, Z. Weihong, C. J. Hamer, and J. Oitmaa, Phys. Rev. B **60**, 7278 (1999).

[94] J. Sirker, Z. Weihong, O. P. Sushkov, and J. Oitmaa, Phys. Rev. B **73**, 184420 (2006).

[95] O. P. Sushkov, J Oitmaa, and Z Weihong, Phys. Rev. B **63**, 104420 (2001).

[96] G. M. Zhang, H. Hu, and L. Yu, Phys. Rev. Lett. **91**, 67201 (2003).

[97] M. Zhitomirsky and K. Ueda, Phys. Rev. B **54**, 9007 (1996).

[98] V. Murg, F. Verstraete, and J. I. Cirac, Phys. Rev. B **79**, 195119 (2009).

[99] J. F. Yu and Y. J. Kao, Phys. Rev. B **85**, 94407 (2012).

[100] L. Wang, D. Poilblanc, Z. C. Gu, X. G. Wen, and F. Verstraete, Phys. Rev. Lett. **111**, 37202 (2013).

[101] T. Li, F. Becca, W. Hu, and S. Sorella, Phys. Rev. B **86**, 75111 (2012).

[102] D. Iwanaga, Y. Inaguma, and M. Itoh, J. Solid State Chem. **147**, 291 (1999).

[103] T. Koga, N. Kurita, M. Avdeev, S. Danilkin, T. J. Sato, and H. Tanaka, Phys. Rev. B **93**, 054426 (2016).

[104] S. Vasala, H. Saadaoui, E. Morenzoni, O. Chmaissem, T. S. Chan, J. M. Chen, Y. Y. Hsu, H. Yamauchi, and M. Karppinen, Phys. Rev. B **89** (2014).

[105] S. Vasala, M. Avdeev, S. Danilkin, O. Chmaissem, and M. Karppinen, J. Phys. Condens. Matter **26**, 496001 (2014).

[106] P. Babkevich, V. M. Katukuri, B. Fåk, S. Rols, T. Fennell, D. Pajić, H. Tanaka, T. Pardini, R. R. Singh, A. Mitrushchenkov, O. V. Yazyev, and H. M. Rønnow, Phys. Rev. Lett. **117**, 237203 (2016).

[107] H. C. Walker, O. Mustonen, S. Vasala, D. J. Voneshen, M. D. Le, D. T. Adroja, and M. Karppinen, Phys. Rev. B **94**, 64411 (2016).

[108] T. Koga, N. Kurita, and H. Tanaka, J. Phys. Soc. Japan **83** (2014).

[109] M. Watanabe, N. Kurita, H. Tanaka, W. Ueno, K. Matsui, and T. Goto, Phys. Rev. B **98** (2018).

[110] J. D. Reger and A. P. Young, Phys. Rev. B **37**, 5978 (1988).

[111] K. Majumdar, Phys. Rev. B **82**, 144407 (2010).

[112] Y. Xu, S. Liu, N. Qu, Y. Cui, Q. Gao, R. Chen, J. Wang, F. Gao, and X. Hao, J. Phys. Condens. Matter **29** (2017).

[113] J. Rodríguez-Carvajal, Physica B **192**, 55 (1993).

[114] M. P. Attfield, P. D. Battle, S. K. Bollen, S. H. Kim, A. V. Powell, and M. Workman, J. Solid State Chem. **96**, 344 (1992).

[115] D. V. West and P. K. Davies, J. Appl. Crystallogr. **44**, 595 (2011).

[116] L. J. De Jongh and A. R. Miedema, Adv. Phys. **23**, 1 (1974).

[117] J. K. Kim and M. Troyer, Phys. Rev. Lett. **80**, 2705 (1998).

[118] H. Rosner, J. Oitmaa, R. R. Singh, W. E. Pickett, and W. H. Zheng, Phys. Rev. B **67**, 144161 (2003).

[119] O. Mustonen, S. Vasala, E. Sadrollahi, K. P. Schmidt, C. Baines, H. C. Walker, I. Terasaki, F. J. Litterst, E. Baggio-Saitovitch, and M. Karppinen, Nat. Commun. **9**, 1085 (2018).

[120] B. Bernu and G. Misguich, Phys. Rev. B **63**, 134409 (2001).

[121] A. Suter and B. Wojek, Physics Procedia **30**, 12th International Conference on Muon Spin Rotation, Relaxation and Resonance (μ SR2011), 69 (2012).

[122] K. Horigane, M. Fujii, H. Okabe, K. Kobayashi, R. Horie, H. Ishii, Y. F. Liao, Y. Kubozono, A. Koda, R. Kadono, and J. Akimitsu, Phys. Rev. B **97**, 64425 (2018).

[123] W. Hong, L. Liu, C. Liu, X. Ma, A. Koda, X. Li, J. Song, W. Yang, J. Yang, P. Cheng, H. Zhang, W. Bao, X. Ma, D. Chen, K. Sun, W. Guo, H. Luo, A. W. Sandvik, and S. Li, Phys. Rev. Lett. **126**, 37201 (2021).

[124] S. Yoon, W. Lee, S. Lee, J. Park, C. H. Lee, Y. S. Choi, S. H. Do, W. J. Choi, W. T. Chen, F. Chou, D. I. Gorbunov, Y. Oshima, A. Ali, Y. Singh, A. Berlie, I. Watanabe, and K. Y. Choi, Phys. Rev. Mater. **5**, 14411 (2021).

[125] C. A. Steer, S. J. Blundell, A. I. Coldea, I. M. Marshall, T. Lancaster, P. D. Battle, D. Gallon, A. J. Fargus, and M. J. Rosseinsky, Physica B **326**, 513 (2003).

[126] E. W. Montroll and J. T. Bendler, J. Stat. Phys. **34**, 129 (1984).

[127] A. S. Wills, Physica B **276-278**, 680 (2000).

[128] J. Kanamori, J. Phys. Chem. Solids **10**, 87 (1959).

[129] Y. Xu, S. Liu, N. Qu, Y. Cui, Q. Gao, R. Chen, J. Wang, F. Gao, and X. Hao, J. Phys. Condens. Matter **30** (2018).

[130] R. Kubo, Phys. Rev. **87**, 568 (1952).

[131] N. Laflorencie, S. Wessel, A. Läuchli, and H. Rieger, Phys. Rev. B **73**, 60403 (2006).

[132] H. Q. Wu, S. S. Gong, and D. N. Sheng, Phys. Rev. B **99**, 85141 (2019).

[133] I. Kimchi, J. P. Sheckelton, T. M. McQueen, and P. A. Lee, Nat. Commun. **9**, 4367 (2018).

[134] A. Keren, G. Bazalitsky, I. Campbell, and J. S. Lord, Phys. Rev. B **64**, 54403 (2001).

[135] E Kermarrec, P Mendels, F Bert, R. H. Colman, A. S. Wills, P Strobel, P Bonville, A Hillier, and A Amato, Phys. Rev. B **84**, 100401 (2011).

[136] L. Vegard, Zeitschrift für Phys. **5**, 17 (1921).

[137] O. Mustonen, S. Vasala, K. P. Schmidt, E. Sadrollahi, H. C. Walker, I. Terasaki, F. J. Litterst, E. Baggio-Saitovitch, and M. Karppinen, Phys. Rev. B **98** (2018).

[138] M. Fujihala, K. Morita, R. Mole, S. Mitsuda, T. Tohyama, S. ichiro Yano, D. Yu, S. Sota, T. Kuwai, A. Koda, H. Okabe, H. Lee, S. Itoh, T. Hawai, T. Masuda, H. Sagayama, A. Matsuo, K. Kindo, S. Ohira-Kawamura, and K. Nakajima, Nat. Commun. **11**, 3429 (2020).

[139] R. S. Hayano, Y. J. Uemura, J. Imazato, N. Nishida, T. Yamazaki, and R. Kubo, Phys. Rev. B **20**, 850 (1979).

[140] P. D. De Reotier and A. Yaouanc, J. Phys. Condens. Matter **4**, 4533 (1992).

[141] A. Keren, Phys. Rev. B **50**, 10039 (1994).

[142] G. M. Luke, J. H. Brewer, S. R. Kreitzman, D. R. Noakes, M. Celio, R. Kadono, and E. J. Ansaldo, Phys. Rev. B **43**, 3284 (1991).

[143] R. Kadono, J. Imazato, T. Matsuzaki, K. Nishiyama, K. Nagamine, T. Yamazaki, D. Richter, and J. M. Welter, Phys. Rev. B **39**, 23 (1989).

[144] R. Sarkar, P. Schlender, V. Grinenko, E. Haeussler, P. J. Baker, T. Doert, and H. H. Klauss, Phys. Rev. B **10**, 241116 (2019).

[145] A. Keren and G. Bazalitsky, Physica B **289-290**, 205 (2000).

[146] P. Mendels and F. Bert, J. Phys. Soc. Japan **79**, 11001 (2010).

Publication List

1) M. Watanabe, N. Kurita, H. Tanaka, W. Ueno, K. Matsui, and T. Goto: Valence-bond-glass state with a singlet gap in the spin-1/2 square lattice random J_1-J_2 Heisenberg antiferromagnet $Sr_2CuTe_{1-x}W_xO_6$; Phys. Rev. B **98** (2018) 054422 (1-6).

2) Y. Kojima, M. Watanabe, N. Kurita, H. Tanaka, A. Matsuo, K. Kindo, and M. Avdeev: Quantum magnetic properties of the spin-1/2 triangular lattice antiferromagnet $Ba_2La_2CoTe_2O_{12}$; Phys. Rev. B **98** (2018) 174406 (1-8).

3) M. Saito, M. Watanabe, N. Kurita, A. Matsuo, K. Kindo, M. Avdeev, H. O. Jeschke, and H. Tanaka: Successive phase transitions and magnetization plateau in the spin-1 triangular lattice antiferromagnet $Ba_2La_2NiTeO_2O_{12}$ with small easy-axis anisotropy; Phys. Rev. B **100** (2019) 064417 (1-12).

4) T. Yajima, T. Soma, K. Yoshimatsu, N. Kurita, M. Watanabe, and A. Ohtomo: Heavy-fermion metallic state and Mott transition induced by Li-ion intercalation in LiV_2O_4 epitaxial films; Phys. Rev. B **104** (2021) 245104 (1-7).

5) M. Watanabe, N. Kurita, H. Tanaka, W. Ueno, K. Matsui, T. Goto, and M. Hagihala: Contrasting Magnetic Structures in $SrLaCuSbO_6$ and $SrLaCuNbO_6$: Spin-1/2 Quasi-Square-Lattice J_1-J_2 Heisenberg Antiferromagnets; Phys. Rev. B **105** (2022) 054414 (1-12).

6) M. Saito, R. Takagishi, N. Kurita, M. Watanabe, R. Nomura, H. Tanaka, Y. Fukumoto, K. Ikeuchi, K. Nakajima, and R. Kajimoto: Structures of magnetic excitations in spin-1/2 kagome-lattice antiferromagnets $Cs_2Cu_3SnF_{12}$ and $Rb_2Cu_3SnF_{12}$; Phys. Rev. B **105** (2022) 064424 (1-15).